



Max-Planck-Institut  
für Kolloid- und Grenzflächenforschung



# Tracking Self-assembly of Hierarchically Structured Soft Matter

DISSERTATION

zur Erlangung des akademischen Grades

„doctor rerum naturalium“

(Dr. rer. nat.)

in der Wissenschaftsdisziplin Biochemie

eingereicht an der

Mathematisch-Naturwissenschaftlichen Fakultät

der Universität Potsdam

von

Franziska Jehle

Ort und Tag der Disputation: Golm, 06. Juni 2019

Hauptbetreuer: Prof. Robert Seckler

Betreuer\*innen: Prof. Matt Harrington, Dr. Luca Bertinetti

Gutachter\*innen: Prof. Robert Seckler, Dr. Kerstin Blank, Prof. Hans Börner

Dem Anwenden muss das Erkennen vorausgehen.

- Max Planck -







## ABSTRACT

Protein-based materials are ubiquitous in nature and exhibit exceptional hierarchical architectures and mechanical properties despite a limited set of building blocks. Their structure may, thus, inspire the development of novel high-performance materials. The mussel byssus, a protein-based fibrous holdfast, has become a role model for the development of polymers with self-healing properties and of new types of underwater adhesives. Marine mussels (*Mytilidae*) are aquatic sessile organisms that inhabit wave battered rocky seashores. The synthesis of the proteinaceous byssus by which they attach to rocks is their key to withstand enormous mechanical forces from crashing waves without being swept away. The byssus is comprised of numerous single threads, which enable underwater adhesion to almost any accessible surface. Byssal threads are renowned for their remarkable mechanical properties, such as high stiffness, high toughness and self-healing capacity. Recent investigations have revealed that these properties arise from the hierarchical structure of the protein building blocks within the threads, as well from functional protein-metal coordination interactions that act as sacrificial load-bearing cross-links. Byssal threads rapidly form via biomolecular self-assembly under environmentally friendly conditions and thus have motivated researchers since decades to unravel their structure-function relationship and assembly process. In the present work, I undertake a multiscale *in vitro* and *in situ* investigation of mussel byssal thread core and cuticle, respectively. I aim at overcoming the constraints of previously described attempts in producing mussel-inspired materials by more closely mimicking the self-assembly of core building blocks and by a fundamental investigation of the cuticle ultrastructure, composition and assembly process.

The self-healing core of byssal threads consists of collagenous protein building blocks called preCols that self-assemble into a hierarchically structured semi-crystalline array. Histidine-rich domains (HRDs) at the termini of preCols are believed to trigger the self-assembly of the thread core in a pH-dependent manner and to form strong and reversibly breakable metal coordination cross-links that control the tough and self-healing behavior of threads. The byssus cuticle resembles a particle-reinforced composite, which surrounds and protects the fibrous core. It consists of biphasic granules, which are embedded in a matrix and up to now, only one proteinaceous component was verified to be present in the cuticle, namely the mussel foot protein 1 (mfp-1). Although the cuticle is about five times harder than the underlying structure, it exhibits very high failure strains making it a paragon for bio-inspired engineering polymers. To understand the formation of the hierarchical structure of the native material, which is essential for the threads' impressive properties, one needs

better knowledge of the physicochemical triggers underlying the transition from liquid protein precursors to a multi-level hierarchically structured material. I am addressing this problem by studying the development of the material from the production and storage site of the precursors to the fully developed cuticle.

In addition to studying the natural material, I harnessed peptides based on the native sequence of HRDs to demonstrate a new route for the production of complex nanostructured materials with tunable mechanical properties. Taking advantage of the pH sensitivity of the HRDs, I developed a protocol to form free-standing films from these peptides both in the absence and presence of metal ions. Results of spectroscopic and X-ray diffraction investigations indicate that similar to the byssus, this approach leads to complex multiscale structures that can be cross-linked and fortified via histidine-metal complexes. Moreover, these results demonstrate that this approach enables one to specifically tune both the higher order structure and the mechanical properties of the films depending on the processing and inclusion of metal ions. This work is reported in the first part of this thesis.

In the second part, I use a combination of high-resolution electron microscopy techniques and energy dispersive X-ray spectroscopy (EDS) for the ultrastructural and elemental analyses of the byssus cuticle. I demonstrate that the matrix of byssus cuticle does not consist of fatty acids as previously hypothesized, but rather that cysteine-rich proteins might contribute to the complex cuticle architecture. 3D-reconstruction of the particle-reinforced composite presents a detailed depiction of its complex and highly controlled ultrastructure and paves the way for potential structural and functional models. Moreover, the elemental analysis reveals a partitioning of metal ions, which was never observed before and might impact the design of future mussel-inspired coatings.

The third part builds on the findings of the second study to provide fundamental insights into the production and storage site of cuticle precursors and their self-assembly into a hierarchically structured coating. I demonstrate that the elemental distribution within the storage site of cuticle precursors resembles the one of the byssus cuticle. This result allows for the first time to assign specific precursor phases to the respective components of the mature cuticle. Moreover, I show that metal ions are absent from the storage vesicles of cuticle precursors, which is highly consistent with previous observations. Artificial induction of vesicle secretion and thread formation revealed critical insights based on high-resolution investigations of the byssal thread cuticle formation.

Taken together, the combined studies of byssus core and cuticle demonstrate a path toward the production of complex nanostructured materials and reveal critical insights into the ultrastructure, composition and assembly process of a natural coating. The results presented within

## ABSTRACT



---

this thesis not only broaden our understanding of physicochemical parameters influencing natural assembly processes but are also expected to help improving current concepts for mussel-inspired materials.

## TABLE OF CONTENTS

ABSTRACT .....	iii
TABLE OF CONTENTS.....	vi
LIST OF FIGURES.....	viii
LIST OF ABBREVIATIONS.....	x
1. INTRODUCTION .....	1
2. MOTIVATION & AIMS .....	5
3. STATE OF THE ART .....	7
3.2 Structure-function relationship.....	8
3.2.1 The plaque – a multifaceted underwater adhesive .....	8
3.2.2 The core – a self-healing graded block copolymer .....	11
3.2.3 The cuticle – a protective reinforced composite .....	12
3.3 Established methods for byssus examination .....	18
3.4 Mussel-inspired materials .....	20
3.4.1 Materials from extracted byssus proteins .....	20
3.4.2 Materials from recombinant byssus proteins.....	21
3.4.3 Materials from byssus peptides.....	23
4. METAL-TUNABLE SELF-ASSEMBLY OF HIERARCHICAL STRUCTURE IN MUSSEL-INSPIRED PEPTIDE FILMS.....	26
4.1 Material & Methods .....	28
4.1.1 Film Formation.....	28
4.1.2 Fourier Transform Infrared Spectroscopy.....	28
4.1.3 Raman Spectroscopy.....	28
4.1.4 X-ray Absorption Near Edge Spectroscopy (XANES).....	29
4.1.5 X-ray Diffraction .....	29
4.1.6 AFM-based Indentation .....	29
4.2 Results .....	30
4.2.1 Sequence Selection and Film Formation.....	30
4.2.2 Fourier Transform Infrared (FTIR) and Raman Spectroscopy .....	30
4.2.3 X-ray absorption spectroscopy (XAS).....	32
4.2.4 Polarized Raman Spectroscopy.....	33
4.2.5 X-ray Diffraction.....	34
4.2.6 Mechanical Characterization .....	37
4.3 Discussion .....	39



4.4	Conclusion .....	41
5.	ULTRASTRUCTURE AND COMPOSITION OF BYSSAL THREAD CUTICLE.....	42
5.1	Material & Methods .....	44
5.1.1	Chemical fixation & embedding.....	44
5.1.2	TEM-EDS.....	44
5.1.3	FIB - SEM .....	44
5.1.4	Image processing .....	45
5.1.5	Segmentation.....	45
5.1.6	Volume fractions and 3D thickness mapping .....	45
5.2	Results .....	46
5.2.1	Ultrastructure of <i>M. edulis</i> byssal thread cuticle.....	46
5.2.2	Elemental composition of byssal thread cuticle .....	47
5.2.3	3D-reconstruction of cuticle granules.....	49
5.3	Discussion .....	55
5.4	Conclusion .....	59
6.	DYNAMIC FORMATION PROCESS OF BYSSAL THREAD CUTICLE.....	60
6.1	Material & Methods .....	61
6.1.1	Chemical fixation and embedding .....	61
6.1.2	Induced secretion and thread formation.....	62
6.1.3	Sample preparation for TEM.....	62
6.1.4	TEM-EDS.....	62
6.1.5	FIB-SEM .....	63
6.1.6	Image processing .....	63
6.1.7	Segmentation.....	63
6.2	Results .....	64
6.2.1	Development of a fixation protocol suitable for mussel foot tissue .....	64
6.2.2	Ultrastructure of cuticle vesicles in gland tissue .....	65
6.2.3	Elemental composition of cuticle vesicles .....	67
6.2.4	3D-reconstruction of vesicle phases .....	70
6.2.5	Induced thread formation.....	72
6.3	Discussion .....	75
6.4	Conclusion .....	77
7.	REFERENCES .....	79
8.	DECLARATION OF ORIGINALITY / EIDESSTÄTTLICHE ERKLÄRUNG .....	87
9.	ACKNOWLEDGEMENTS .....	88

**LIST OF FIGURES**

Figure 1. Mussel byssal threads and their functional parts. .... 2

Figure 2. Byssal thread fabrication and morphology. .... 7

Figure 3. Structural hierarchy of byssal threads. .... 10

Figure 4. Schematic organization of gland tissue within mussel foot..... 15

Figure 5. Schematic overview of thread formation. .... 17

Figure 6. HRD-peptide based studies. .... 24

Figure 7. Self-assembly of the mussel byssal thread and the bioinspired system..... 27

Figure 8. HRD-based peptides spontaneously assemble into amyloid  $\beta$ -sheet structures. .... 32

Figure 9. XANES spectra of HRD-based peptide film and Zn references. .... 33

Figure 10. Stacking of  $\beta$ -sheets in HRD-based peptide films. .... 34

Figure 11. XRD patterns of HRD-based peptide films. .... 35

Figure 12. Alignment of structures in HRD-based peptide films..... 35

Figure 13. Results of the radial and azimuthal integration of XRD pattern. .... 36

Figure 14. Metal-binding effects the mechanical properties of HRD-based peptide films. .... 38

Figure 15. Model of multiscale structure in HRD-based peptide films..... 40

Figure 16. The cuticle of *M. edulis* byssal threads contains biphasic granules..... 46

Figure 17. Sulfur and metal ions show distinct distributions in the thread cuticle. .... 48

Figure 18. FIB-SEM setup for imaging the cuticle of *M. edulis* threads in three dimensions. ... 50

Figure 19. Image processing by using custom-written python scripts. .... 51

Figure 20. Architecture of biphasic cuticle granules..... 51

Figure 21. Orientation of the electron-dense granule phase. .... 52

Figure 22. Alignment of the electron-dense granule phase. .... 52

Figure 23. Mean volume fraction  $\phi$  of cuticle granules..... 53

Figure 24. The electron-dense granule phase exhibits a very consistent thickness..... 54

Figure 25. Identification of cuticle vesicles within the gland tissue. .... 65

Figure 26. Cuticle gland cells contain vesicles with different phases. .... 66

Figure 27. Nitrogen and sulfur composition of cuticle gland vesicles. .... 68

Figure 28. Elemental composition of cuticle gland vesicles..... 69

Figure 29. FIB-SEM setup for imaging the gland tissue vesicles in three dimensions. .... 70

Figure 30. 3D-reconstruction of secretory cuticle vesicles reveals the different phases..... 71

Figure 31. Mean volume fraction  $\phi$  of cuticle gland vesicles. .... 72



---

Figure 32. Induced thread formation.....	72
Figure 33. Secretion of cuticle vesicles. ....	73
Figure 34. Induced thread shows the ultrastructure of cuticle assembly. ....	74

**LIST OF ABBREVIATIONS**

AFM	atomic force microscopy
Ala	Alanine
BSE	backscattered electrons
DMA	dynamic mechanical analysis
DOPA	3, 4-dihydroxyphenylalanine
ECM	extracellular matrix
EDS	energy dispersive X-ray spectroscopy
EDTA	ethylenediaminetetraacetic acid
EPR	electron paramagnetic resonance
ESEM	environmental scanning electron microscopy
EXAFS	extended X-ray absorption fine structure
FIB-SEM	focused ion beam – scanning electron microscopy
FTIR	Fourier-transform infrared
Gly	Glycine
GRAVY	grand average of hydropathy
HAADF	high-angle annular dark field
His	Histidine
HPF	high-pressure freezing
HRD	histidine-rich domain
HRD-DN	peptide based on the N-terminal HRD of preCol-D
LC	liquid-crystalline
Lys	Lysine
$\mu$ CT	micro-computed tomography
mfp	mussel foot protein
PEG	polyethylene glycol
preCol	prepepsinized collagenous protein
preCol-D	distal prepepsinized collagenous protein
preCol-NG	non-graded prepepsinized collagenous protein
preCol-P	proximal prepepsinized collagenous protein

## LIST OF ABBREVIATIONS

---



ptmp	proximal thread matrix protein
rfp	recombinant foot protein
SAXD	small-angle X-ray diffraction
SE	secondary electrons
SEM	scanning electron microscopy
SCP	soft colloidal probe
SIMS	secondary ion mass spectroscopy
STEM	scanning transmission electron microscopy
TEM	transmission electron microscopy
tmp	thread matrix protein
WAXD	wide-angle X-ray diffraction
XANES	X-ray absorption near edge structure
XAS	X-ray absorption spectroscopy
XRD	X-ray diffraction





## 1. INTRODUCTION

Through billions of years of natural selection, living organisms have evolved remarkable materials with excellent properties. Biological materials, such as wood, bone and insect carapaces are omnipresent in our everyday life and some of their building blocks (cellulose and chitin) rank among the most abundant polymers on earth.<sup>1</sup> Their appearance and mechanical properties are as versatile as their function; yet the formation of biological materials is based on a limited selection of building blocks.<sup>1,2</sup> The main components in nature's toolbox are polymers based on proteins or sugars (e.g. collagen, cellulose, chitin) that often form composites with minerals and ions, resulting in a hierarchical architecture at multiple length-scales.<sup>1,3</sup> The hierarchical structure of biological materials is thereby a consequence of controlled self-assembly, which takes place under ambient conditions with minimized energy use.<sup>4</sup> The predominant assembly motifs in biological materials are fibers.<sup>1</sup> Among these, collagen, keratin and silk are prominent examples of protein-based fibrous materials with remarkable mechanical properties. Collagen is the most abundant protein in mammals and can be found in our skin, tendon and bone, where it meets different mechanical requirements.<sup>5</sup> The example of collagen emphasizes the diversity of protein-based materials in mechanics and function despite a limited set of twenty amino acids, which are the building blocks of any proteinaceous material. However, the composition of amino acids, the organization into associated folding patterns and the interaction of single components lead to the observed huge diversity among protein-based biological materials.<sup>6</sup> The resulting hierarchical architecture defines material function and mechanical performance, such as elasticity, toughness, self-healing and rigidity.<sup>1,6,7</sup>

Silk might be the most prominent example of proteinaceous fibrous materials due to its outstanding mechanical properties and hierarchical architecture. It combines high tensile strength with extensibility and outperforms man-made fibers, such as Kevlar.<sup>8,9</sup> Yet, silk is produced at ambient temperature, low pressure and with water as a solvent - making it a paragon for sustainably produced high-performance polymers. Sustainability in polymer production has become a major issue, since we are facing huge endangerment of our ecosystem and health by plastic pollution.<sup>10,11</sup> Along these lines, spider silk has been extensively studied for decades in order to unravel its structure-function relationship and assembly process. It mainly consists of large repetitive proteins, called spidroins that are stored in a specific gland, where they are proposed to be pre-aligned in a nematic liquid crystalline phase.<sup>12</sup> A combination of physicochemical changes and mechanical influences (acidification, ion exchange, water removal and shear forces) trigger the silk fiber assembly during its spinning process.<sup>12</sup> Unraveling these critical parameters was an important

milestone toward the production of artificial spider silk.<sup>13</sup> The use of microfluidic devices, for example, allows to mimic the native ion and pH gradients as well as shear forces and was successfully applied to spin artificial silk based on recombinant proteins.<sup>14</sup>

Similar to spider silk, the mussel byssus is an extracorporeal fibrous structure that has inspired the production of various materials including self-healing polymers, underwater adhesives and tough coatings.<sup>15,16</sup> Mussels use byssal threads to anchor to accessible surfaces in wave battered habitats, where they dissipate enormous mechanical forces from crashing waves (Figure 1 A).<sup>17,18</sup> Byssal threads consist mainly of proteins and are formed one fiber at a time as a protein secretion in an organ called the mussel foot. They attain complex hierarchical structure via biomolecular self-assembly under environmentally friendly conditions. Their three functional parts, namely plaque, core and cuticle combine wet adhesion, high extensibility, high toughness, abrasion resistance and self-healing properties and each function is defined by the hierarchical arrangement of distinctly localized and specific proteins (Figure 1 B).<sup>19</sup>

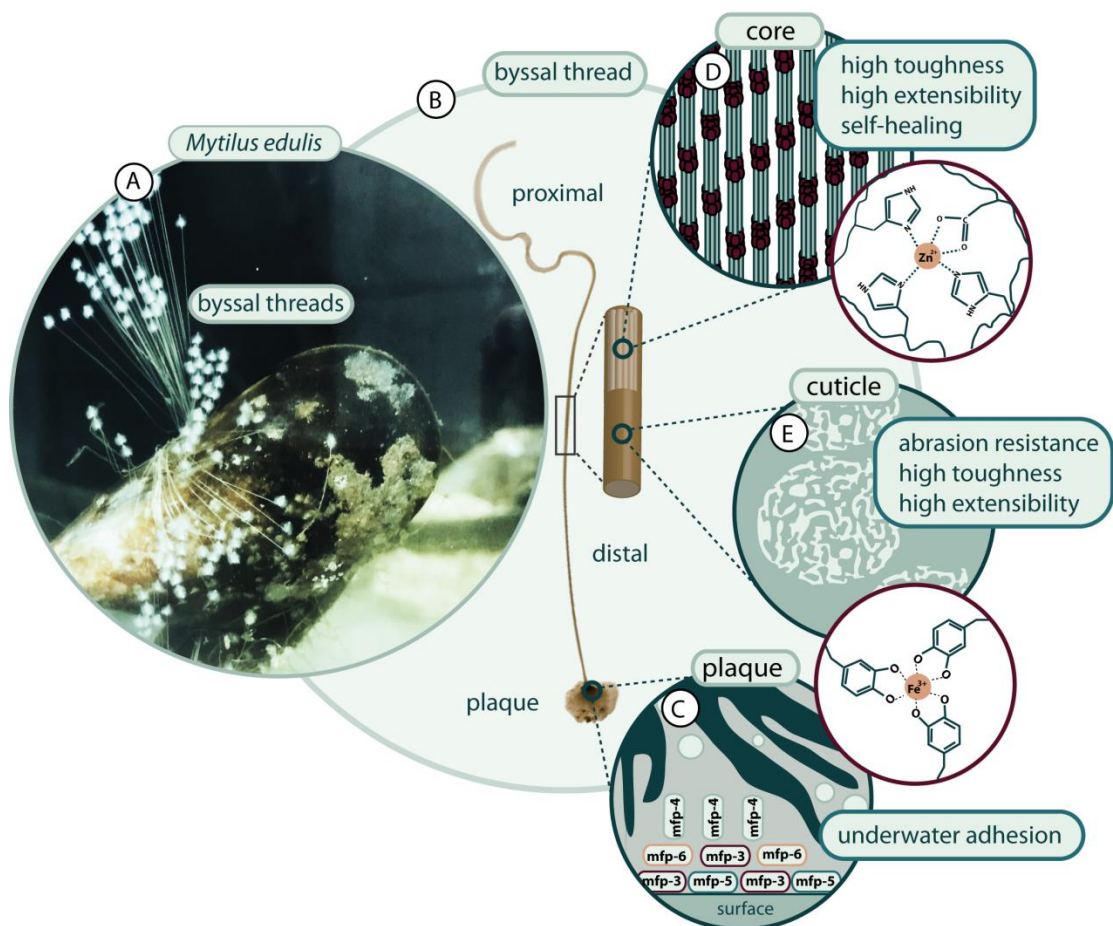


Figure 1. Mussel byssal threads and their functional parts.

A) Photo of a mussel (*Mytilus edulis*), that attached itself onto the aquarium glass by deposition of several byssal threads. B) Photo of a single byssal thread, which can be divided into an attachment site – the plaque and a fiber with a distal and proximal region. Threads consist of a fibrous core and a protective cuticle. The material properties are based on the hierarchical architecture of the different functional parts. C) The organization of DOPA-rich plaque proteins is highly spatially and temporally regulated. DOPA-Fe<sup>3+</sup> coordination



bonds between neighboring protein residues form and stabilize the hierarchical architecture. D) The core building blocks – termed preCols - are arranged in a semicrystalline framework. Histidine-rich domains at the termini of preCols are known to form sacrificial bonds via metal coordination and are thus proposed to play a crucial role in self-assembly, end-to end linkage of building blocks and self-healing behavior. E) The cuticle exhibits biphasic granules with an increased interaction of DOPA residues via  $\text{Fe}^{3+}$  complexation.

Protein-based biological materials, such as the mussel byssus, offer an excellent role model for the design and sustainable production of new high-performance polymers. In particular, the role of structural hierarchy and non-covalent cross-linking is highlighted in the example of the mussel byssus. Plaque proteins, for example, contain large amounts of 3, 4-dihydroxyphenylalanine (DOPA), a post-translational modification of tyrosine that has been shown to enable underwater adhesion via the versatile interaction with various surface chemistries.<sup>20</sup> Furthermore, the organization of more than six different proteins within the plaque architecture is highly spatially and temporally regulated, which greatly affects the interaction of single components (Figure 1 C).<sup>20</sup> DOPA-metal coordination bonds and cohesive interactions between neighboring protein residues form and stabilize the hierarchical architecture. A very specific amino acid composition can also be found in the core building blocks, termed preCols, which consist of different domains.<sup>21</sup> The central protein domain possesses a typical collagen motif sequence and mediates the organization of single proteins into triple helices, which further organize into bundles providing the fibrous core with an incredibly hierarchical architecture (Figure 1 D).<sup>22</sup> The domains at both termini of preCols contain elevated amounts of histidine residues (histidine-rich domains – HRDs), which are known to form sacrificial bonds via metal coordination and are thus proposed to play a crucial role in self-assembly, end-to end linkage of building blocks and self-healing behavior.<sup>21,23,24</sup> In addition, different variants of preCols are graded along the fibers axis, resulting in distinct mechanical properties of distal and proximal thread portion.<sup>21</sup> However, the details of composition, organization and interaction of single components is much less understood in the cuticle of byssal threads, which provides a protective coating. A DOPA-rich protein is believed to be the main cuticle component and the current model suggests an increased interaction of DOPA residues via  $\text{Fe}^{3+}$  complexation in defined subcompartments, leading to high hardness and concurrent extensibility (Figure 1 E).<sup>25</sup>

Although a great deal is known about the structure-function relationship in byssal threads, this complex biopolymeric material still issues a challenge to researchers, who draw inspiration from its remarkable architecture and mechanical functions. The main reason is an incomplete understanding of the physicochemical triggers underlying the transition from liquid protein precursors to a multi-level hierarchically structured material. Furthermore, some of the thread building blocks, especially in the cuticle, remain elusive to date. Therefore, most of the current mussel-inspired materials are based on isolated functions, such as DOPA catechol chemistry, and

neglect the native chemical context and hierarchical structure.<sup>19</sup> The successful production of artificial spider silk has taught us though that it is essential to understand the physical and chemical driving forces guiding the rapid self-assembly of such materials in detail in order to improve upon current generation of bio-inspired materials.

In the current thesis, I undertake a multiscale *in vitro* and *in situ* investigation of mussel byssus. I pursue two different approaches in order to gain more information about the chemical and physical mechanisms at play during formation of a complex hierarchically structured material from fluid precursors. In chapter 4, I produce a multi-level structured nanomaterial based on HRD peptide sequences by mimicking the native thread assembly conditions. By doing so, I obtain valuable insights into parameters influencing the preCol HRDs arrangement into a hierarchical architecture and the potential role of non-covalent cross-links. In chapter 5, I present a new understanding and potential model of cuticle ultrastructure and composition based on combined high-resolution electron microscopy, elemental mapping and 3D-reconstruction. Finally, in chapter 6, through *in situ* analysis of the production and storage site of cuticle precursors and their assembly via induced thread formation, I obtain valuable insights into the assembly process of the thread cuticle. The results presented within this thesis broaden our understanding of physicochemical parameters influencing natural assembly processes and will help to improve upon current mussel-inspired materials.



## 2. MOTIVATION & AIMS

During the past decades many research groups endeavored to mimic the outstanding structural and mechanical properties of mussel byssal threads.<sup>15,16,26</sup> Most of the strategies encompassed a minimalistic approach via synthetic chemistry by utilizing the identified key players of mechanical performance - DOPA and histidine residues.<sup>27-30</sup> Both amino acids are part of the distinctive metal coordination chemistry in byssal threads, thereby largely contributing to the biological materials performance.<sup>31</sup> Numerous hydrogels and polymers based on PEG-His and PEG-DOPA have impressively established this route for the production of self-healing materials, coatings and adhesives.<sup>27,28,32,33</sup> However, these materials lack the complex structure and hierarchy of the native material, which is known to contribute significantly to the threads impressive properties. Along these lines, biotechnological approaches represent a promising alternative by more closely resembling the natural protein sequence and conformation. Various studies on extracted and recombinant byssal proteins demonstrated the potential of biotechnological attempts.<sup>34-36</sup> Resulting materials range from hand-drawn fibers with native-like properties to nanofibrous scaffolds for bioactive molecules.<sup>37,38</sup> However, this approach holds limitations regarding the yield, purification and posttranslational modification of proteins – the latter being particularly crucial for the biomaterials performance.

Therefore, this thesis aims to overcome the constraints of previously described attempts in mimicking mussel byssus performance by pursuing two strategies: 1) the development of a mussel-inspired material by utilizing natural sequences, thereby keeping functional groups in their native context and 2) performing a fundamental investigation of the natural assembly process, which will enable a more in-depth mimicry and thus the improvement of mussel-inspired materials function. While numerous studies contributed to our current understanding of the single building blocks comprising the core, their hierarchical architecture and their role in byssus performance - there exists much less knowledge regarding the composition, ultrastructure and assembly of the cuticle. Thus, it is essential to take one step back and shed light on these missing pieces in order to complete our understanding of the thread cuticle and to develop mussel-inspired materials with superior properties.

The first study aims at producing a mussel-inspired material by pursuing both above presented strategies. Inspired by the multifunctional role of HRDs in byssus core self-assembly and function, peptides based on the natural sequence of HRDs were utilized. A pathway for the production of complex nanostructured materials was developed by mimicking the pH-triggered self-

assembly of the core's natural building blocks. The resulting mussel-inspired materials were analyzed using spectroscopic, X-ray diffraction and mechanical investigations, revealing an intimate connection between structure and function.

The second study aims for a better understanding of the ultrastructure and composition of the byssal thread cuticle. Despite its highly complex morphology, only one macromolecule was confirmed to be present to date. However, the thorough extraction of design principles for mussel-inspired coatings requires a profound understanding of the structure-function relationship in the byssus cuticle. High resolution transmission electron microscopy combined with energy dispersive X-ray spectroscopy (TEM-EDS) and focused ion beam – scanning electron microscopy (FIB-SEM) are used to elucidate its elemental composition and to 3D-reconstruct its microphase-separated features, respectively.

The third study aims at unraveling the dynamic formation process of the byssal thread cuticle, which is poorly understood thus far. The acquired knowledge will be an important step toward the deduction of design principles for pursuing the second strategy - more closely mimicking the native assembly process. The dynamic formation of the thread cuticle occurs very rapidly and hidden from our view. However, a combination of electron microscopy and elemental analysis was used to investigate three different states of thread formation: 1) the cuticle gland tissue and its vesicles 2) the induced secretion of precursors and their assembly and 3) the native thread cuticle.



### 3. STATE OF THE ART

#### 3.1 Morphology and function of byssal threads

Bivalves belonging to the genus *Mytilus* spp. are aquatic sessile organisms that spend most of their lives attached to surfaces in rather turbulent habitats. A proteinaceous holdfast – the byssus – made of high performance bio-polymeric fibers bestows them with the required tenacity to survive in wave-swept rocky shores. It consists of a bundle of single threads, which anchor mussels to a wide range of surface chemistries.<sup>39</sup> Single threads of *Mytilus edulis* are 2 to 4 cm in length and are produced one by one in the ventral groove of an organ called the mussel foot (Figure 2 A).<sup>40,41</sup>

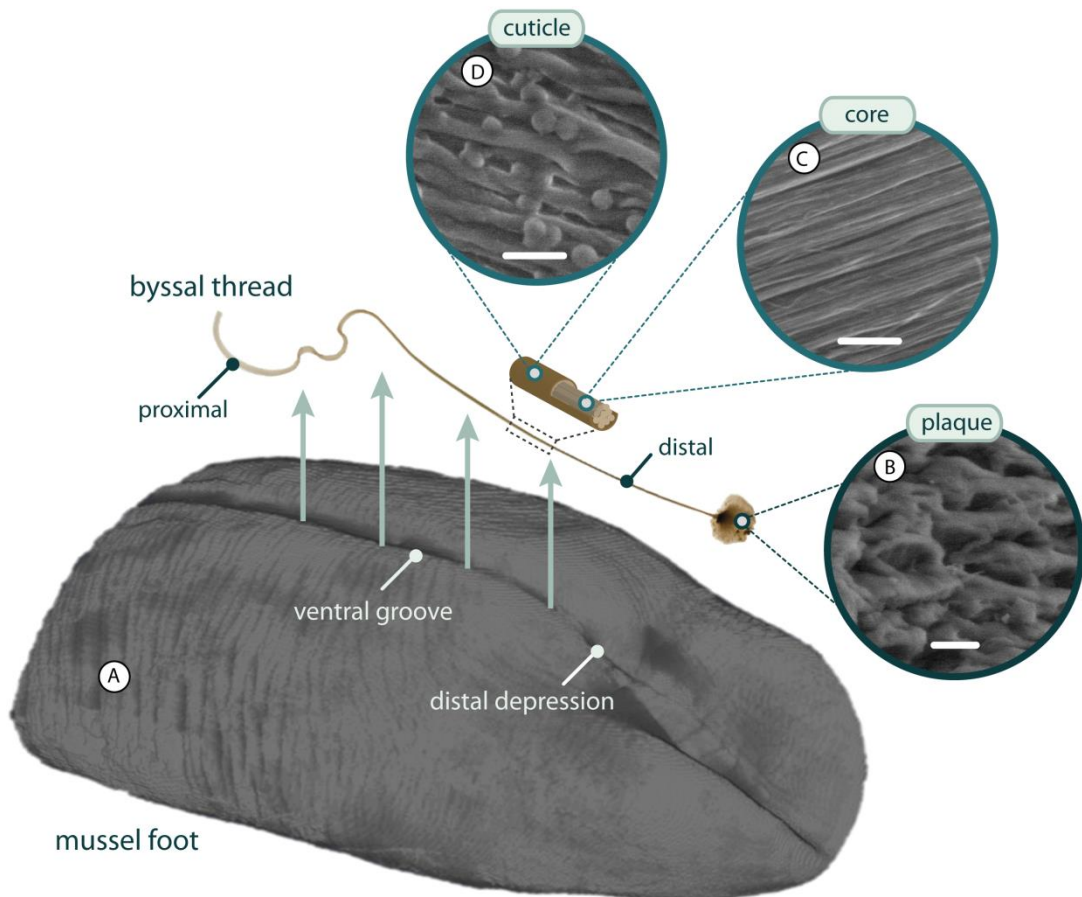


Figure 2. Byssal thread fabrication and morphology.

A) Byssal threads are produced one by one in the ventral groove of the mussel foot ( $\mu$ -CT image) and consist of an attachment disc - the plaque – and a polymeric fiber with morphologically and mechanically distinct parts – the distal and proximal region. Functional parts comprise the plaque (B), core (C) and cuticle (D) with distinct ultrastructural hallmarks (scale bar core and cuticle electron microscopy image: 2  $\mu$ m; scale bar plaque electron microscopy image: 1  $\mu$ m).

During this process, the foot is extended and emerges from the shell in order to affix its tip to a firm substrate (e.g. rocks, other mussels, wood pilings).<sup>41</sup> Once a suitable substrate is found, the production of a new byssal thread starts. Within just a few minutes, at least 10 and possibly up to 20 different proteins stored in vesicles get secreted from different mussel foot glands in a highly localized distribution to form the three structurally and functionally distinct parts - the plaque, core and cuticle (Figure 2 B-D).<sup>19,41</sup> Each part has its own purpose contributing equally to the remarkable mechanical properties and possessing complex hierarchically organized structural features. The most distal end of the thread – the plaque – is organized into an open-cell foam and specialized for adhesion (Figure 2 B).<sup>20</sup> The core, which can be divided into a distal and proximal part, combines high stiffness and extensibility and is known as a paragon for cell-free self-healing (Figure 2 C).<sup>21</sup> The cuticle is a very hard, but extensible non-mineralized coating exhibiting a fascinating ultrastructure that is believed to largely contribute to its remarkable mechanical properties (Figure 2 D).<sup>42</sup> During the past decades, there has been a great deal of interest in elucidating the structure-function relationship of each byssus part and the details are described within the following chapter.

## **3.2 Structure-function relationship**

### **3.2.1 The plaque – a multifaceted underwater adhesive**

Man-made adhesives still face difficulties in being moisture-resistant and applicable underwater. By contrast, countless marine sessile organisms including *M. edulis* rapidly form strong and tough underwater adhesives with apparent ease.<sup>20,43,44</sup> The formation of the protein-based mussel plaque, for instance, proceeds through an orchestrated secretion of different DOPA-rich water-soluble precursors; yet the released proteins are not at risk of being diluted by diffusion, but rather immediately form a porous solid, which can stick to almost any substrate ensuring their survival.<sup>20</sup> Numerous synthetic mussel-inspired adhesives attempted to reduce the complexity of plaque proteins by focusing only on the role of DOPA moieties in adhesion; however, the biochemistry of the native plaque proteins is much more complex than a single amino acid and furthermore, is highly organized and heterogeneous at different length scales and also timescales during formation.<sup>20,40,45</sup>

The plaque is located at the most distal end of the thread and is the first structure to be formed within an overall process that only takes a few minutes. At least six different proteins (mfp-2, -3S, -3F, -4, -5 and -6) are secreted between the distal depression and the substratum in a highly time-regulated manner. During the past decades, all isolated plaque proteins were characterized and



their functional role as well as their location and interaction were studied in detail.<sup>16,46,47</sup> Mfp-3 and mfp-5 were located at the adhesive interface and stand out due to their high amount of lysine and DOPA (up to 30 mol %), the latter is known to strongly interact with the surface chemistry and serves a wide range of purposes in mussel adhesion. For instance, DOPA in synthetic mfp-3 was shown to evict the surface hydration layers on titanium dioxide and hydroxyapatite surfaces, thus, enabling efficient underwater adhesion.<sup>48</sup> Similar behavior was observed for mfp-5 and both adhesion primers were shown to interact in a highly versatile manner with both hydrophilic and hydrophobic surfaces via their DOPA residues.<sup>49</sup> Physical interaction mechanisms likely include hydrogen bonding, hydrophobic interplay, metal coordination and covalent cross-linking (Figure 3 A).<sup>20,39</sup>

It might seem risky to rely the secure attachment primarily on a single amino acid residue, which is highly prone to oxidation in the O<sub>2</sub>-saturated seawater, but mussel adhesion presents an intriguing solution.<sup>20</sup> Mfp-6, a cysteine-rich protein that is also localized near the plaque-surface interface, was shown to act as an antioxidant. It is proposed that the oxidation of nine thiols within a single mfp-6 is coupled to the reduction of DOPA-quinone back to DOPA ensuring its chemical availability in adhesion.<sup>46</sup> Besides its role as reducing agent, mfp-6 is believed to act subsequently as a cross-linking partner for mfp-3, thereby enhancing the cohesion between plaque proteins. In general, cohesive interactions between plaque proteins are crucial for the mechanical stability of the foamy structure and are also based to a large extent on DOPA.<sup>20</sup> Among other aromatic moieties, DOPA is involved in cation- $\pi$  interactions with positively charged residues and was shown to form tris-DOPA-Fe<sup>3+</sup> coordination bonds within the highly abundant mfp-2.<sup>50,51</sup> The interaction between the plaque and the distal region of the core is likely mediated by mfp-4, which is the only plaque protein containing histidine side chains that are also highly abundant within the core proteins.<sup>52</sup> Coordination cross-links between histidine residues and metal ions might act as molecular bridge between the two parts of the thread.

Mussel adhesion is based on the highly complex interplay of different proteins, whose individual contributions to the overall structure and function are well understood. However, nine new mussel foot proteins (mfp-7 – mfp-15) assigned to the plaque were recently identified from transcriptomic analysis of the mussel foot plaque gland of *M. californianus*.<sup>53</sup> Although their specific function still needs to be unraveled, their discovery greatly emphasizes the complexity of this natural adhesive once more.

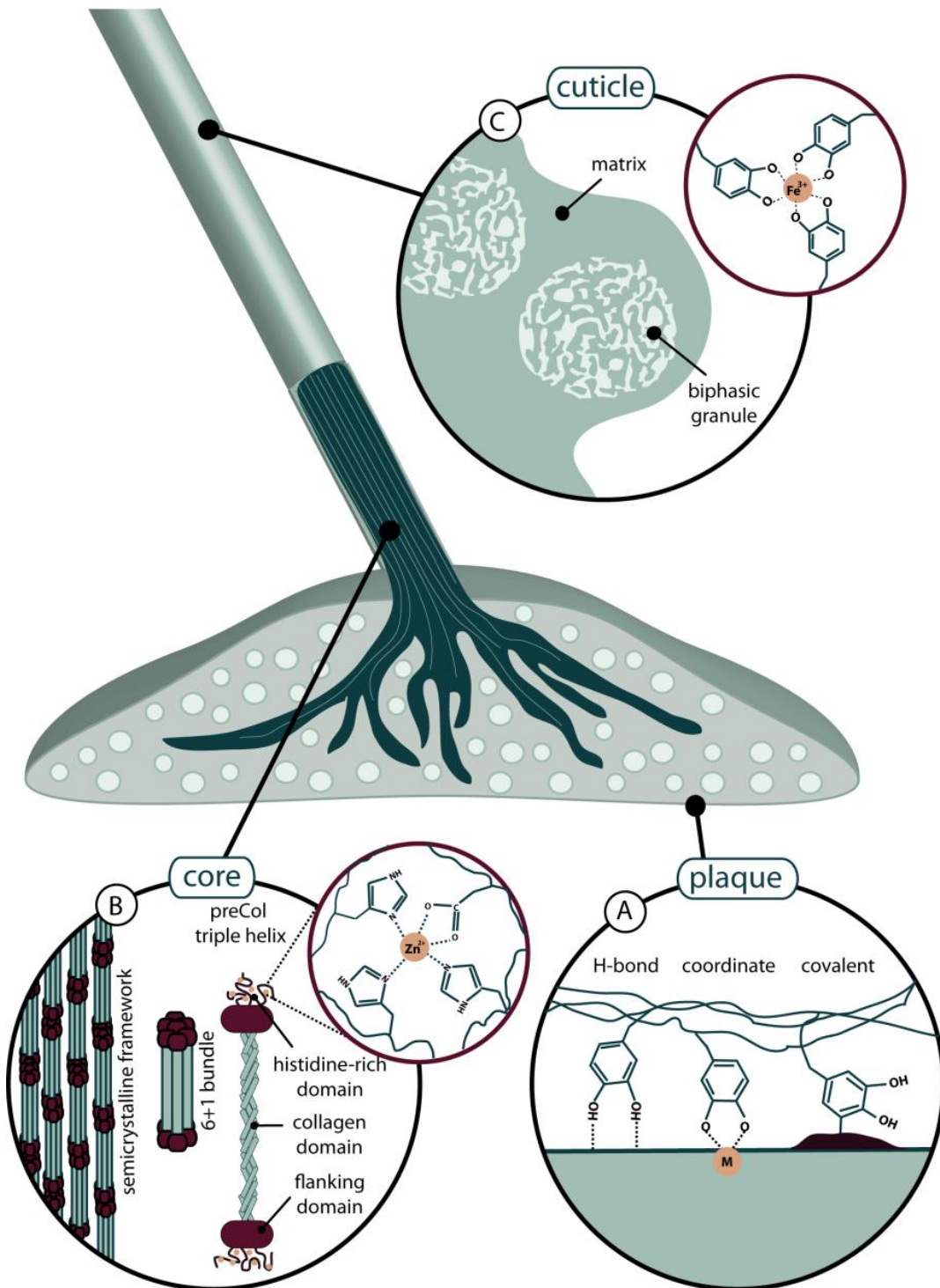


Figure 3. Structural hierarchy of byssal threads.

A) The plaque consists of different proteins and adhesion is mainly mediated by DOPA and Lys-rich mfp-3 and mfp-5. Physical interaction mechanisms of DOPA residues with the surface chemistry include hydrogen bonding, metal coordination and covalent cross-linking. B) The self-healing core of byssal threads is comprised of preCol proteins that consist of a central collagen domain as well as flanking domains and His-rich domains at the termini. PreCol triple helices form 6 + 1 bundles that are hierarchically organized into a semicrystalline framework. His-metal coordination bonds stabilize the highly organized structure and play an important role in self-healing. C) The cuticle consists mainly of the DOPA-rich mfp-1, which is cross-linked via DOPA- $\text{Fe}^{3+}$  bonds and exhibits biphasic structures embedded in a matrix.



### 3.2.2 The core – a self-healing graded block copolymer

The core of byssal threads, which is largely composed of a modified extracorporeal collagen, has fascinated researchers since decades.<sup>21</sup> Already more than sixty years ago, collagen was determined to be present in the distal portion of byssal threads by X-ray diffraction studies and at present is believed to largely contribute to the thread's remarkable properties.<sup>54,55</sup> It took another forty years – due to the chemical intractability of byssal threads – until pepsin-resistant collagen fragments were successfully isolated and partially sequenced.<sup>56</sup> This finding marked the starting point for an extensive amount of work in unraveling the core's complex composition and hierarchical architecture.

The core can be divided into a distal and proximal portion. The distal end is interlinked with the foamy structure of the plaque, while the proximal end is attached to the stem that anchors into the mussel's tissue. Both regions are morphologically and mechanically highly distinctive. Macroscopically, the distal part appears sleek and fibrous, whereas the proximal part can be distinguished by its wrinkled structure.<sup>57</sup> This localized appearance is also reflected on the nanoscale, where the thread's collagenous protein building blocks and matrix proteins are gradually organized.<sup>56</sup> Three different protein variants – termed preCols – appear to be graded along the thread axis.<sup>21</sup> Whereas preCol-D and preCol-P are exclusively found in the distal and proximal thread region, respectively, a third variant (preCol-NG (non-graded)) appears uniformly distributed and is thought to connect the two localized forms.<sup>58</sup> The different variants' common feature is a central domain characterized by a (Gly-X-Y)<sub>n</sub> repeat sequence typical of fibrillary collagen (Figure 3B). However, the morphological and mechanical gradient of byssal threads is believed to correlate with the variants' different flanking domains. These domains surround the central collagen domain and their primary sequence resembles spider drag-line silk in preCol-D, elastin in preCol-P and glycine-rich extensible domains from flagelliform silk in preCol-NG.<sup>21</sup>

At both termini, all variants possess HRDs containing ~ 20 mol % histidine, which are highly conserved between different mussel species, but are variable in the spacer regions between histidine residues in different preCol variants.<sup>21</sup> The nitrogen atoms (N<sub>τ</sub> and N<sub>π</sub>) of histidine are able to coordinate divalent metal ions at neutral to basic pH and thus serve as end-to-end linkage of preCol proteins in addition to covalent bonds (Figure 3 B).<sup>23,59</sup> Single preCol building blocks form triple helices and are further organized into 6 + 1 hexagonal bundles, which are axially staggered forming a semicrystalline framework (Figure 3 B).<sup>22,24</sup> Resulting preCol fibers are embedded in a protein matrix, which consists of two axially graded proteins – the thread matrix protein (tmp-1) and the proximally located ptmp-1.<sup>60-62</sup> Whereas ptmp-1 makes up approximately 35 % of the proximal thread dry weight, tmp-1 is much less abundant (ca. 0.5 - 2 % dry weight).<sup>60</sup> Although their detailed role is not

yet elucidated, ptmp-1 was demonstrated to affect collagen assembly *in vitro*, suggesting that matrix proteins play a vital role in the assembly of the core's structure and thereby its function.<sup>60</sup>

The graded distribution of molecules at the nanoscale, their interaction and hierarchical architecture is substantially displayed in the core's mechanical function and the distinct properties of distal and proximal region. The thread distal region is very stiff (up to 800 MPa) and strong but also extensible (~ 100 % strain), whereas the proximal region is characterized by a lower stiffness (~ 20 MPa) and an large extensibility of up to 200 % of its initial length.<sup>21</sup> By combining spectroscopic and X-ray diffraction techniques with *in situ* mechanical testing, a deep understanding of the underlying structure-function relationship was attained.<sup>22,24,63-65</sup> The high extensibility of threads was shown to stem from the unfolding of  $\beta$ -sheet structures in the flanking domains of preCol-D, since the collagenous domains were shown to merely strain by 2 %.<sup>22,63</sup> The combination of stiff collagen domains with less stiff sacrificial domains provides the threads with an intrinsic healing capacity during cyclic tensile loading caused by crashing waves.<sup>63</sup> The self-healing behavior of threads is based on the cooperative interplay of sacrificial HRDs and flanking domains providing hidden length.<sup>24</sup> When byssal threads are stretched beyond their yield point, sacrificial His-Zn coordination bonds rupture and thus enable flanking domains to unfold.<sup>23,24</sup> As soon as the threads are relaxed, both domains refold in a two-step time-displaced process with the flanking domains refolding immediately and a slower recovering of sacrificial metal coordination cross-links. Critical to this synergetic behavior of preCol domains is the core's building blocks hierarchical architecture.<sup>22,24</sup>

### 3.2.3 The cuticle – a protective reinforced composite

The cuticle of *M. edulis* is the part of byssal threads posing the most unresolved questions. Numerous studies have been aimed at unravelling the composition and structural features of this thin layer (~ 1 - 5  $\mu\text{m}$ ), which surrounds and protects the fibrous core.<sup>66</sup> The outstanding mechanical properties of this natural, non-mineralized coating are the main reason why it attracted extensive attention. Usually, high hardness of materials comes at the expense of extensibility - but the byssal cuticle remarkably combines both features.<sup>42</sup> Although it is about five times harder than the fibrous core, it exhibits very high failure strains making it a paragon for bio-inspired engineering polymers.<sup>42</sup>

Up to now, only one proteinaceous component was verified to be present in the cuticle, namely the mussel foot protein 1 (mfp-1). Unlike the collagenous proteins that it covers, mfp-1 is largely unstructured consisting of ~ 80 consensus decapeptide repeats (AKPSYPPTYK)<sub>n</sub>.<sup>67</sup> Due to its high content of lysine (20 mol %), mfp-1 is highly positively charged and exhibits a basic isoelectric point (pI) of ~ 10.3.<sup>68</sup> The highly conserved tyrosine residues are mostly enzymatically modified to 3,4-dihydroxyphenylalanine (DOPA). Similar to the graded building blocks in the core, an axial



gradient in the posttranslational modification of tyrosine to DOPA was detected in threads with higher DOPA concentrations being present in the distal part. This spatial organization is based on an analogous gradient from tip to base in the thread forming system, the mussel foot tissue.<sup>69</sup>

Despite the presence of only one verified component (although others have been proposed), the cuticle exhibits a very complex and distinctive ultrastructure. Within a homogeneous amorphous matrix, microphase-separated granules are embedded and make up to 50 % of the cuticle content (Figure 3 C).<sup>42</sup> The biphasic structures are ~ 500 - 1000 nm in diameter and show a domain size of approximately 20 - 40 nm.<sup>25,68</sup> It was proposed that granules provide the cuticle with damage tolerance, since cracks were observed to form first within the matrix of stretched *M. galloprovincialis* threads.<sup>42</sup> Along these lines, mussel species residing in subtidal, stiller waters - such as *Modiolus capax* and *Perna canaliculus* - show a homogeneous cuticle that lacks biphasic granules, which once more emphasizes their potential role in mechanics.<sup>42,70</sup>

The fascinating cuticle ultrastructure raises the question whether other macromolecules might contribute to its distinct features. In fact, fatty acids have been reported to be present in byssal threads and in the mussel foot and been speculated to act as anionic counterparts to the highly positively charged mfp-1.<sup>68,71</sup> The theory of other macromolecules being present in the cuticle was supported by secondary ion mass spectroscopy (SIMS), which revealed a higher nitrogen concentration in the thread core than in the cuticle.<sup>72</sup> However, transcriptomic analyses recently identified four relatively small proteins (mfp-16 – 19, 5 - 20 kDa), in the cuticle gland of *M. californianus* foot tissue. All of them contain high amounts of cysteine as well as other key amino acids - namely arginine, lysine, tyrosine, glycine, histidine, aspartate and glutamate.<sup>53</sup> It was hypothesized that the newly discovered proteins might be located in the cuticle matrix with their cysteine residues serving as redox regulators for the highly abundant DOPA in mfp-1 – similar to the role of mfp-6 in the plaque.<sup>53</sup> Cytochemical analyses performed on cuticle gland vesicles within the foot tissue revealed different lability of its components to protease treatment, which supports the presence of several distinct proteins in thread granules and matrix.<sup>73</sup> However, a reliable verification or identification of other components in the thread cuticle remains elusive to date.

Apart from potential macromolecules, the presence of inorganic ions, such as Fe, Si, Ca, V and Al, is beyond debate.<sup>72,74</sup> DOPA residues in mfp-1 and metal ions were shown to be co-localized within the cuticle and the presence of coordination cross-links (DOPA-Fe and DOPA-V) was demonstrated via confocal Raman spectroscopic imaging.<sup>25,42,72,74</sup> Furthermore, *in situ* resonance Raman spectroscopy revealed a higher DOPA-metal cross-link density in the granules than in the surrounding matrix, strongly implying that granules play a vital role in cuticle mechanics.<sup>25</sup> More recent studies, however, suggest they might serve a different function. Whereas granules were

previously assumed to be stiffer than the matrix, *in situ* atomic force microscopy (AFM) investigations revealed contrary results.<sup>70</sup> The biphasic structures appeared to be three-fold softer than the surrounding matrix in semi-hydrated conditions suggesting a model, in which granules are responsible for keeping the cuticle plasticized via hydration, preventing it from becoming brittle via drying during tidal cycles in high intertidal zones.<sup>70</sup> In order to be able to fully elucidate the mechanical role of the cuticle's distinct features, it will be inevitable to get deeper insight into its composition, ultrastructure and assembly process.

### 3.2.4 Thread formation

Byssal threads are characterized by their impressive mechanical properties, which are based on highly localized and hierarchically structured protein building blocks assembled with an exceptional precision. Although the scene of event – the mussel foot groove – is effectively concealed, there still exists a basic understanding of how byssal threads are fabricated. The byssal factory – the foot – contains three major glands that are organized in clusters around the ventral groove with no absolute boundaries between them.<sup>75</sup> Each gland is specialized for the synthesis, maturation, storage and secretion of the respective protein building blocks that are determined to form the plaque, core and cuticle. Since their discovery, the foot glands acquired various names, but on the basis of present knowledge regarding their content, they are currently denoted as plaque, core and cuticle gland (Figure 4).<sup>40</sup> The mechanism of thread formation is often compared to injection molding, a process used in polymer production providing the products with the desired morphology.<sup>40,41</sup>

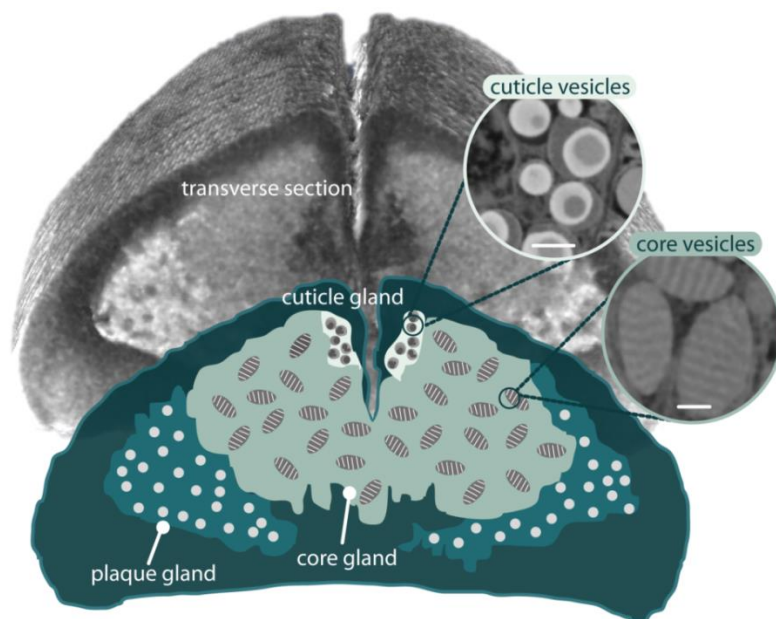


Figure 4. Schematic organization of gland tissue within mussel foot.

Transverse section of a mussel foot  $\mu$ -CT scan and corresponding color-coded illustration showing the approximate localization of the three glands. The plaque gland is located around the distal depression and contains plaque proteins stored in round vesicles. The core gland is the largest gland and produces and stores core vesicles, which are characterized by their typical banding pattern stemming from the organization of preCol proteins in a liquid-crystalline phase. The cuticle gland is located near the foot surface. Cuticle vesicles present electron-dense structures in the core and one or more outer layers. Scale bars: 1000 nm.

The distribution of the glands along the length of the foot corresponds to the relative position of the different thread parts that are to be synthesized. Therefore, the plaque gland is exclusively found around the distal depression and contains round vesicles ( $d = 1 - 2 \mu\text{m}$ ) of homogeneous appearance in which the plaque proteins are stored (Figure 5 A).<sup>75</sup> *In situ* hybridization localized mfp-2 and mfp-3 in the plaque gland and suggested that the six different plaque precursors are produced and stored in spatially separated parts.<sup>76,77</sup> When the formation of a new thread starts, vesicles containing the plaque proteins are secreted via ciliated longitudinal ducts in a precisely timed progression. Time-lapse mass spectrometry during secretion from a related species revealed that mfp-3 variants, mfp-5 and mfp-6 are secreted first after an acidification of the environment to  $\sim \text{pH } 2$ .<sup>20,45,46</sup> Rapid formation of the open-cell foam requires an inversion of a proteinaceous liquid phase into a solid porous structure (Figure 5 B). This spontaneous phase inversion is also observed in other marine adhesives, such as the cement of the sandcastle worm *Phragmatopoma californica*.<sup>43</sup> The adhesive glue of the sandcastle worm is secreted as a dense coacervate – a liquid-liquid phase separation of oppositely charged polyelectrolytes.<sup>43</sup> Complex coacervates are excellently suited for underwater adhesion, since they combine high density, low interfacial energies and high internal diffusion coefficients.<sup>78</sup> Although the polycationic mussel plaque proteins lack any polyanionic counterparts, purified mfp-3S was shown to form a single component coacervate triggered by

physicochemical parameters such as pH and ionic strength.<sup>79</sup> Therefore, it is currently assumed that coacervation of plaque proteins plays a crucial role in underwater adhesion.<sup>20,80</sup> However, its involvement in the formation process still needs to be demonstrated *in vivo*.

The large core gland spreads out over almost the entire length of the foot and stores the core's building blocks under acidic conditions in ellipsoidal secretory vesicles of 1 – 2  $\mu\text{m}$  in length (Figure 4). The current model suggests that preCol proteins are arranged in a smectic liquid-crystalline (LC) phase within the core's secretory vesicles, since they exhibit a characteristic banding pattern in TEM (Figure 4).<sup>37,81,82</sup> During secretion, collagen vesicles migrate in rows through the cytoplasm and terminate in the ventral groove, which is lined with ciliated epithelial cells (Figure 5 A).<sup>75</sup> It was hypothesized that the contact with basic seawater pH might trigger the coalescence of vesicles and the transition from LC phase to a stiff fiber with highly defined structural organization (Figure 5 C).<sup>40</sup> However, artificially induced threads only show alignment of preCols at small scales, suggesting that active processes such as muscle contractions of the foot are crucial for the higher order structure of byssal threads.<sup>40,41</sup> Locking of the highly ordered arrangement is proposed to be mediated via the N- and C-terminal HRDs of the preCols, which are highly sensitive to pH changes due to their elevated histidine content.<sup>83</sup> The transition to basic pH causes deprotonation of the histidine nitrogen atoms endowing them with the capacity to coordinate transition metal ions (e.g.,  $\text{Zn}^{2+}$ ,  $\text{Cu}^{2+}$ ,  $\text{Ni}^{2+}$ ) in highly defined complexes (Figure 5 C).<sup>23</sup> Additional stability of the structure might be mediated via posttranslational conversion of highly conserved tyrosine residues to DOPA, whose oxidized form at basic pH is able to cross-link individual preCol molecules.<sup>17</sup>

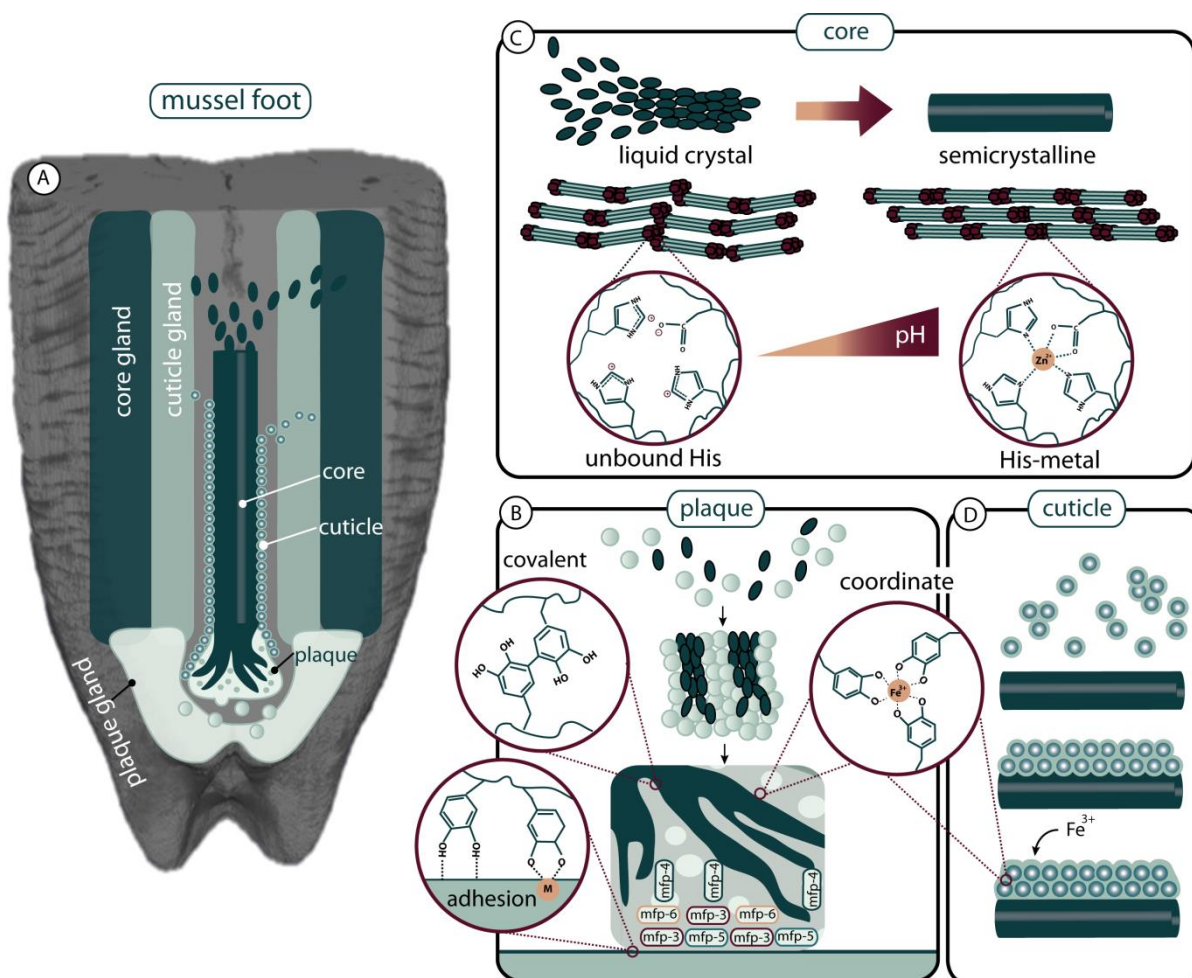


Figure 5. Schematic overview of thread formation.

A) Threads are formed individually within the ventral groove of the mussel foot. The protein building blocks of the threads' different functional parts (plaque, core and cuticle) are produced and stored in specific glands. They are secreted into the groove and distal depression where they self-assemble into a thread. B) The DOPA-rich plaque proteins are secreted in a highly spatially and temporally regulated manner and utilize a range of different interactions, such as DOPA-metal coordination, hydrogen bonding as well as covalent bonds to mediate adhesion and cohesion, respectively. C) PreCols are stored in core vesicles as a liquid crystal phase. Increasing pH likely triggers their self-assembly into a semicrystalline fiber and the formation of His-metal coordination bonds. D) Cuticle vesicles self-organize into a thin layer on the assembled core and are later cross-linked via DOPA-metal coordination.

The formation of the protective cuticle is the final step before the groove opens its seal and releases its fibrous product. The cuticle gland is located closely to the surface of the mussel foot extending along the ventral groove on both sides and contains membrane-bound spherical vesicles of 0.8 – 1.2  $\mu\text{m}$  length (Figure 4).<sup>75</sup> Cuticle vesicles can easily be recognized by their electron-dense core with mottled round shapes or whorls and one or more outer layers.<sup>73</sup> Their complex ultrastructure and different lability to protease treatment strongly suggests the presence of different components.<sup>73</sup> Although the existence of other proteins in the cuticle gland was recently confirmed, their localization within the secretory vesicles remains elusive due to the very small length scales

involved.<sup>53</sup> It was proposed that the characteristic biphasic granular structures found in the thread cuticle are the result of a maturation process, which secretory vesicles might undergo before secretion.<sup>73</sup> However, the details regarding structural and compositional changes on the granule's way from gland to native thread require further thorough investigations. A recent study of artificially induced thread formation revealed that cuticle vesicle merge and coalesce in the groove and encase the core with a thin layer (Figure 5 D).<sup>40</sup> The cuticle's mechanical stability was shown to highly depend on a network of DOPA-Fe<sup>3+</sup> cross-links, which was proposed to form due to a pH jump from acidic to basic conditions, similarly to the His-metal coordination in the core.<sup>25,28</sup> However, *in situ* Raman spectroscopy of induced thread formation revealed no evidence for the presence of DOPA-metal coordination and suggest that they might not be relevant for cuticle assembly (Figure 5 D).<sup>40</sup> The cuticle assembly and its involved components might be the least understood part of thread formation and obliges further examination of all associated processes.

### 3.3 Established methods for byssus examination

Our detailed knowledge about the byssal thread ultrastructure and the subcellular organization of its forming system are based on profound investigations that started more than fifty years ago.<sup>84</sup> At that time, only a minor portion of the present comprehensive knowledge regarding byssus and gland tissue biochemistry was available; thus, the pioneering research was mainly of structural nature and in particular based on electron microscopy studies. Along with histochemical tests and enzymatic digestion, TEM investigations identified the three different secretory glands within the mussel foot tissue.<sup>73,75,81,84,85</sup> These studies established an early relationship between the byssal factory and its products by generating a profound understanding of the protein synthesizing cells, the protein storing vesicles and their secretion.

On the other hand, numerous *in vitro* biochemical studies were focused on extraction and characterization of the single building blocks of byssal threads.<sup>52,86-90</sup> The presence of collagenous and polyphenolic proteins was already beyond debate at an early stage of byssus research, yet the key for unraveling the specific protein composition was the development of extraction protocols that overcame the thread's chemical intractability.<sup>91</sup> Homogenization followed by acetic extraction of several proteins and additional pepsin treatment for the extraction of collagens paved the way for a number of analytical methods, such as amino acid analysis, immunohistology and mass spectrometry.<sup>91</sup> *In situ* hybridization was used to localize some of the proteins to the respective gland tissue.<sup>76,77</sup> However, a recent study demonstrated that presumably due to covalent intermolecular cross-links or other modifications, some byssal proteins might not be susceptible to extraction and



purification.<sup>53</sup> By using next generation sequencing, mRNA transcripts of each gland were analyzed and a large group of previously unknown mfps was identified highlighting once more the great complexity of byssal threads.

While we are currently able to access a great deal of information on the origin of byssal components and the final product, little is known about the dynamic assembly process. Artificial induction of thread formation by injection of KCl into the pedal nerve at the base of the mussel foot was already used at an early stage of byssus investigation and presents a useful technique for investigating the assembly processes.<sup>85</sup> For instance, this trick proved helpful in tracking time-regulated secretion of plaque precursor and was recently used to dynamically track morphological and chemical changes during thread formation.<sup>40,45,46</sup> A synergistic combination of histological staining and confocal Raman microspectroscopy was used to localize the thread's building blocks to their respective glands and to obtain spectral fingerprints, thus, revealing critical insights into this complex biological manufacturing process.<sup>40</sup>

Although this study greatly broadened our understanding of the dynamic processes underlying byssal thread formation, there still remain many open questions. During thread assembly, protein precursors undergo a rapid fluid-to-solid transition. Spatially organized vesicles containing pre-packaged thread building blocks were shown to coalesce and self-assemble into locally organized architectures.<sup>40</sup> Physicochemical triggers initiating this transition are likely seawater pH and changes in ionic strength; however, the details remain elusive. Especially our understanding of the cuticle assembly is incomplete, since some of the cuticle components are still unknown. In order to deepen our understanding of phase transitions occurring during thread assembly, it is essential to track changes in the precursors ultrastructure and composition from their production and storage in the tissue to their secretion and self-assembly. Such investigations require a resolution that is beyond the limit of light microscopy techniques. High-resolution TEM combined with EDS can provide new insights on structural and chemical details. However, TEM traditionally is a 2D technique with limited sample thickness, which only allows a fractional analysis of a micron-thick structure. Along these lines, 3D imaging techniques, such as FIB-SEM, became powerful tools for imaging the ultrastructure of large biological samples.<sup>92</sup> Combining both techniques for the investigation of byssus assembly could provide valuable new insights on the structural and biochemical transitions during fluid-to-solid transition.

### 3.4 Mussel-inspired materials

The following section was written for the review article “Mussel Byssus Structure-Function and Fabrication as Inspiration for Biotechnological Production of Advanced Materials” published in the *Biotechnology Journal* (Harrington, M. J., Jehle, F., Priemel, T. 2018, *Biotechnol. J.* 13, 1800133) and adapted for this thesis with the authorization of the co-authors.<sup>19</sup>

Based on the structure-function relationships described in chapter 3.2, many groups have attempted to transfer extracted design principles from the byssus into man-made materials. However, due to the underlying complexity of the natural system, this is easier said than done. While traditional polymers are produced from long chains with repeating monomeric subunits, protein function is determined by specific sequences of amino acids with defined length presenting side chains with different chemical properties. The sequence and length of the proteins determined by natural selection are intimately linked to the higher order hierarchical structure of the materials, which largely determine material properties. Initial efforts to produce mussel-inspired materials took a minimalist approach, reducing the complexity of the byssal proteins to single amino acid moieties.<sup>27,28</sup> In particular, there has been a strong focus on harnessing metal coordination chemistry mediated via histidine and DOPA moieties toward synthetic production of wet adhesives and self-healing materials.<sup>15,16,26-30</sup> This reductionist synthetic approach has been highly successful and the details are well reviewed.<sup>15,16,26</sup> Investigations of the native byssus reveal, if anything, that the desirable material properties are not just the result of a single functional group, but rely on the complex interplay with other residues and hierarchical architecture. Biotechnological processes are promising for production of sustainable polymers under ambient conditions and permit closer mimicry of the complexity inherent in the native system, leaving the functional groups in the context of their natural chemical and structural protein environment.

#### 3.4.1 Materials from extracted byssus proteins

The potential of a biotechnological approach for mussel-inspired materials was demonstrated over a decade ago with purified proteins from the byssus and mussel soft tissue, including mfp-1 and the preCols. For example, preCols extracted and purified from mussel foot tissue of *M. californianus* were easily drawn into fibers with ultrastructure and mechanical properties reminiscent of native byssal threads.<sup>36,37</sup> A drawback of this approach was the very low protein yield - only 1 mg from 30 mussel feet. Alternatively, several groups utilized both basic and acidic partial hydrolysis of crude byssus that resulted in larger amount of relatively impure fibrous byssus material, which could be formed into free-standing water-insoluble films with fibrillary structure and tunable



properties.<sup>93-96</sup> Additionally, Cell-Tak, a formulated protein solution extracted from mussels containing mfp-1 is marketed as a natural adhesive for attaching cells or sections of tissue to a wide range of surfaces. However, mfp-1 faces a similar problem to preCol of inefficient extraction and purification yields.<sup>97</sup> Based on methods developed by Waite and co-workers, it is possible to extract and purify many of the byssus adhesive proteins including mfp-3 and 5.<sup>87,88</sup> Dependent on ionic strength and pH, purified mfp-3 is able to form self-coacervates — a liquid-liquid phase separation proposed to be critical to the formation of the adhesive interface due to low interfacial energy and high density.<sup>20,79</sup> However, the extraction of mfp-3 from mussel feet, like preCol and mfp-1, is labor-intensive and produces low yields, making it impractical for mass-production of bio-inspired adhesives.

### 3.4.2 Materials from recombinant byssus proteins

Recombinant approaches offer promise toward producing higher yields of byssus proteins. Efforts to produce preCols in bacteria have met numerous challenges due to the high degree of post-translational modification (hydroxyproline is critical for the collagen stability); however, by using *Pichia pastoris* as an expression host, Scheibel and co-workers successfully produced preCol-D recombinantly.<sup>34</sup> Similar to preCols extracted from mussel foot tissue, it formed nanofibrils under native conditions; however, this approach currently suffers from the similar low yields of native extraction and needs to be optimized. It has also been possible to recombinantly express the two matrix proteins present within the fibrous core, tmp-1, and ptmp-1.<sup>60,62</sup> It was proposed that both proteins influence the mechanical properties of byssal threads via their direct interactions with preCols.<sup>60,61</sup> Studies with recombinant ptmp-1 demonstrated that the matrix protein mediated via von Willebrand type-A like domains is able to enhance mouse osteoblast cell adhesion and interact with type I collagen, reinforcing its role in thread assembly and function and its potential use as a biomedical adhesive.<sup>98</sup>

Mfp-1, like other byssus proteins, possesses a highly repetitive protein sequence, resulting in a biased amino acid composition that, during recombinant expression, can inhibit cell growth or cause formation of inclusion bodies, leading to low recombinant product yields. In addition, the heavy post-translational modification of mfp-1 (e.g., hydroxylysine and DOPA) presents an additional problem, as DOPA plays an essential role in protein function.<sup>20,99</sup> A strategy to circumvent the inherent challenge of expressing very long and repetitive proteins is the biotechnological production of a shortened construct, in which tyrosine residues are modified to DOPA enzymatically *in vitro* following expression. For example, rfp-1, a truncated variant of mfp-1 comprising only 12 tandemly repeated decapeptides (AKPSYPPTYK) was successfully produced and exploited in several

studies.<sup>33,100,101</sup> Following enzymatic modification of tyrosine to DOPA,  $\text{Fe}^{3+}$  could mediate strong bridging of rfp-1 coated surfaces via DOPA-iron complexation.<sup>101</sup> A potential medical adhesive and sealant based on rfp-1 was developed in which gelation of concentrated rfp-1 solution was mediated either by noncovalent  $\text{Fe}^{3+}$  complexation or quinone-mediated covalent cross-linking, resulting in tunable viscoelastic and self-healing behavior.<sup>33</sup> The pH sensitivity of the DOPA- $\text{Fe}^{3+}$  complex was exploited to develop an electrospraying process to synthesize polymer nanoparticles based on rfp-1 and doxorubicin, a commercial anti-breast-cancer drug, in which drug release was induced via pH-dependent changes in DOPA-metal coordination.<sup>100</sup> The nanoparticles were efficiently taken up by cells and drug release resulted in a cytotoxic effect on the cancer cell line. Additionally, truncated versions of mfp-1 were used to investigate the role of charge in the mechanism underlying complex coacervation of byssal thread proteins.<sup>80,102</sup>

Based on their role in adhesion, mfp-3 and mfp-5 have become attractive targets for biotechnological production of underwater glues (e.g., for biomedical applications), especially as they are biocompatible and biodegradable. The biotechnological production of mfp-5 was reported more than ten years ago and used as a bio-adhesive for cell biological applications.<sup>103</sup> By fusing recombinant mfp-5 with two domains of an antibody-binding protein, it was also possible to immobilize antibodies onto surfaces.<sup>104</sup> To address issues of protein yield, a novel fusion protein fp-151 was developed with six mfp-1 decapeptide repeats at each terminus of mfp-5, exhibiting significantly greater yields and the potential to be used as a tissue bio-adhesive and even an electrospun scaffold for biomedical applications.<sup>38,105,106</sup> To further promote the potential of fp-151 in the biomedical arena, an RGD cell-adhesion recognition motif was fused with the C-terminus resulting in improved cell-adhesion and spreading abilities.<sup>107</sup> Other extracellular matrix (ECM) peptides stemming from fibronectin, laminin and type IV collagen were also fused to fp-151, demonstrating the potential of this approach for adhesives for cell culture and tissue engineering.<sup>108</sup> The potential role of complex coacervation in mfp-3 and mfp-5 mediated adhesion was also investigated using fp-151, as well as fp-131, a recombinant protein containing six decapeptides of mfp-1 at both termini of mfp-3.<sup>47</sup> By using hyaluronic acid as an anionic counterpart both formed complex coacervates, which enhanced the adhesive strength of the material twofold. In an effort to circumvent challenges involved in the efficiency of enzymatic post-translational modification of tyrosine to DOPA in recombinant mussel proteins, researchers have also been able to incorporate DOPA during recombinant expression via misaminoacylation of DOPA to the tyrosine tRNA.<sup>109</sup> This resulted in a higher DOPA content compared with enzymatic methods and a concomitant increase in adhesive properties.



### 3.4.3 Materials from byssus peptides

An alternative approach to recombinant expression is peptide synthesis, in which short stretches of protein sequence (less than 40 amino acids) are utilized. Peptides allow a more minimalist approach that still leaves functional amino acid groups in the relevant biochemical context of their native sequence. For example, short but representative regions of mfp-3 were harnessed to elucidate the role of amino acids other than DOPA in coacervation and adhesion.<sup>48</sup> Although shorter, the resulting peptide possessed the main characteristics with abundant positively charged and aromatic residues. To shed light on DOPA's role in adhesion and coacervation, peptides with modified and unmodified tyrosine were investigated. Notably, the DOPA-modified peptide formed a single-component coacervate promoting faster initial adsorption kinetics and enhanced adsorption.<sup>48</sup> A similar approach using different peptides based on mfp-5 in which tyrosine residues were enzymatically modified to DOPA demonstrated that synergistic effects between amino acids over the whole protein sequence are crucial for the strong adhesion of mfp-5.<sup>110</sup> Taken together, these studies demonstrate that mussel-inspired peptides can be a valuable alternative to recombinant full-length constructs when addressing specific research questions.

In fact, several peptide-based studies investigated the preCol HRDs, with a specific focus on their role in pH-dependent self-assembly and mechanical performance of threads.<sup>21,23,31</sup> For example, the reversible adhesive self-interaction of HRDs mediated via His-metal coordination was studied using PEG-based soft colloidal probes (SCPs) coupled with spectroscopic analysis (Figure 6 A).<sup>111</sup> The study provided clear evidence for metal coordination bonds as load-bearing reversible cross-links in the byssus and their role in mechanical properties and self-healing behavior. Furthermore, comprehensive spectroscopic investigations of two different evolutionary conserved sequence motifs in preCol HRDs ( $[HA]_n$  and  $[HGGG]_n$ ) revealed that HRDs undergo pH and concentration responsive transitions in conformational structure.<sup>83</sup> The observed transitions, which are highly relevant to the assembly and biological function of the byssus, occurred independent of metal ions; however it was suggested that they provide defined bonding geometries for metal ions, which are crucial for the self-healing behavior based on sacrificial bonds.<sup>83</sup>

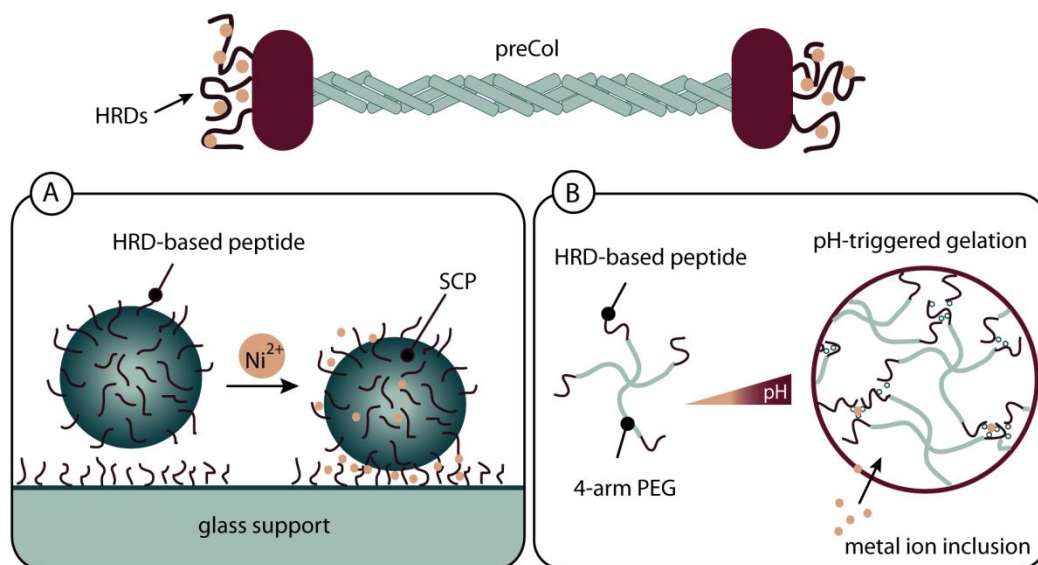


Figure 6. HRD-peptide based studies.

A) Schematic representation of adhesive self-interaction of HRD-based peptides in the absence and presence of metal ions using PEG-based soft-colloidal probes (SCPs). B) PH- triggered reversible hydrogel formation based on hybrids of PEG and HRD-based peptides.

The pH-dependent fluid-to-fiber transition of preCol building blocks is believed to be triggered by the HRDs. In order to shed light on the physicochemical triggers of this process, polymer-peptide hybrids were used and the formation of hydrogels was triggered by pH elevation mimicking the natural assembly process (Figure 6 B).<sup>112</sup> Similar to the previously discussed study, spectroscopic analysis revealed a conformational transition of peptide groups into  $\beta$ -sheet crystalline structure, which mediated gelation via cross-linking the polymer backbone.<sup>112</sup> Furthermore, inclusion of metal ions increased the viscoelastic damping of the gels, a process that is also proposed for the native byssal threads. These HRD-based peptide studies provided valuable new insights into the molecular and physicochemical bases of byssal thread self-assembly and mechanical function. Along these lines, HRD-based peptides were utilized to produce a mussel-inspired material by imitating the natural assembly processes of byssal threads. The study, which is described in the following chapter, aims at improving structural complexity of synthetic mussel-inspired materials and, as a result, the material properties.

Taken together, the mussel byssus is a fascinating high-performance fiber that exhibits excellent mechanical properties, such as high hardness, high extensibility, self-healing and underwater-adhesion. During the past decades, an excellent understanding of the complex relationship between the structural organization of the byssal proteins and the mechanical performance of threads was established. Ever since, the byssus served as inspiration for countless materials aiming to reach its outstanding properties. Most of them focused on the thread's



distinctive metal-coordination chemistry. However, the example of artificial spider silk has taught us that it is essential to understand the physical and chemical parameters guiding the rapid self-assembly of such complex high-performance fibers in order to improve upon current mussel-inspired materials. Along these lines, the following three chapters describe the results of the attempt to develop a mussel-inspired material by utilizing natural sequences, thereby keeping functional groups in their native context (chapter 4) and performing a fundamental investigation of the byssus cuticle (chapter 5) and its natural assembly process (chapter 6).

#### 4. METAL-TUNABLE SELF-ASSEMBLY OF HIERARCHICAL STRUCTURE IN MUSSEL-INSPIRED PEPTIDE FILMS

The following section was written for the article “Metal-tunable Self-assembly of Hierarchical Structure in Mussel-inspired Peptide Films” published in ACS Nano and adapted for this thesis with the authorization of the co-authors.<sup>113</sup>

The byssus exhibits impressive material properties (high toughness, self-healing, wet adhesion), which are linked to the rapid self-assembly of specific protein building blocks into a hierarchical architecture at different length scales. In particular, the self-healing fibrous core of byssal threads is composed of collagenous protein building blocks called preCols (Figure 7 A), which assemble into a semicrystalline organization within minutes following secretion.<sup>21,22,40</sup> The current assembly model suggests that preCol proteins are stored in a LC phase in secretory vesicles under acidic conditions, and the transition to basic seawater pH triggers the coalescence of vesicles and the transition from LC phase to a stiff fiber with highly defined structural organization (Figure 7 A).<sup>40</sup> It is proposed that this fluid-to-solid transition is mediated via the N- and C-terminal HRDs of the preCols, which possess an elevated histidine content ( $\sim 20$  mol %), making them highly sensitive to pH changes in the range of pH 4 to 8 and endowing them with the capacity to coordinate transition metal ions (e.g.,  $Zn^{2+}$ ,  $Cu^{2+}$ ,  $Ni^{2+}$ ) in highly defined complexes.<sup>17,21,23,83</sup> In support, recent work revealed that peptides based on HRDs undergo a fast pH-triggered self-organization into an amyloid-like cross- $\beta$ -sheet structure when brought to pH 8.<sup>83</sup> In addition to their role in self-assembly, histidine–metal coordination bonds mediated by the HRDs contribute significantly to the high toughness and self-healing behavior of byssal threads, behaving as strong but reversible sacrificial cross-links.<sup>17,23,24,63,111</sup> Based on this finding, a number of groups have produced polymeric materials and hydrogels stabilized by histidine–metal coordination, which exhibit interesting dynamic mechanical and self-healing properties.<sup>27,29,30</sup> However, up to this point, the resulting synthetic materials have mimicked only the chemistry of the byssus and completely lack the structural complexity. Not surprisingly, these materials also do not achieve the performance of the natural material, likely stemming from the fact that the metal-binding groups are taken out of the context of the amino acid sequences in which they are embedded in the natural material.

In an effort to overcome this limitation, the goal of the current study is to imitate natural assembly processes to improve structural complexity of synthetic materials and, as a result, the material properties. Inspired by the multifunctional role of HRDs in byssus self-assembly and function, I utilized peptides based on the natural sequence of HRDs and demonstrate a pathway for



the production of complex nanostructured materials. Taking advantage of the pH sensitivity of the HRDs, I developed a protocol to form free-standing films from HRD peptides at basic pH both in the absence and presence of metal ions (Figure 7 B).

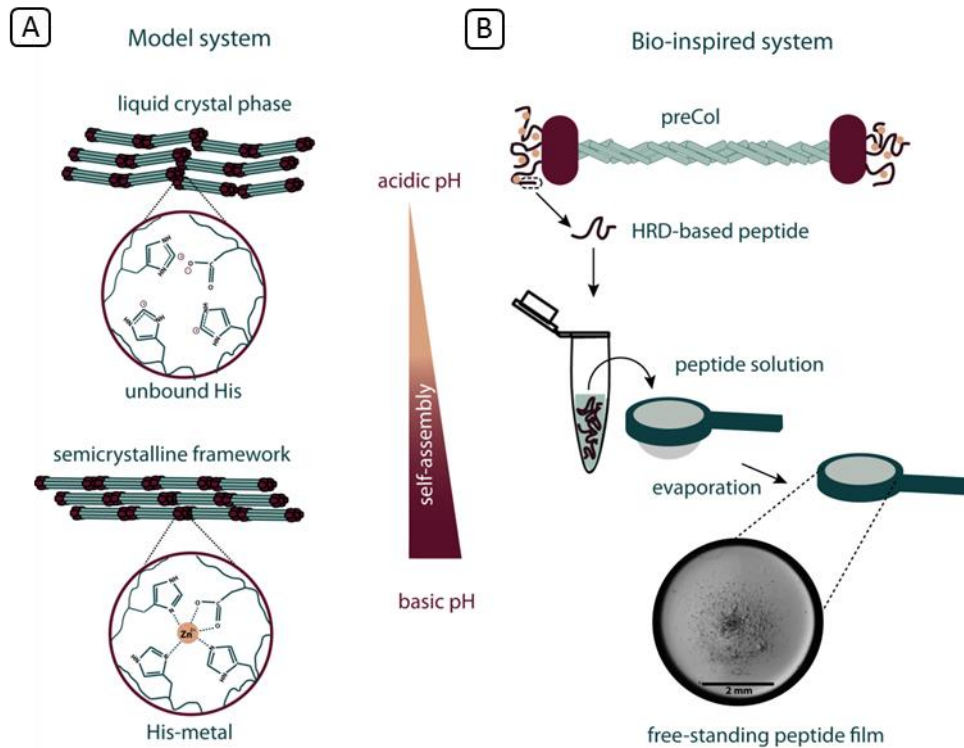


Figure 7. Self-assembly of the mussel byssal thread and the bioinspired system.

A) Byssal thread distal region consists of preCol proteins with different functional domains. HRDs at the preCol termini trigger self-assembly of the thread core in a pH-dependent manner. At acidic pH, preCol proteins are stored in a liquid-crystalline phase where histidine residues are protonated and unbound. A pH change toward basic conditions triggers the self-assembly of preCol proteins into a semicrystalline framework, and deprotonated histidine residues are able to coordinate metal ions and thus to form sacrificial bonds. B) Synthetic peptides based on the HRDs of preCol proteins are dissolved at acidic pH and spontaneously self-assemble into free-standing peptide films at basic pH.

Spectroscopic and X-ray diffraction investigations indicate that, similar to the byssus, this approach leads to complex multiscale structures that can be cross-linked and fortified via histidine–metal complexes. Moreover, the here presented results demonstrate that this approach enables one to tune both the higher order structure and the mechanical properties of the films depending on the processing and inclusion of metal ions. This work establishes mussel HRD peptides as versatile natural building blocks for fabricating biomaterials.

## 4.1 Material & Methods

### 4.1.1 Film Formation

The mussel-derived HRD-based peptides were synthesized and characterized by Pepscan (Lelystad, Netherlands). Peptides were dissolved in distilled water (10 mg/mL) and mixed with 100 mM ZnCl<sub>2</sub> or 100 mM CuCl<sub>2</sub> solution in a ratio of 3 His/1 Zn<sup>2+</sup> or 3 His/1 Cu<sup>2+</sup>. The pH of the peptide solution was adjusted to 6.5 by the addition of 0.1 M NaOH. Films were then formed by transferring 50 µL of the peptide solution into an inoculation ring of 4 mm in diameter and evaporating for approximately 12 h at room temperature. In order to form less brittle films for mechanical characterization, 1 % glycerol was added and film formation was carried out as previously described.

### 4.1.2 Fourier Transform Infrared Spectroscopy

FTIR spectra were recorded using a Bruker Tensor spectrometer (Ettlingen, Germany) equipped with a liquid N<sub>2</sub>-cooled mercury cadmium telluride detector. Film formation was carried out as previously described. In order to obtain thinner films that are also suitable for measurements in transmission mode, only 35 µL of peptide solution were used. At least five measurements at different spots were acquired for each film in transmission and absorption mode. Infrared spectra were baseline corrected and the region around the amide I band was cropped using OPUS 7.0.

### 4.1.3 Raman Spectroscopy

Raman spectroscopic measurements were performed to characterize the secondary structure of peptides and metal coordination in films in the absence and presence of metal ions. Spectra were obtained with a Confocal Raman Microscope (alpha300, WITec, Germany) equipped with a piezo-scanner (P-500, Physik Instrumente, Karlsruhe, Germany). Raman measurements were performed on films with the incident beam perpendicular as well as parallel to the film plane. A linear polarized laser (Nd:YAG laser,  $\lambda = 532$  nm) was focused on the sample through a 10x (Nikon, Düsseldorf, Germany, NA = 0.40; measurements orthogonal to film plane) or 60x objective (measurements parallel to film plane) (Nikon, Düsseldorf, Germany) and the Raman scattered light was detected by an thermoelectrically cooled CCD detector (DU401A-BV, Andor, Belfast, North Ireland). Spectra were acquired with an integration time of 0.5 s and 60 accumulations and either 0° or 90° polarization. The ScanCtrlSpectroscopyPlus software (Witec, Ulm, Germany) was used for the measurement setup and OPUS 7.0 for baseline correction and smoothing.



#### 4.1.4 X-ray Absorption Near Edge Spectroscopy (XANES)

X-ray absorption spectroscopy (XAS) was performed at beamline LISA at the ESRF (Grenoble, France). Peptide films in the presence of  $\text{Zn}^{2+}$  were formed as previously described. In order to have enough material, two films were placed between two Kapton© foils and the sample was mounted in a metal holder. XAS spectra were recorded in fluorescence mode using a 12-element high purity germanium radiation detector (ORTEC, Tennessee, United States). During each measurement a Zn metal foil was recorded simultaneously in transmission for energy calibration purposes. The data were collected at the  $K\alpha$  edge of Zn (9659 eV) with a ring current between 160 and 200 mA using the following settings (energies relative to edge position): the pre-edge region from -200 to -30 eV was sampled with steps of 10 eV and the XANES region from -30 to 200 eV was sampled with steps of 0.5 eV. For each data point the exposure time of the fluorescence detector was at least 10 s. During data collection, the samples were kept at a temperature of 83 K to reduce the thermal molecular vibrations and beam damage. In total, three spectra were collected and averaged. The XAS spectra were analyzed with the Athena module of the Demeter XAS software package. For each spectrum the energy calibration was performed according to the simultaneously collected spectrum of a Zn metal foil standard. Then all spectra obtained from one sample were aligned, merged and normalized.

#### 4.1.5 X-ray Diffraction

X-ray diffraction experiments were carried out on the  $\mu$ Spot beamline at the synchrotron source Bessy II (Berlin Elektronenspeicherring GmbH, Berlin, Germany) with an X-ray wavelength of 0.82656 Å and a spot size of 50  $\mu\text{m}$ . Films were measured with their film plane parallel and perpendicular to the X-ray beam using an integration time of 10 s at a sample detector distance of 327 mm determined by calibration using a quartz standard. Acquired diffraction patterns were analyzed using the Fit2D software.<sup>114</sup> An empty background was subtracted from all sample images and d spacings of the reflections were determined by integrating intensity using the cake function of Fit2d.<sup>114</sup>

#### 4.1.6 AFM-based Indentation

Due to the high brittleness of HRD-based peptide films, 1% glycerol was added to the peptide solution as a plasticizer. Mechanical characterization of peptide films was performed under wet conditions (10 mM PIPPS buffer, pH 8) on a Nanowizard III atomic force microscope (AFM) (JPK Instruments AG, Berlin, Germany). The AFM head was mounted on an optical microscope (IX71, Olympus, Japan) with phase contrast optics (objective 63x / 1.25 Oil Ph3, Antiflex EC "Plan-Neofluar", Carl Zeiss AG, Germany). To record spatially resolved height and modulus data, peptide films were

mapped by an array of AFM force-distance measurements in a 10  $\mu\text{m}$  x 10  $\mu\text{m}$  large grid with  $\sim$  4096 indentations and at least 5 measurements at different spots for each sample. Partial Au coated quartz-like cantilevers (Nanosensors™ qp-BioAC-20, Switzerland) with a spring constant of 0.15 - 0.55 N/m were used. The measurements were performed at constant force of 10 nN. The reduced modulus was calculated from the elastic response of the peptide films indented by the AFM tip using the JPKSPM data processing program and a Hertz model for data fitting. The tip shape was assumed as paraboloid with a radius of 10 nm and a Poisson ratio of 0.5 was assumed.

## 4.2 Results

### 4.2.1 Sequence Selection and Film Formation

The peptide HRD-DN (N-AVAHAHAHAHASAGANGRARAHA-C) used in this study is based on the N-terminal histidine-rich domain of preCol-D, a protein that is found in the distal region of *Mytilus* species byssal threads.<sup>17</sup> This sequence was chosen because it represents a common tandemly repeated motif [HA]<sub>n</sub> that was previously shown to strongly influence conformational structure and metal-binding geometry in HRDs and is therefore believed to play a major role in self-assembly of hierarchical structure in byssal threads.<sup>83</sup> The synthesized and purified ( $\sim$  98 %) peptide was dissolved in dH<sub>2</sub>O ( $\sim$  4 mM), and the pH of the solution was increased to 6.5 in order to avoid metal precipitation occurring at more basic conditions. In the absence and presence of metal ions (His : Zn<sup>2+</sup>/Cu<sup>2+</sup> ratio = 3:1), peptides spontaneously assembled into thin, free-standing films inside a polystyrene ring following slow evaporation. Once formed, it was not possible to dissolve the films at high pH; however, at slightly acidic pH, the films were resolubilized, indicating that noncovalent interactions are responsible for the film stability. Furthermore, films could then be cast from the dissolved film solutions using an identical protocol. Consistent with recent findings, HRD-based peptides were able to self-assemble in the absence of metal ions but in a highly pH-dependent manner.<sup>83</sup> Combined spectroscopic methods were used to obtain specific chemical and structural information on self-assembled peptide films.

### 4.2.2 Fourier Transform Infrared (FTIR) and Raman Spectroscopy

FTIR and Raman spectroscopy are commonly used to investigate the secondary structure of peptides and proteins as they are sensitive to the backbone confirmation. By applying both complementary techniques, we can extract important information about the biochemistry and secondary structure of HRD-based peptides inside free-standing films at the nanoscale. All major



peaks observed in the amide I region (1600–1700  $\text{cm}^{-1}$ ) of FTIR spectra (Figure 8 A) can be assigned to  $\beta$ -sheet structures or turns. The sharp peak at lower spectral position (1626  $\text{cm}^{-1}$ ) indicates a high degree of crystallinity stemming most likely from shorter hydrogen bonds between  $\beta$ -strands.<sup>115,116</sup> Notably, the addition of  $\text{Zn}^{2+}$  and  $\text{Cu}^{2+}$  resulted in a decrease of peak intensity (1626  $\text{cm}^{-1}$ ), indicating a higher degree of crystallinity in films where metal ions are absent. This observation is contrary to previously published data that suggested the formation of amyloid  $\beta$ -sheet structures of HRD-based peptides at low dilutions is increased by the addition of  $\text{Zn}$ .<sup>83</sup> However, in the current work, the secondary structure of peptides was investigated in solid films at high concentrations. In addition, all three spectra show peaks at higher wavenumbers (1696  $\text{cm}^{-1}$ ) that can also be assigned to  $\beta$ -sheets.<sup>115</sup> Spectral positions of additional smaller peaks for films containing metals ions (1668  $\text{cm}^{-1}$ ) and films that were formed in the absence of metals (1678  $\text{cm}^{-1}$ ) suggest the presence of  $\beta$ -turns. Consistent with FTIR spectroscopy, confocal Raman spectra of peptide films (Figure 8 B) exhibit intense and distinct amide I (1673  $\text{cm}^{-1}$ ) and amide III bands (1236  $\text{cm}^{-1}$ ) that can be assigned to  $\beta$ -sheet structures.<sup>117</sup> Notably, the amide I band of films formed in the presence of  $\text{Cu}^{2+}$  (Figure 8 B) appears slightly broader, indicating that  $\beta$ -sheet structures might be less prominent in the presence of  $\text{Cu}^{2+}$ .

It was previously demonstrated that metal ions interact strongly and specifically with HRD peptides.<sup>83</sup> While FTIR spectroscopy is limited to structural information, Raman spectroscopy can also provide insights into metal coordination chemistry because it is sensitive to the protonation, coordination, and tautomer of histidine.<sup>118</sup> In the absence of metal ions (Figure 8 C), a characteristic Raman band at 1571  $\text{cm}^{-1}$  was observed in peptide films that can be assigned to the deprotonated  $\text{N}_{\tau}\text{-H}$  form of histidine residues.<sup>118</sup> Raman spectra of peptide films in the presence of  $\text{Zn}^{2+}$  and  $\text{Cu}^{2+}$  (Figure 8 C), however, exhibit instead a strong band at 1603  $\text{cm}^{-1}$  that is characteristic of the presence of the His-metal tautomer [ $\text{N}_{\tau}\text{-M}$ ;  $\text{N}_{\pi}\text{-H}$ ].<sup>118</sup> Furthermore, the appearance of a minor peak at 1555  $\text{cm}^{-1}$  may indicate the presence of a metal-bridging imidazolate form [ $\text{N}_{\tau}\text{-M}$ ;  $\text{N}_{\pi}\text{-M}$ ]. Notably, this peak is less prominent in films containing  $\text{Cu}^{2+}$ , indicating fewer His-metal bridges.

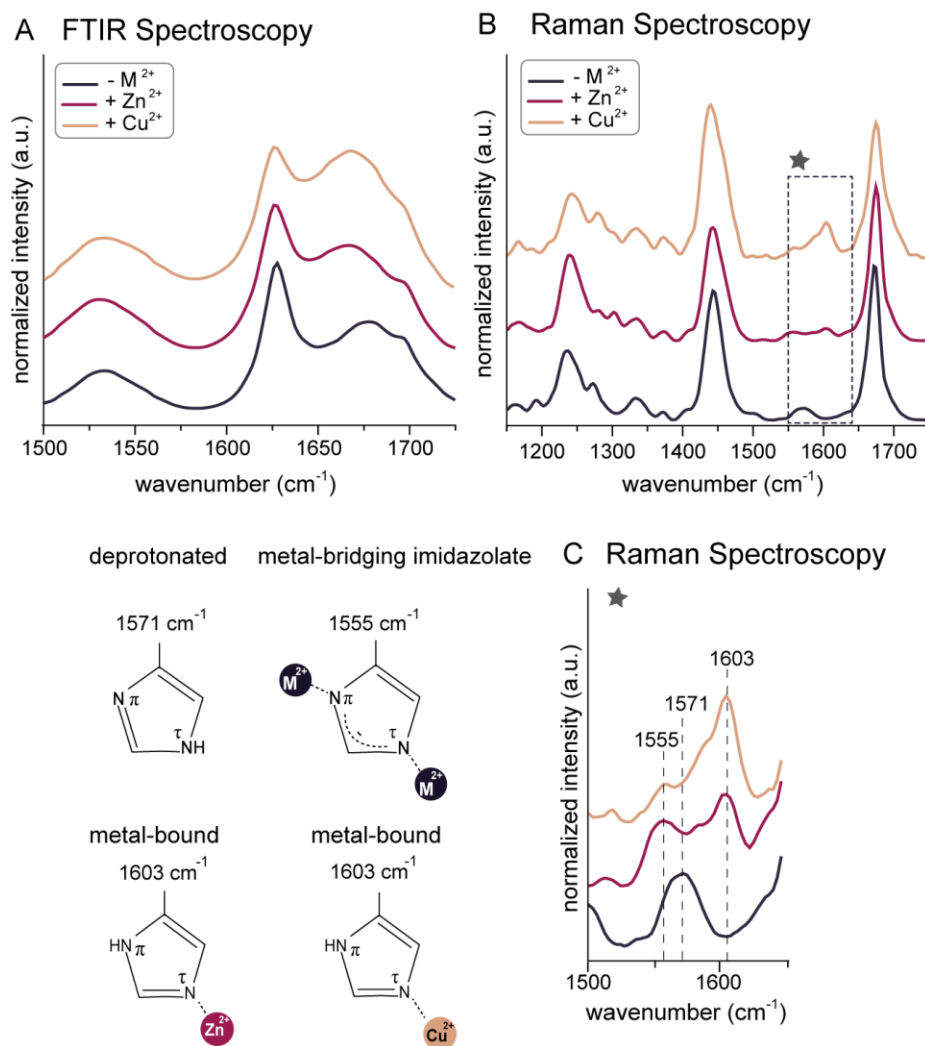


Figure 8. HRD-based peptides spontaneously assemble into amyloid  $\beta$ -sheet structures.

A) FTIR spectra of HRD-DN peptide films in the absence (blue) and presence of  $\text{Zn}^{2+}$  (red; His/Zn  $\sim$  3:1) and  $\text{Cu}^{2+}$  (beige; His/Cu  $\sim$  3:1). All spectra show peaks that can be assigned to  $\beta$ -sheet structures or turns. B) Raman spectra of HRD-DN peptide films in the absence (blue) and presence of  $\text{Zn}^{2+}$  (red; His/Zn  $\sim$  3:1) and  $\text{Cu}^{2+}$  (beige; His/Cu  $\sim$  3:1). C) Characteristic peaks at 1555, 1571, and 1603  $\text{cm}^{-1}$  correspond to metal-bridging imidazolate, deprotonated histidine, and its metal-bound forms, respectively.

#### 4.2.3 X-ray absorption spectroscopy (XAS)

In addition, the specific histidine metal coordination environment in peptide films containing  $\text{Zn}^{2+}$  was further investigated by X-ray absorption spectroscopy (XAS) and compared to reference samples that coordinate Zn ions by histidine residues. XAS provides specific information about the coordination sphere of a specific metal ion, in this case Zn, and has been previously utilized for analyzing His–Zn coordination in mussel byssal threads and HRD peptides.<sup>23,83</sup> Two distinct peaks (9664 and 9671 eV) in the XANES (X-ray absorption near-edge structure) region of the Zn K-edge XAS spectra suggest a well-defined bond geometry of His-metal-binding sites (Figure 9). Furthermore, it was previously shown that the intensity of the Zn K-edge white line is indicative of the coordination

number of Zn. The intensity of the measured Zn K-edge white line is  $\sim 1.4$ , which is typically indicative of tetrahedral coordination by four ligands.<sup>119</sup>

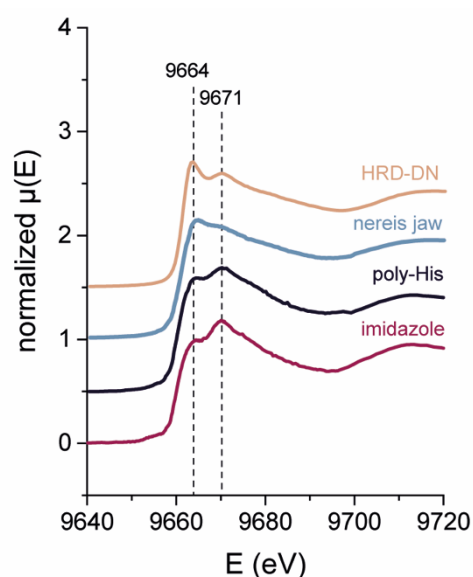


Figure 9. XANES spectra of HRD-based peptide film and Zn references. Normalized Zn K-edge XANES spectrum of HRD-based film (beige) containing Zn in a ratio 3:1 and references nereis jaw (light blue), polyhistidine : Zn mixture (2:1 His : Zn) (dark blue) and imidazole (red). The vertical dashed lines are intended for easy comparison of the double peak feature among various curves.

Taken together, these complementary spectroscopic investigations reveal that HRD-based peptides spontaneously assemble into films composed of metal-binding amyloid-like  $\beta$ -sheet structure during the evaporation process, which is consistent with previous studies on the role of pH and metals in mussel byssus formation.<sup>83</sup>

#### 4.2.4 Polarized Raman Spectroscopy

To further investigate the hierarchical architecture of peptides in HRD-based peptide films, polarized Raman spectroscopy was performed. Since the amide I band mainly arises from stretching vibrations of C=O bonds in the peptide backbone, it is possible to determine backbone orientation inside the film using polarized light aligned parallel ( $0^\circ$ ) and perpendicular ( $90^\circ$ ) to the film plane during confocal Raman spectroscopic measurements.<sup>117</sup> When exposed perpendicular to the beam, polarized Raman spectra (Figure 10 A) of HRD-based peptide films that were formed in the absence and presence of  $\text{Zn}^{2+}$  appear to be similar and therefore do not indicate oriented peptide backbones.

However, when  $\text{Cu}^{2+}$  was added,  $\beta$ -sheets seem to be slightly oriented because the amide I shows marginal differences in relative band intensities under polarized light. In contrast, polarized Raman spectra of HRD-based peptide films measured with the beam parallel to the film plane show explicit differences in relative band intensities (Figure 10 B). The proportion of the intensity of amide

I and amide II bands seems to be reversed when comparing spectra obtained at 0 and 90° polarization. More specifically, the amide I band is much more prominent when polarized parallel to the film plane (0°), indicating that C=O groups are oriented parallel to the film plane, which suggests that  $\beta$ -sheets are likely stacked with their backbones parallel to the film plane. Notably, the intensity of the peak at 1571  $\text{cm}^{-1}$ , which is assigned to the deprotonated form of histidine, is also affected when changing the polarization (Figure 10 B). The same observation can be made for the Zn-binding form of histidine at a wavenumber of 1603  $\text{cm}^{-1}$  (Figure 10 B). This intensity difference is not present in  $\text{Cu}^{2+}$ -treated films. Considering that peaks corresponding to the different coordination forms of histidine arise from vibrations of the C4=C5 bond in the imidazole side chain, the results further suggest that the C4=C5 bond of histidine is oriented perpendicular to the film plane.<sup>118</sup> The observation that polarization dependency is much less prominent in films formed in the presence of  $\text{Cu}^{2+}$  indicates a less ordered hierarchical structure, which is consistent with all previously discussed data.

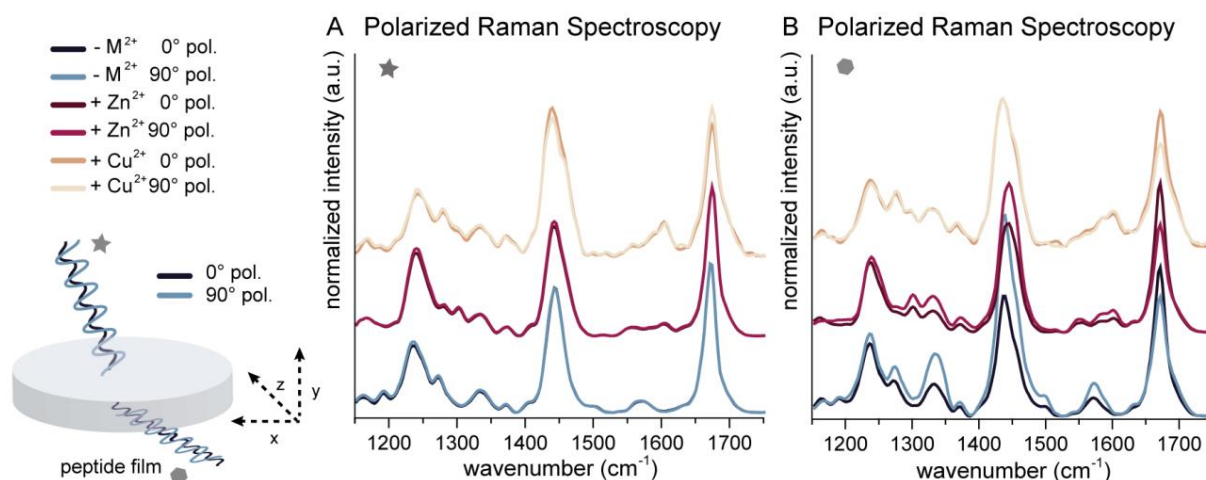


Figure 10. Stacking of  $\beta$ -sheets in HRD-based peptide films.

A) Raman spectra of HRD-DN peptide films in the absence (blue) and presence of  $\text{Zn}^{2+}$  (red; His/Zn  $\sim$  3:1) and  $\text{Cu}^{2+}$  (beige; His/Cu  $\sim$  3:1) under polarized light (0° (dark color) and 90° (light color)). B) Films that were measured with the beam parallel to the plane of the film (indicated by hexagon) show explicit differences in relative band intensities, indicating a highly oriented backbone structure.

#### 4.2.5 X-ray Diffraction

In light of the results obtained by polarized Raman spectroscopy, X-ray diffraction (XRD) was performed to obtain more detailed information about the film's hierarchical architecture at the nanoscale. For this purpose, the peptide films were investigated using the previously described beam configurations. Diffraction patterns from peptide films measured with the beam perpendicular to the film plane show reflections at  $d = 0.46$  nm with nearly equal intensities at all azimuthal angles corresponding to the inter-strand spacing of  $\beta$ -sheets (Figure 11 A-C).<sup>120,121</sup>

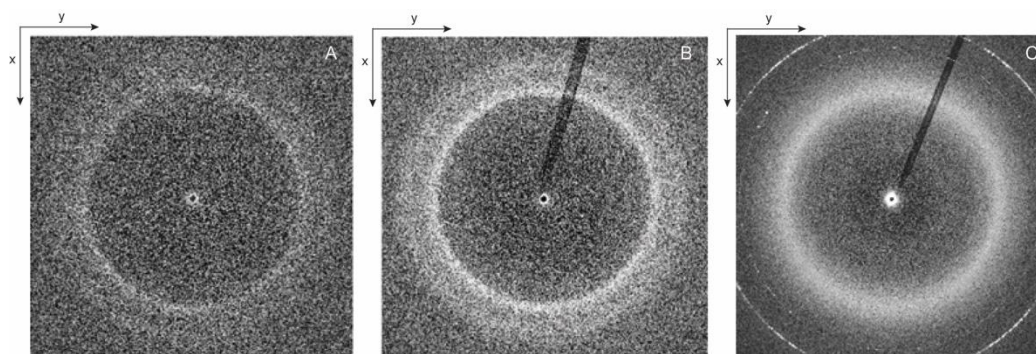


Figure 11. XRD patterns of HRD-based peptide films.

Films formed in the absence (A) and presence of metals (B, C) were exposed to the incident beam perpendicular to the film plane. XRD patterns of all three peptide films show diffuse rings with nearly equal intensity at all azimuthal angles (A, B, C). However, in the presence of  $Zn^{2+}$  (B) and  $Cu^{2+}$  (C), the ring at  $d = 0.46$  nm indicating  $\beta$ -sheet structure appears somewhat stronger than in the absence of metal ions.

The results are consistent with the spectroscopic investigations and support the hypothesis that  $\beta$ -sheets are not oriented in plane. Consistent with the findings from polarized Raman spectroscopy, however, diffraction patterns of films that were measured with their plane parallel to the incident beam show a very distinct alignment of structures (Figure 12 A-C) similar to wide-angle X-ray diffraction (WAXD) pattern of amyloid materials. The distinguishing feature of amyloid  $\beta$ -sheet structures is a cross- $\beta$  pattern that consists of characteristic diffraction signals oriented perpendicular to one another.<sup>120</sup> Similarly, the observed WAXD pattern of HRD-based peptide films shows reflections oriented along the x- and y-axes of the films.

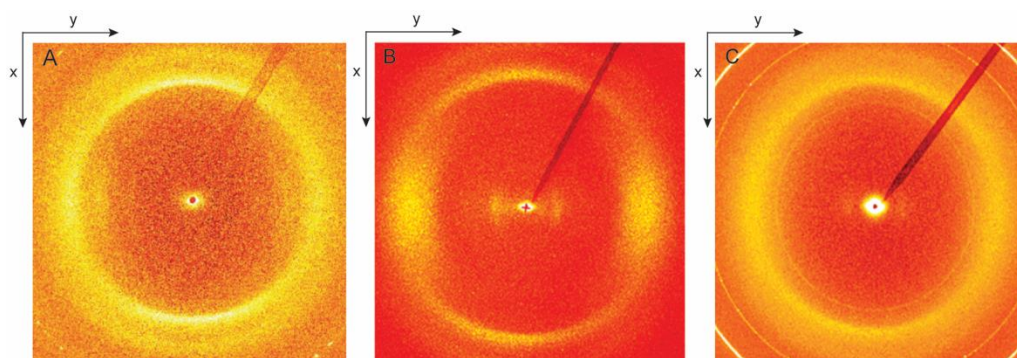


Figure 12. Alignment of structures in HRD-based peptide films.

Diffraction patterns of films that were measured with their plane parallel to the incident beam show a very distinct alignment of structures. A-C) Diffraction patterns of HRD-DN peptide films that were formed in the absence (A) and presence of the metal ions (B)  $Zn^{2+}$  and (C)  $Cu^{2+}$ .

They are mostly oriented along the x-axis (Figure 13 A), suggesting  $\beta$ -sheet structures ( $d = 0.46$  nm) with  $\beta$ -strands parallel to the film plane. Additionally, a second reflection corresponding to  $d = 0.38$  nm can be identified for all three films. A similar reflection ( $d = 0.37$  nm) linked to  $\beta$ -

crystallites was previously observed in spider silk as well as in hagfish protein fibers.<sup>122,123</sup> In addition, a reflection at 0.38 nm spacing was reported for short peptide sequences forming amyloid fibrils.<sup>124</sup> Although the exact origin of the 0.38 nm reflection is still under debate, it can certainly be associated with the observed crystalline  $\beta$ -sheet structure in HRD-based films. Along the  $y$ -axis, there are several strong reflections in the pattern of films without metals and with  $Zn^{2+}$  (Figure 12 A, B). In the absence of metals, distinct reflections at  $d = 0.44$ , 0.56, and 0.84 nm are visible (Figure 13 B) and most probably reveal the presence of stacked  $\beta$ -sheet crystallites. However, when  $Zn^{2+}$  is present, a prominent reflection at  $d = 1.86$  nm is visible that indicates a highly ordered structure based on crystallite formation. The result of the integration (Figure 13 B) reveals a broad, asymmetric peak that most likely consists of several individual peaks. Aside from the wide-angle reflections, the pattern of films without metals and with  $Zn^{2+}$  obtained from small-angle scattering appears homogeneous, suggesting a highly ordered system. In addition to protein-related peaks, sharp rings can be observed in the diffraction patterns of films containing  $Cu^{2+}$  that most likely arise from the presence of salt formation during the film formation process.

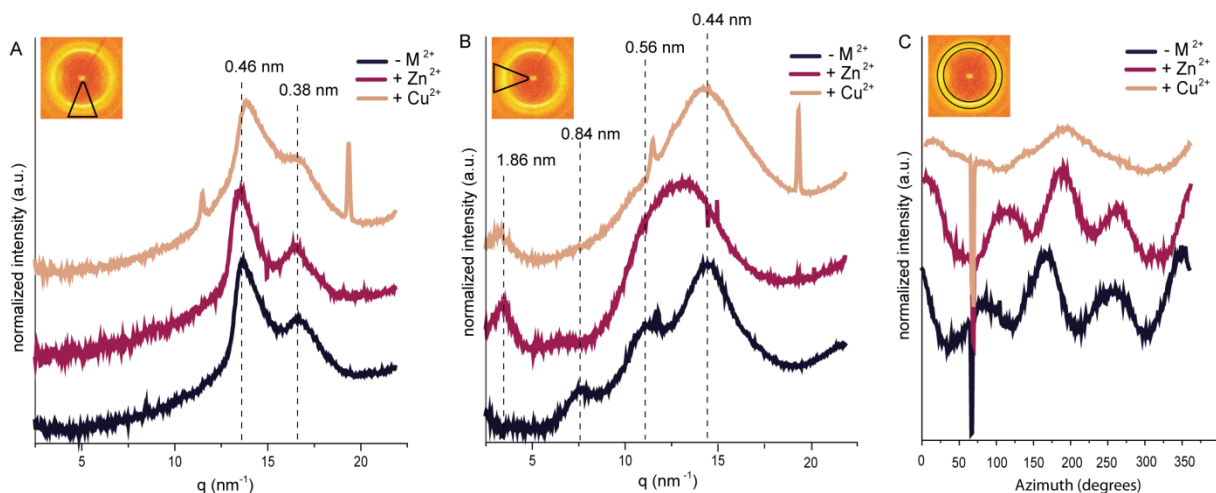


Figure 13. Results of the radial and azimuthal integration of XRD pattern.

A) WAXD reflections oriented along the  $x$ -axis are highly consistent with a cross- $\beta$ -sheet structure with  $\beta$ -strands parallel to the film plane. B) Strong reflections along the  $y$ -axis reveal most likely the  $\beta$ -stacking of a unit cell. Sharp rings in the diffraction pattern and corresponding sharp peaks in the plots arise most likely from salt crystals formed during the film formation process. C) Azimuthal integration of HRD-based peptide film WAXD pattern exhibits four distinct peaks suggesting a distinct alignment of structures in films containing no metal ions or  $Zn^{2+}$ . Films formed in the presence of  $Cu^{2+}$  only show two broad peaks indicating little alignment of structures.

Consistent with the spectroscopic evidence, the diffraction pattern of HRD-DN with  $Cu^{2+}$  (Figure 12 C) shows little alignment, which is illustrated by the azimuthal distribution shown in Figure 13 C and therefore indicates a less ordered system. This is further emphasized by the small-angle X-ray diffraction (SAXD) pattern, which suggests a higher inhomogeneity compared to films without metals and films with  $Zn^{2+}$ . In the presence of  $Cu^{2+}$  (Figure 12 C), the reflections are less prominent



and the integration results show peaks similar to the ones observed for films containing  $\text{Zn}^{2+}$  (Figure 13 B).

Taken together, the results of XRD are consistent with the spectroscopic investigations. Since the observed stacking peaks indicate that crystallites appear to be well-organized along the films y-axis, HRD-based peptides are hypothesized to assemble into an amyloid-like hierarchical architecture that can be tuned with metal ions. Mild shear forces inside the ring likely influence the stacking of peptides along the direction of the y-axis to form a hierarchical ordered structure as it was observed that films do not form when droplets of peptide solution are evaporated on a glass slide. Notably, shear forces are believed to be important in the assembly of hierarchical structure in the native byssal thread.<sup>40</sup> Nonetheless, these results clearly demonstrate that, in addition to the influence of shear forces, the fine-scale nanostructure and resulting mechanical properties of the film can be influenced by inclusion of metal ions.

#### 4.2.6 Mechanical Characterization

Since the link between control of multiscale structure in polymeric materials and their properties is well-established, the mechanical properties of peptide films were investigated using atomic force microscopy (AFM)-based nano-indentation. Due to their crystalline  $\beta$ -sheet structure, peptide films are highly brittle and made mechanical characterization challenging. However, it was shown in previous studies that small amounts of plasticizers like glycerol increased the stability of amyloid protein films, enabling mechanical testing while not greatly influencing the structural properties.<sup>125,126</sup>

Therefore, peptide solution was prepared as previously described, and 1% v/v glycerol was added before transferring the solution inside the polystyrene ring. This method enabled testing the mechanical properties of the films under wet conditions (pH 8) on a glass surface. Because the results of XRD suggest the presence of salt crystals in films containing metals, initially  $10\ \mu\text{m} \times 10\ \mu\text{m}$  areas were probed. Salt crystals appeared as bright spots in resulting AFM maps, and smaller areas ( $2\ \mu\text{m} \times 2\ \mu\text{m}$ ) without crystals were chosen for the final indentation measurements. The typical resulting force – displacement curves are shown in Figure 14.

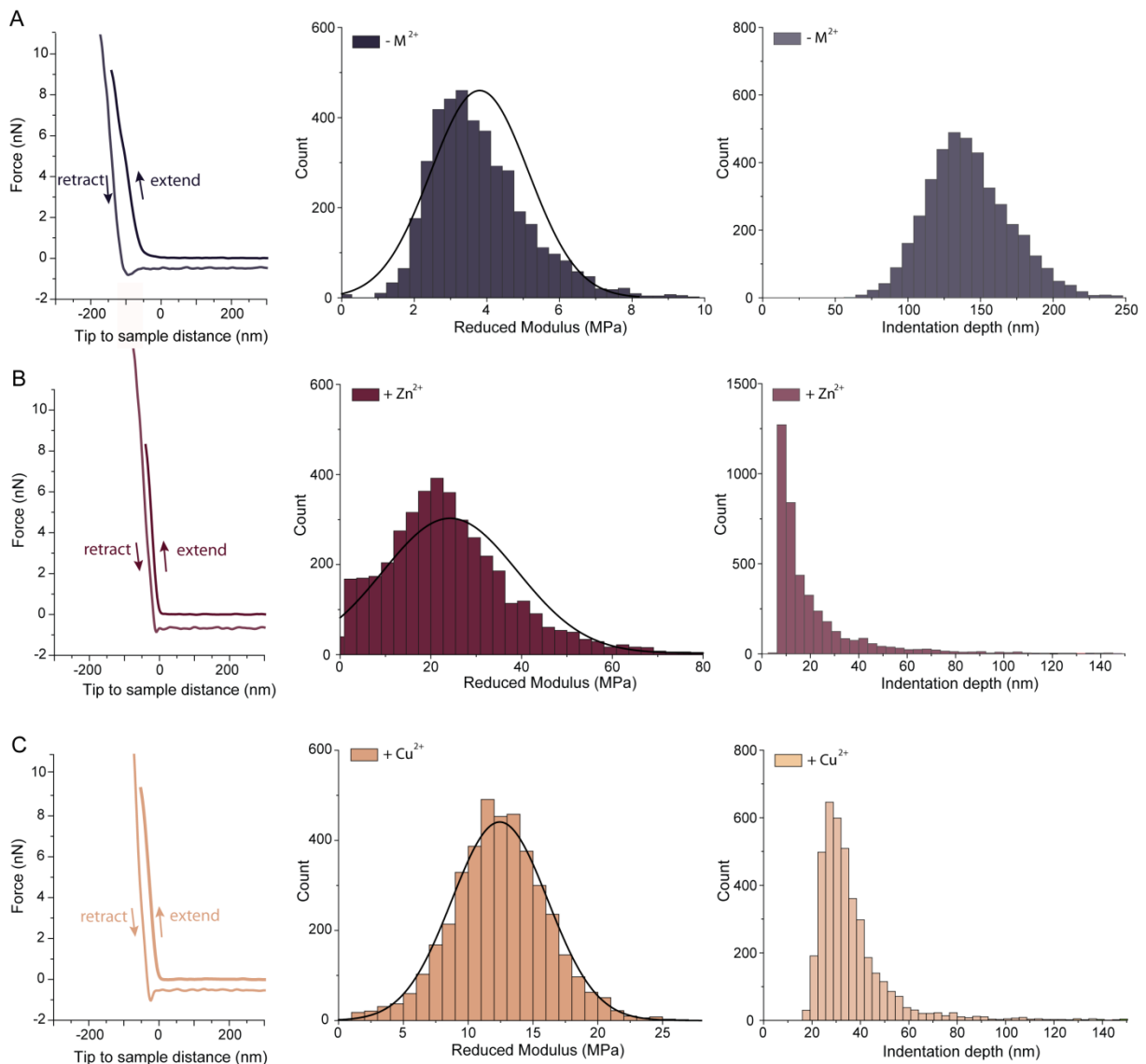


Figure 14. Metal-binding affects the mechanical properties of HRD-based peptide films.

(A) Peptide films that were formed in the absence of metal ions show less steep force–displacement curves when compared to films that contain  $Zn^{2+}$  (B) or  $Cu^{2+}$  (C). Resulting extracted moduli show a 10-fold increased stiffness of peptide films that were formed in the presence of  $Zn^{2+}$  (B) compared to films without metal ions (A) while the stiffness of films containing  $Cu^{2+}$  is only slightly increased (C). The calculated indentation depth of all three samples does not exceed 10 % of the sample thickness.

In the absence of metal ions (Figure 14 A), the curves appear less steep than those of peptide films containing metal ions (Figure 14 B, C). The reduced moduli were calculated from the elastic response of the samples indented by the AFM tip using the Hertz model for data fitting. The resulting moduli show a 10-fold increased stiffness of peptide films that were formed in the presence of  $Zn^{2+}$  (Figure 14 B) compared to films without metal ions (Figure 14 A), while the stiffness of films containing  $Cu^{2+}$  is only slightly increased (Figure 14 C). Due to the high complexity of the system, the resulting values are considered as comparative; however, they clearly indicate a large effect of metal



binding on mechanical properties. In order to exclude any influence of the glass substrate on the calculations, the indentations must not exceed 10 % of the sample thickness. Under wet conditions, samples were  $\sim 50 \mu\text{m}$  thick, whereas the indentation depths did not account for more than 250 nm (Figure 14). Taken together, the results of the mechanical testing strongly indicate an influence of metal ions on the stiffness of HRD-based peptide films likely arising from their metal-dependent architecture. The mechanical characterization of HRD-based peptide films was enabled by adding glycerol as a plasticizer. An alternative strategy to overcome the high brittleness could be to include peptides based on the flanking domains of preCol proteins. These domains are known to complement the sacrificial network of HRD by providing high extensibility of byssal threads via hidden length.<sup>24</sup>

### 4.3 Discussion

By linking the existing knowledge of mussel byssus fabrication to bottom-up assembly of a bioinspired polymer, I developed a protocol for the self-assembly of HRD-based peptides into free-standing films. The present results reveal that HRD-based peptides spontaneously assemble into hierarchically organized amyloid-like  $\beta$ -sheet structures within free-standing films. The findings are consistent with previous results that report dense amyloid-like phases of HRD peptides under conditions relevant for thread formation, namely, basic pH and high concentration.<sup>83</sup> They once more support the hypothesis that HRDs may exist in an ordered conformation in the mussel byssus; however, the actual secondary structure of HRDs within preCol proteins still needs to be resolved *in situ*. Based on combined investigations with X-ray diffraction and spectroscopy, I suggest a model that is presented in Figure 15. Because the peptide contains an alternating  $[\text{HA}]_n$  sequence at the N-terminus, we can assume that all histidine residues in the  $\beta$ -strand configuration are facing in one direction, and alanine residues are facing in the opposite direction (Figure 15 A). Along the plane of the film,  $\beta$ -sheets do not show any preferred orientation (Figure 15 B). However, results of polarized Raman spectroscopy and XRD reveal that  $\beta$ -sheets are most likely stacked in the y-direction, leading to an organized structure at multiple length scales (Figure 15 C). FTIR spectroscopy revealed that peptide films formed in the absence of metal ions are the most crystalline at the level of  $\beta$ -sheet H-bonding. The different measured stacking distances might arise depending on which residues are facing each other. Theoretically, either His–His, Ala–Ala, or His–Ala interfaces are conceivable. Considering that all presented results suggest that films containing  $\text{Zn}^{2+}$  show the highest hierarchical order, we hypothesize that binding Zn ions via histidine residues brings layered  $\beta$ -sheets into register at the expense of crystallinity. One feasible way might be through lateral bridging interactions that

are present in metal-containing films according to the results of Raman spectroscopy (peak at  $1555\text{ cm}^{-1}$ ) (Figure 8 C). In light of the spectroscopic evidence, metal ions might be coordinated between histidine residues of two  $\beta$ -sheets putatively in a tetrahedral geometry. In addition, results of polarized Raman spectroscopy suggest that the C4=C5 bond in the imidazole side chains is oriented perpendicular to the film plane. However, the combined investigations indicate that the addition of Cu results in less hierarchically organized peptide films.

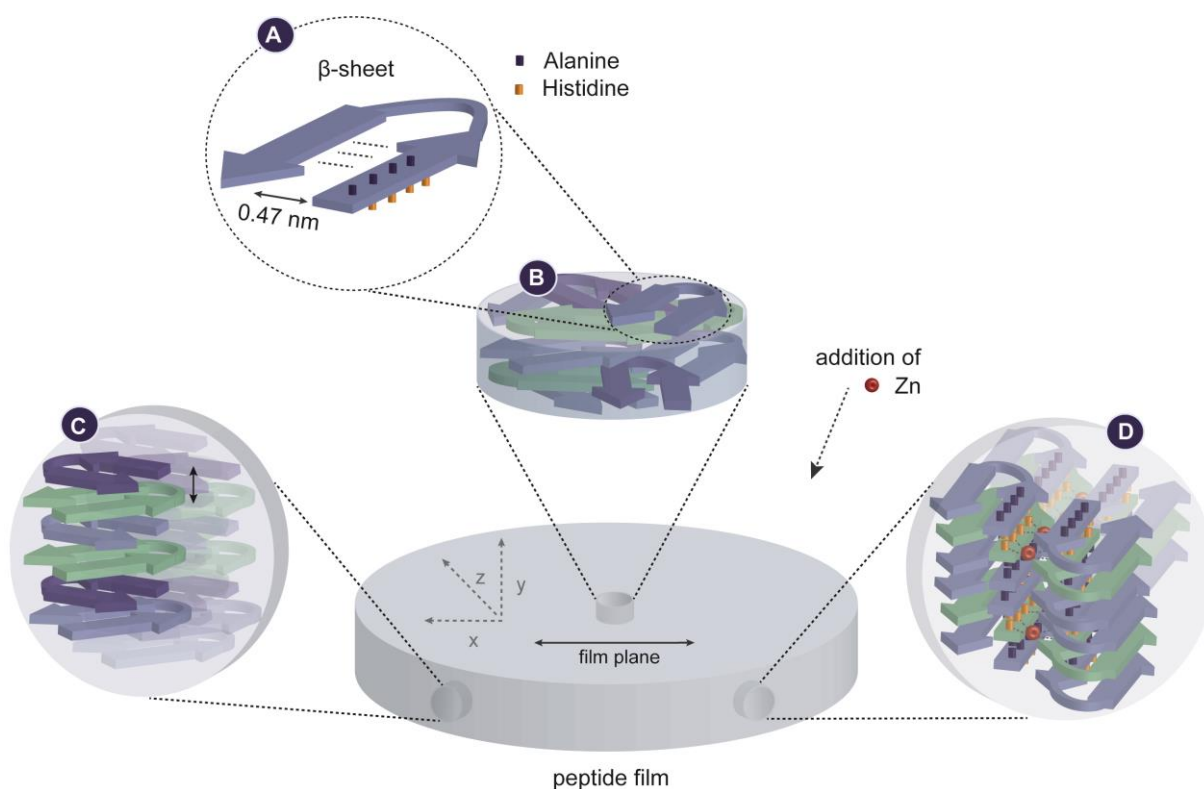


Figure 15. Model of multiscale structure in HRD-based peptide films.

(A) HRD-based peptides form amyloid  $\beta$ -sheet structures with histidine residues facing in one and alanine residues facing in another direction. (B) Along the plane of the film,  $\beta$ -sheets do not show any preferred orientation. (C)  $\beta$ -Sheets are most likely stacked in the y-direction, leading to an organized structure at multiple length scales. (D) Zn ions might bring  $\beta$ -sheets into register presumably via lateral bridging interactions.

The results of FTIR spectroscopy revealed that the peak ( $1626\text{ cm}^{-1}$ ) indicating crystalline  $\beta$ -sheet structure is less prominent for films containing Cu. Furthermore, the peaks in the obtained polarized Raman spectra show less explicit differences in intensities when measured at  $0$  and  $90^\circ$  polarization, which indicates a less oriented structure compared to films containing no metal ions or Zn. In addition, the obtained SAXD pattern suggests an inhomogeneity higher than that of the other samples. One explanation for a less organized structure might be a different coordination geometry that reduces the lateral arrangement of  $\beta$ -sheets.<sup>127</sup> XAS measurements of films containing Cu could help to shed some light on this open question.



#### 4.4 Conclusion

The combined studies demonstrate that HRD-based peptide films containing Zn ions possess both a higher degree of hierarchical order and significantly higher mechanical performance, suggesting a possible correlation between these two parameters. Future work will aim at further disentangling the complex interplay of structure and performance. Overall, these studies strengthen the hypothesis that HRDs of mussel byssus proteins self-assemble in a pH-triggered manner, which allows the transition from a liquid-crystalline phase to a stiff fiber with highly defined structural organization. Moreover, the presented results demonstrate that this approach enables one to specifically tune both the higher order structure and the mechanical properties of the films depending on the processing and inclusion of metal ions. This work establishes mussel HRD peptides as versatile natural building blocks for fabricating biomaterials and demonstrates a pathway for the production of complex nanostructured materials.

## 5. ULTRASTRUCTURE AND COMPOSITION OF BYSSAL THREAD CUTICLE

The design and production of thin coatings that are able to protect flexible substrates is appealing for a variety of technological applications but remains challenging, since conventional coatings are usually either hard or extensible.<sup>72</sup> The byssal thread cuticle on the other hand, resembles a particle-reinforced composite and combines both properties, which is believed to allow efficient protection of the extensible fibrous core from abrasion.<sup>25</sup> Current mussel-inspired coatings and polymers are mainly based on the identified key player of cuticle mechanical performance – DOPA residues.<sup>16</sup> However, these materials lack the complex structure of the native biological material and show inferior mechanical performance. A key first step to improve upon current mussel inspired materials is a thorough understanding of the native byssal thread cuticle ultrastructure, composition and its influence on mechanics.

The byssus cuticle resembles a particle-reinforced composite with biphasic granules that are embedded in a matrix and this hierarchical structure was proposed to play a vital role in cuticle mechanics.<sup>66</sup> However, the current hypotheses regarding their explicit function are highly contrary. Based on the observation that granules seem to arrest crack formation in the matrix under high strain, it was assumed that they endow the cuticle with enhanced damage tolerance.<sup>42</sup> *In situ* resonance Raman spectroscopy demonstrated a higher density of DOPA-metal cross-links in the granules than in the matrix, provoking the hypothesis that granules provide the cuticle with hardness, whereas the matrix provides extensibility.<sup>25</sup> However, a more recent study demonstrated that granules seem to be three-fold softer in the semi-hydrated state suggesting a model, in which granules are responsible for keeping the cuticle plasticized via hydration, preventing it from becoming brittle during emersion in intertidal zones.<sup>70</sup> Although the exact role of granules in cuticle mechanics remains elusive, it is known that DOPA-metal coordination cross-links in the cuticle are a critical component of its mechanical behavior.<sup>25,42,72,74</sup> Ca, Al and Si were previously detected in the cuticle of *M. galloprovincialis* and combined Raman spectroscopy and electron paramagnetic resonance (EPR) measurements demonstrated the presence of DOPA-Fe and DOPA-V tris-coordination bonds.<sup>69,74</sup> As of yet, a specific distribution of the concurrently present metal ions in native byssal cuticles was not ascertained. EDTA-treatment of native threads resulted in significant reduction of elastic modulus and hardness, which both could be recovered by subsequent metal reinforcement.<sup>74</sup> Notably, mussels were demonstrated to be opportunistic in their use of metal ions, since Fe and V were both equally sufficient to recover the cuticles native mechanical behavior.<sup>74</sup>



Thus, the key to understanding this material requires a deeper look into the structure-function relationship and composition.

It is currently assumed, that granules and matrix are both composed of DOPA-rich mfp-1, which brings into question the origin of the biphasic granules, which based on appearance, are likely comprised of more than one component. Indeed, it seems very likely that other macromolecules contribute to the observed phase-separated structure. Along these lines, fatty acids were proposed to function as an anionic counterpart and were recently localized on the surface and inside of byssal threads and plaque, but their role in determining cuticle structure or properties is not clear.<sup>68,71</sup> Notably, recombinant mfp-1 was shown to undergo liquid-liquid phase-separation *in vitro* - even in the absence of negatively charged counterparts.<sup>80</sup> The coacervation of mfp-1 was shown to be triggered via cation- $\pi$  interaction at sea-level salt concentration, which was identified as key factor for this process by regulating the effective interaction of mfp-1.<sup>80</sup> Another study demonstrated that coacervation of recombinant mfp-1 with a second positively charged polyelectrolyte.<sup>102</sup> The formation of this like-charged coacervate was also triggered by short-range cation- $\pi$  interactions, which help to overcome longer-range electrostatic repulsion. Based on these results, the presence of other proteins and their interaction with mfp-1 may offer an explanation for the observed phase-separated granule structures. Along these lines, a recently published study discovered four additional cysteine-rich proteins based on transcriptomic analysis of the mussel foot cuticle gland, but their presence in the cuticle was not experimentally verified thus far.<sup>53</sup> The lacking evidence of other components in the thread cuticle impede the development of a coherent model, which explains its complex ultrastructure.

In an effort to shed light on the above presented open questions, I undertake a detailed *in situ* investigation of *M. edulis* byssal thread cuticle. By combining high-resolution electron microscopy with elemental analysis, I demonstrate the presence of another sulfur-rich proteinaceous component in the thread cuticle, likely indicating high cysteine content. Moreover, the obtained results strongly indicate a specific distribution and partitioning of different metal ions in the byssus cuticle, which might have important implications on the design of future mussel-inspired coatings. Finally, the 3D-reconstruction of cuticle granules provides fundamental insights into its ultrastructure to a degree that has not been previously observed.

## 5.1 Material & Methods

### 5.1.1 Chemical fixation & embedding

Native threads were collected from mussels grown in the North Sea and stored at 4 °C in tap water until usage. Threads were washed 3 x 5 min in cold double distilled H<sub>2</sub>O and the distal part was cut into small pieces of ~ 3 mm in length. Fixation was carried out for 1 h at 4 °C in 2.5 % glutaraldehyde and 1.5 % paraformaldehyde in 0.1 M cacodylate buffer pH 7.4. Samples were rinsed 3 x 10 min in 0.1 M cacodylate buffer at 4 °C before post-fixation with 1 % osmium tetroxide for 1 h. Samples for EDS measurements were treated as previously described without osmium staining. A second rinsing step in 0.1 M cacodylate buffer pH 7.4 (3 x 5 min at 4 °C) was followed by dehydration in ethanol (50 %, 70 %, 90 %, 3 x 100 %) for 10 min each step at RT. Threads were embedded in low viscosity Spurr's resin (Electron Microscopy Sciences, # 14300) at 65 °C over two days.

### 5.1.2 TEM-EDS

The resulting resin blocks were trimmed to the region of interest and sectioned to 100 nm using an ultramicrotome (PowerTome Model XL). Ultrathin sections were mounted on lacey carbon coated copper grids (200 mesh) for imaging and EDS measurements. Dark-field electron imaging using a HAADF detector and EDS was performed on a Jeol JEM ARM200F equipped with a cold field-emission electron source (operated at 200 kV) and an emission current of 15 µA. Elemental maps (59 x 89 pixel) were acquired at a magnification of 200 000 x with a pixel size of 9.3 x 9.3 nm and an exposure of 1 sec per pixel using an Silicon Drift Detector (SDD).

### 5.1.3 FIB - SEM

Resin blocks containing the chemically fixed samples were polished in order to expose the thread on the block surface. The sample was sputter coated with three Carbon layers (~ 5 nm per layer) and one platinum layer (120 sec) and transferred to the Zeiss Crossbeam 540 (Carl Zeiss Microscopy GmbH, Germany). At the region of interest, a trench for SEM imaging was milled into the sample surface using the 65 nA FIB current at 30 kV acceleration voltage. The resulting cross-section was finely polished using the 1.5 nA FIB probe at 30 kV. Thin slices of material were removed in a serial manner by FIB milling (700 pA, 30 kV) and after each milling step (slice thickness 10.5 nm), the specimen was imaged by SEM at 2.5 kV acceleration voltage using the in-lens secondary electron detector. The image resolution was 1024 x 786 pixels with a lateral image pixel size of 4.8 nm. Images were recorded using line averaging (N = 31) and a dwell time of 200 ns.



#### 5.1.4 Image processing

The resulting secondary electron images were processed using the SPYDER<sup>3</sup> (Scientific Python Development Environment) (Python 3.6) software. Custom-written python scripts were developed and provided by Luca Bertinetti (Max Planck Institute of Colloid and Interfaces, Golm, Germany). Images were automatically aligned using the Fourier shift theorem for detecting the translational shift in the frequency domain and vertical stripes arising from the water fall effect by FIB milling were removed by Fourier filtering. Total variation denoising was performed by applying the Chambolle algorithm in 3D mode. The images were inverted afterwards with Fiji and Sauvola's local thresholding computation was applied with a block size of 11, a k value of 0.005 and r value of 1.7. As the thresholded images contained regions resulting from statistical noise in the image, only thresholded regions containing minimum 40 pixels were selected. Images were median 3D filtered with Fiji and x, y, z radii were set to 1.5.

#### 5.1.5 Segmentation

Segmentation of five adjoining cuticle granules was performed using the ZIB version of Amira 3D (Thermo Fisher Scientific, USA). Granule shapes were segmented manually from 352 processed and inverted secondary electron images using the brush tool. In a second step, the dark granule phase was segmented automatically from local threshold computed and median3D filtered image stacks using the Magic Wand tool. 3D visualization of the dark phase was realized by generating a surface from segmented structures. For a better depiction of the granule structure, the surface was cropped and rotated.

#### 5.1.6 Volume fractions and 3D thickness mapping

The volumes of the electron-light (el) and electron-dense (ed) granule phases were calculated using the "Measure and Analyze" tool in Amira. The volume fractions for each individual granule were calculated as follows:

$$V_{\text{total}} = V_{\text{el}} + V_{\text{ed}} \quad \phi_{\text{el}} = V_{\text{el}} / V_{\text{total}} \quad \text{and} \quad \phi_{\text{ed}} = 1 - \phi_{\text{el}}$$

The mean values and standard deviation were calculated with OriginPro 2015. The thickness of the electron-dense phase was mapped using the Exact Euclidean Distance Transform (3D) plugin of Fiji. A default threshold of 7.5 nm was set with Fiji and the original and thresholded data were 3D-reconstructed with Amira 3D (Thermo Fisher Scientific, USA).

## 5.2 Results

### 5.2.1 Ultrastructure of *M. edulis* byssal thread cuticle

The byssal thread cuticle was subject of numerous studies during the past decade due to its outstanding mechanical properties (high hardness and extensibility). Most of the studies investigated the cuticles of *M. galloprovincialis* and *M. californianus* threads, which exhibit thicknesses of 2 – 5  $\mu\text{m}$ .<sup>66,68,72</sup> The cuticle of both species contains numerous biphasic granules, which are embedded in an amorphous matrix. The granule size ( $\sim 200$  nm) in *M. californianus* cuticles is only a quarter of those in *M. galloprovincialis* and was associated with superior mechanical properties.<sup>66</sup> However, the exact structure-function relationship remains elusive to date and the existing hypotheses are contrary.<sup>25,70</sup> The cuticle of *M. edulis* byssal threads, here viewed by environmental scanning electron microscopy (ESEM) (Figure 16 A), is a thin, bumpy layer that surrounds the thread core. Similar to the cuticles of its related species, the transverse cross-section of embedded *M. edulis* thread cuticle exhibits biphasic granules ( $\sim 500$  – 800 nm), which are embedded in a matrix (Figure 16 B). In contrast to the well characterized cuticles of *M. galloprovincialis* and *M. californianus* threads, the amorphous matrix appears to be very thin (100 – 500 nm) and barely covers the granules. Furthermore, granules are mostly located next to each other in a single layer, whereas they also appear to be stacked in multiple layers in the other two species (Figure 16 B).

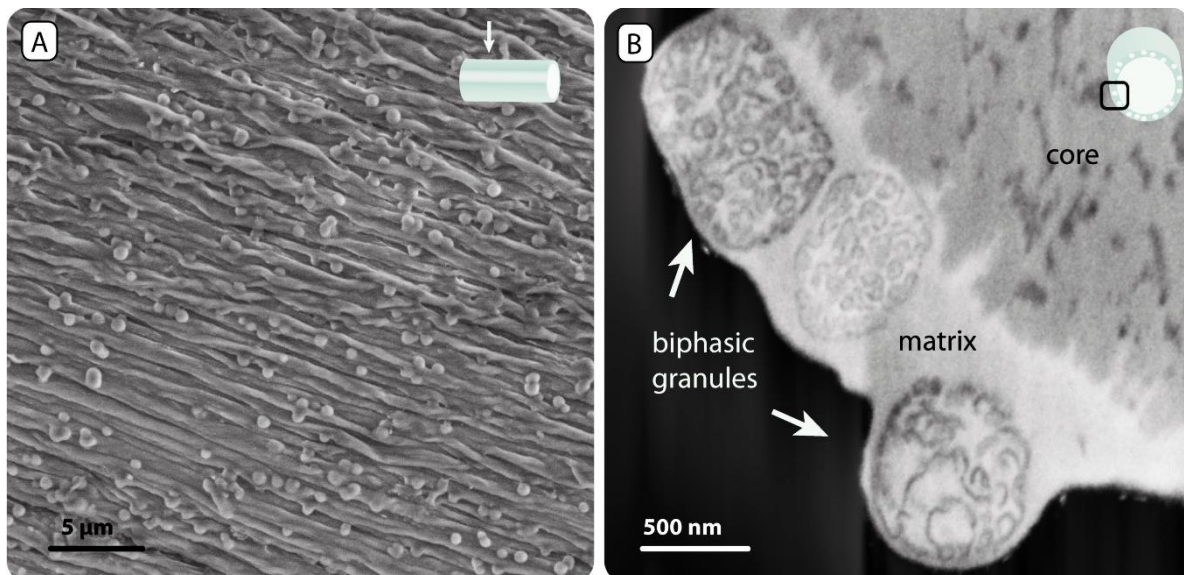


Figure 16. The cuticle of *M. edulis* byssal threads contains biphasic granules.

A) ESEM image of *M. edulis* cuticle shows a thin, bumpy layer. B) FIB-SEM image of a transverse cross-section of an osmium-stained, embedded thread showing that the cuticle consists of biphasic granules embedded in an amorphous matrix.



The electron-dense phase of the biphasic granules is convoluted and winding resembling a brain-like morphology, whereas the other less electron dense phase seems to be of similar texture and possibly continuous with the surrounding matrix. Currently, mfp-1 is the only known protein in byssus cuticle, but the presence and contribution of other components to the complex ultrastructure seems very likely. In order to obtain information of other possible macromolecules in the cuticle, its elemental composition was analyzed.

### 5.2.2 Elemental composition of byssal thread cuticle

The byssus cuticle is known as a paragon for bio-inspired engineering coatings, since it combines high hardness and extensibility. However, as of yet, the development of a mussel-inspired coating with native-like properties was not achieved - most likely because the cuticle ultrastructure, composition and assembly process are not well understood. Especially the origin of biphasic granules and their role in cuticle mechanics are of interest in order to improve upon current generation of bio-inspired materials. The extraction of other cuticle building blocks was reported to be insufficient due to the physical and chemical inertness of threads.<sup>68,91</sup> Therefore, high resolution elemental analysis was considered as a promising approach for the detection of previously unidentified cuticle components. However, the compositional investigation of cuticle granules and matrix is accompanied by vast technical challenges. Metal ions, which are known as crucial cuticle components, have been reported to merely account for 1 % of byssus dry weight, making them highly difficult to detect.<sup>42,72,74</sup> Furthermore, the domain size of granules is between 20 and 40 nm, which requires a high spatial resolution for elemental analysis.<sup>42</sup>

Therefore, high-resolution TEM combined with EDS was performed on unstained ultrathin transverse sections of distal threads. The combination of high resolution images and resulting elemental maps provides us with crucial information about the composition of matrix and granules. Imaging was performed in scanning transmission electron microscopy (STEM) mode using a high-angle annular dark field detector (HAADF) and the corresponding elemental maps were acquired with an EDS detector. A representative result of the elemental analysis is presented in Figure 17. Since the sample is embedded, the elemental analysis likely includes carbon and oxygen from the resin, which results in an underestimation of other elements. The resulting percent composition maps are therefore considered as comparative without exact quantitative determination of elements. The STEM image shows a biphasic granule embedded in matrix (Figure 17 A). The resulting percent composition maps show a high nitrogen and constant carbon signal in both matrix and granules, as well as the thread core, suggesting that all structures consist predominantly of proteins (Figure 17 B, C).

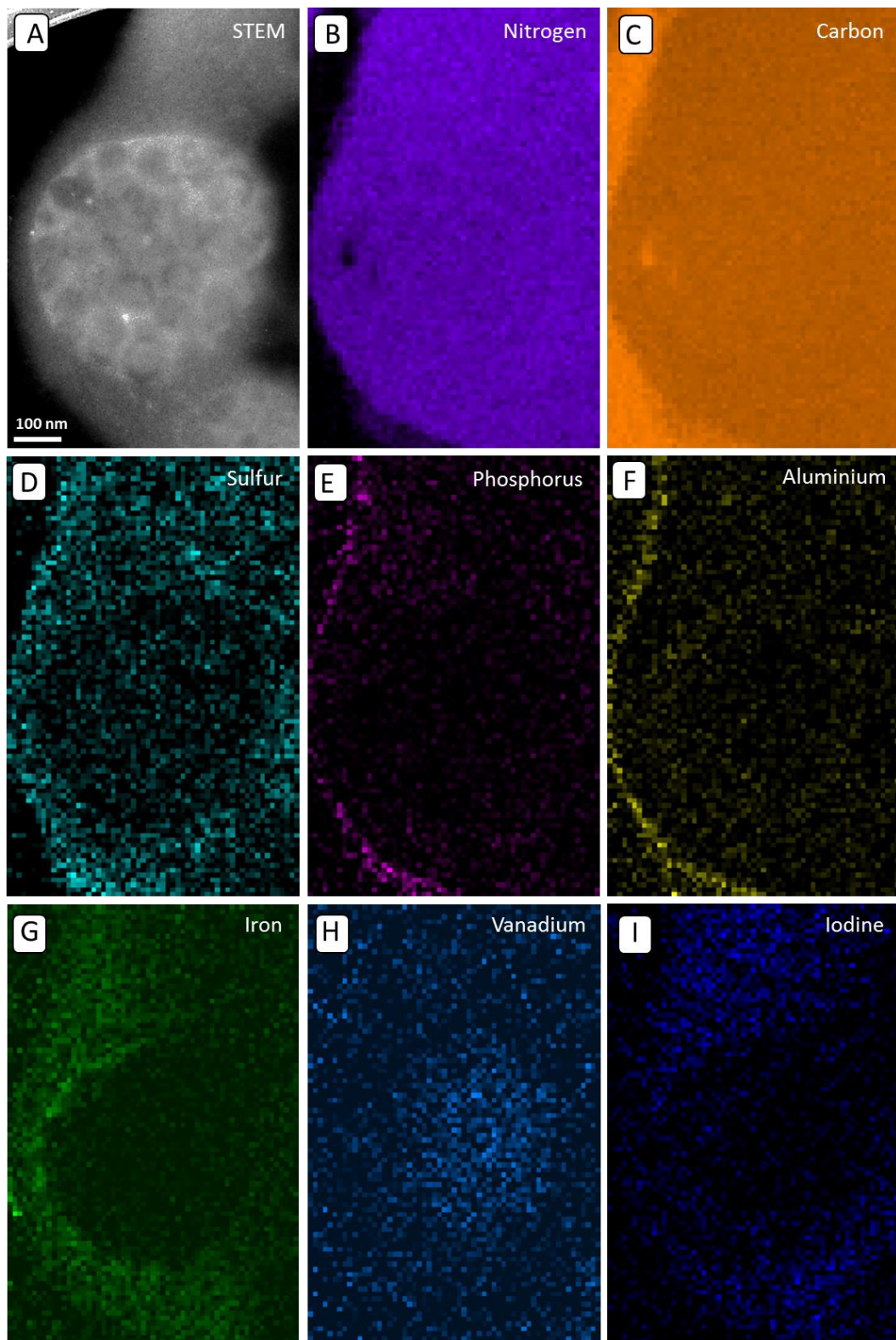


Figure 17. Sulfur and metal ions show distinct distributions in the thread cuticle.

A) STEM HAADF image of a biphasic granule embedded in matrix. B) - H) EDS elemental maps. B) and C) Granules and matrix exhibit a high nitrogen and constant carbon signal suggesting the presence of proteins in both phases. D) Sulfur seems to be more concentrated in the matrix than in the biphasic granules. E) and F) P and Al are accumulated at the cuticle surface. G), H), I) A higher content of Fe and I can be found in the matrix, whereas V seems to be more concentrated in the granule.



This result is consistent with previous models that proposed mfp-1 as main building block of both structures and seems to reject a previous hypothesis of an enhanced lipid component in the cuticle, since the nitrogen content is consistent also between cuticle and core (Figure 17 B). However, the elemental analysis revealed that cuticle matrix and granules contain sulfur (Figure 17 D). It should be noted, however, that the sulfur content in the matrix is approximately two-fold higher than in the granules. In light of the constant nitrogen signal, which indicates the presence of proteins, sulfur likely stems from cysteine residues in protein components. Notably, mfp-1 does not contain cysteine, suggesting the presence of another proteinaceous cuticle component enriched in sulfur-containing amino acids. This fits well with previous hypotheses proposing the presence of cysteine-rich proteins in the cuticle based on transcriptomic data.<sup>53</sup> In addition, while the overall content of sulfur is lower in the granules than matrix, there may be regions of enriched sulfur in the granules (Figure 17 D). Furthermore, P and Al are both present in matrix and granules and seem to be concentrated at the cuticle surface (Figure 17 E, F). Most notably with respect to previous functional studies of the cuticle, the results presented here provide evidence for a distinct distribution of metal ions in the byssus cuticle. It was previously shown that the cuticle contains metal enrichment by both Fe and V, both of which were proposed to interact with DOPA.<sup>25,74</sup> Whereas Fe seems to be more concentrated in the matrix, where I is also co-localized, the percent composition of V is elevated inside the granules (Figure 17 G, H, I). Moreover, the Fe signal shows a sharp decrease transitioning from the matrix to the granule (Figure 17 G).

The data presented here provide the first indication of proteins other than mfp-1 being present in the byssus cuticle. In addition, these results suggest a segregation of specific metal ions between matrix and granules. The current work adds another level of complexity to the ultrastructure and composition of byssus cuticle. Information about the three-dimensional architecture of granules could provide us with crucial information about the biphasic system and will be helpful to interpret the current results. Therefore, the distal thread cuticle was examined with FIB-SEM and image stacks allowing the 3D-reconstruction of granules were obtained.

### 5.2.3 3D-reconstruction of cuticle granules

Considering the complexity of this natural coating, 3D-reconstruction of the granules aims for a better understanding of its hierarchical structure and allows comparison with other known natural and synthetic polymeric nano-architectures. However, granules of *M. edulis* exhibit sizes between 500 nm and 800 nm (chapter 5.2.1) and the electron-dense phase was previously reported to have a domain size of 20 – 40 nm.<sup>42</sup> Consequently, reconstruction of the individual features requires a high spatial resolution. FIB-SEM emerged as powerful tool for the three-dimensional investigation of

nanoscale biological architectures.<sup>92,128</sup> The focused ion beam precisely and progressively removes layers of sample material, thus, creating each time a surface that can be scanned and imaged with an electron beam with very high spatial resolution.<sup>92</sup> Thus, this high-end technology is excellently suited to investigate the hierarchical architecture of *M. edulis* cuticle granules. However, applying this method firstly required the development of a fixation, staining and embedding protocol, which preserved all structural details and provided a good contrast of nanoscale features. The resulting sample was fine-polished to expose the thread on the sample surface and a trench was milled with the FIB in the region of interest (Figure 18). The resulting surface was scanned with a pixel size of 4.8 nm and an image was taken every 10.5 nm resulting in an image stack (352 images) suitable for a detailed reconstruction of several granules in three dimensions (Figure 18).

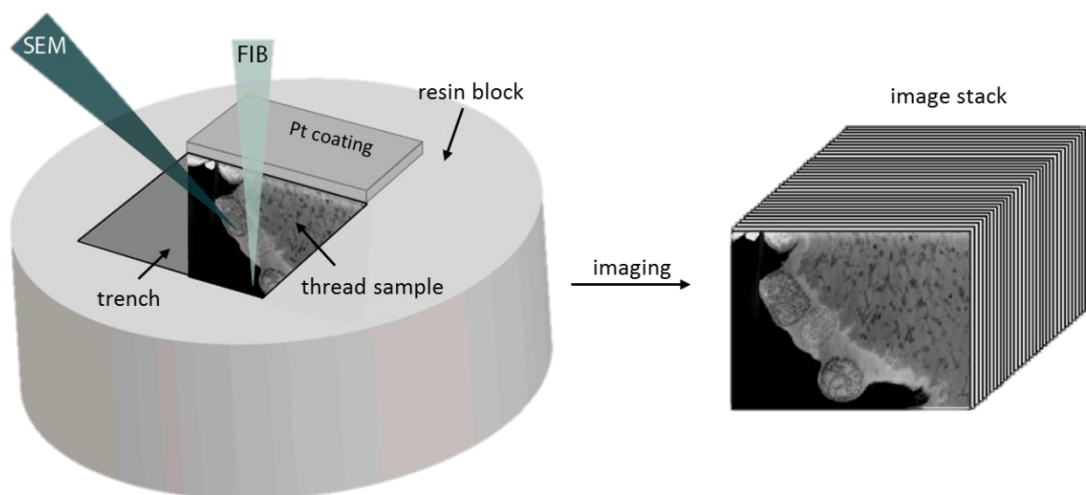


Figure 18. FIB-SEM setup for imaging the cuticle of *M. edulis* threads in three dimensions.

A transverse cross-section of the cuticle is exposed by milling a trench with the FIB. The FIB progressively removes sample material, whereas the electron beam scans each resulting surface in a serial manner resulting in an image stack suitable for 3D-reconstruction.

Processing of the resulting secondary electron images is a crucial step before the nanoscale structures can be reconstructed, since the images are noisy and contain vertical stripes stemming from the water fall effect by FIB-milling (Figure 19 A). Custom-written python scripts provided by Luca Bertinetti (Max Planck Institute of Colloids and Interfaces, Golm) were used to align, destripe and denoise the original images (Figure 19 A) by carefully selecting appropriate parameters. The processed images were then inverted (Figure 19 B) in preparation for the local threshold computation (Figure 19 C) that was highly suited for the segmentation of the electron-dense phase (here depicted in white).

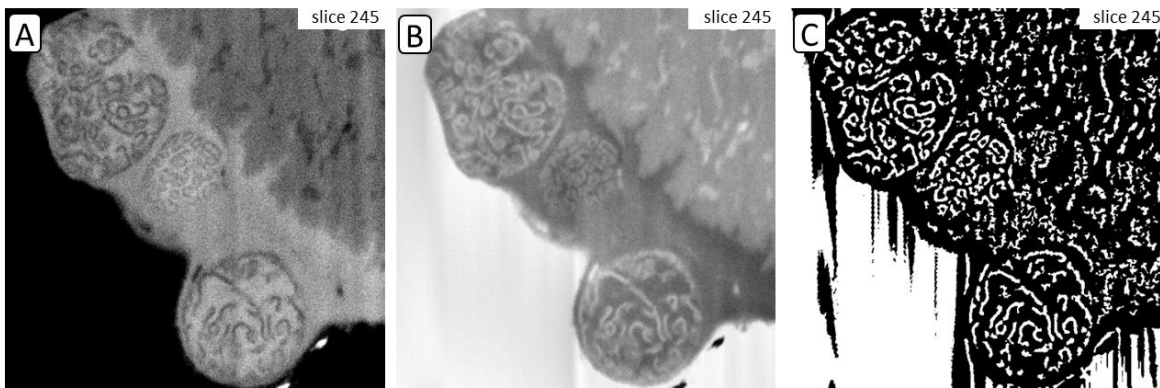


Figure 19. Image processing by using custom-written python scripts.

A) Original images contain noise and vertical stripes stemming from the water fall effect of FIB milling. B) Images were aligned, destriped, denoised and inverted for better contrast. (C) Local threshold computed image stacks were suitable for 3D-reconstruction of the electron-dense phase (here depicted in white).

The granule shape and internal electron-dense granule phases were segmented using the Amira 3D software, which assigns each pixel of an image to a created label. Theoretically, segmentation can be realized automatically based on the different gray values of an image data set, which usually correspond to different structures. However, both matrix and granules contained pixels with similar grey values and thus, segmentation of granules and electron-dense phase had to be performed manually. Firstly, the granule shape of five different granules was defined by going through 352 single images (Figure 19 B) and the pixels of each granule were assigned to five labels. Within the created granule labels, the electron-dense phase could be automatically segmented by using the corresponding binary local threshold computed images (Figure 19 C). Surfaces of the electron-dense phases were generated from the segmented data and present a detailed depiction of their complex ultrastructure (Figure 20).

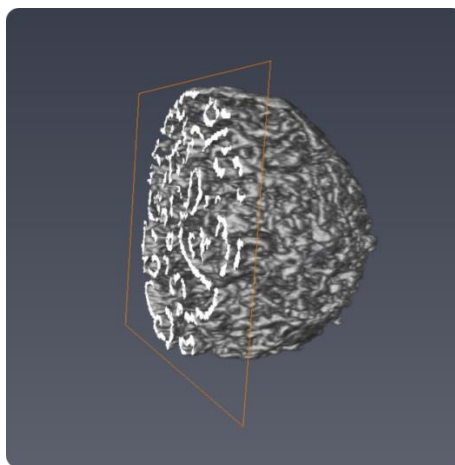


Figure 20. Architecture of biphasic cuticle granules.

3D-reconstruction of a sliced electron-dense granule phase in xy direction reveals the complex architecture of cuticle granules.

The data presented here illustrate for the first time, that the electron-dense granule phase forms a highly complex interconnected system. Figure 21 A shows five adjoining granules sliced in xy direction, as well as reconstructed tubular features in the thread core (marked with an arrow), which indicate the fiber direction. Notably, slicing the surfaces in yz direction revealed that the interconnected sheets, formed by the electron-dense phases of all adjoining granules, seem to be aligned approximately 45 ° relative to the fiber main axis (Figure 21 B).

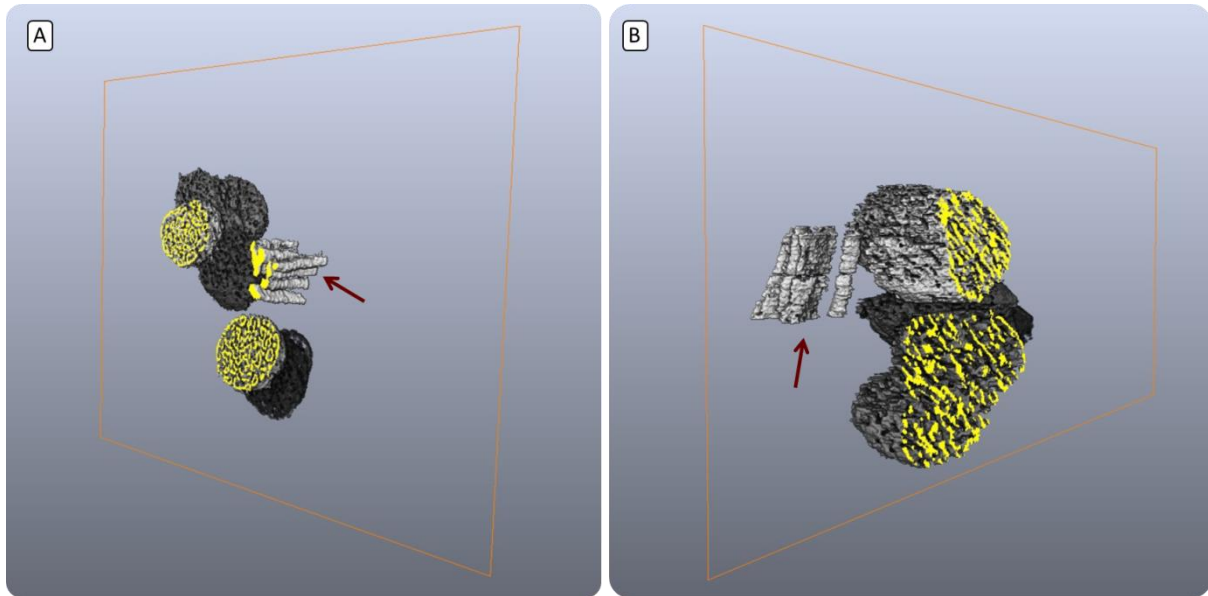


Figure 21. Orientation of the electron-dense granule phase.

A) Five adjoining granules and reconstructed tubular features in the thread core (marked with an arrow) indicating the fiber orientation, are sliced in xy direction. B) Slicing the electron-dense phase of adjoining granules in yz direction reveals that the interconnected sheets are aligned in one direction.

For a better understanding of the details, a segmented granule phase was cropped and rotated. The resulting image series is presented in Figure 22.

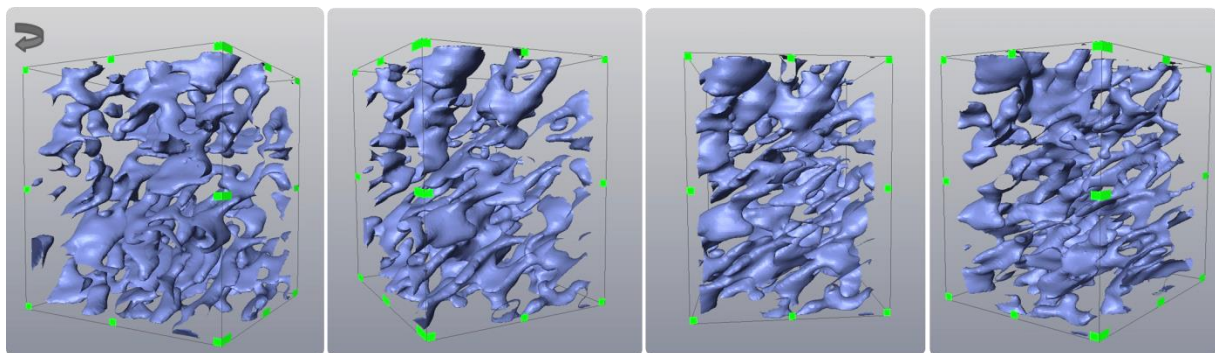


Figure 22. Alignment of the electron-dense granule phase.

Clockwise rotation of a cropped electron-dense granule phase reveals the alignment of structures.



The reduced perspective on the granule phase reveals that it consists of planar structures, which are connected via elongated structures. These data suggest that the 3D-architecture is a highly defined system, which was highly unexpected based on previous analysis of TEM and AFM images of granular biphasic structures.<sup>42,66,73</sup> Based on the 3D-reconstruction of the segmented phases within the granule, the volume fractions of the electron-dense and the surrounding bright phase could be calculated and the mean values are presented in Figure 23.

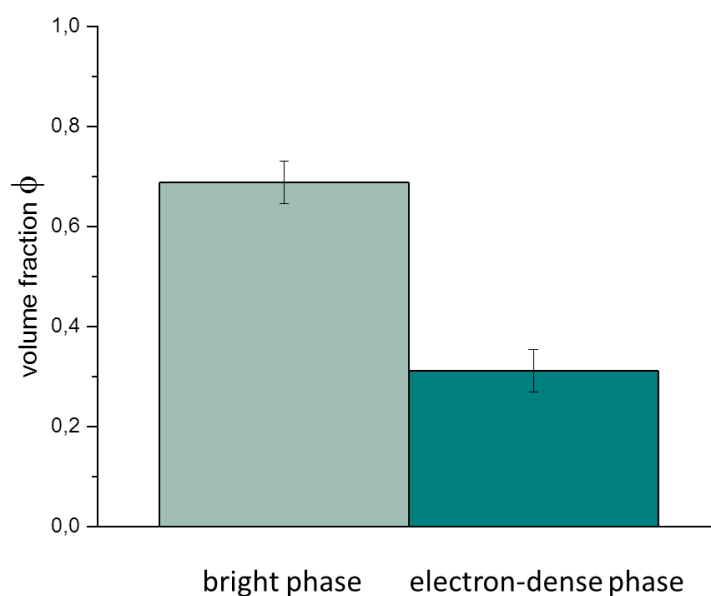


Figure 23. Mean volume fraction  $\phi$  of cuticle granules. Calculated volume fractions of five granules reveal that granules possess highly defined internal architectures.

Calculated volume fractions of both phases reveal that the volume of the electron-light phase surrounding the electron-dense phase of the granule is approximately twice as high. Furthermore, all five granules exhibited very similar volume fraction suggesting that their formation is a highly controlled process. In order to estimate the thickness of the electron-dense phase, an Exact Euclidean Distance Transform of binary granule phase images (Figure 24 A) was performed in 3D mode. Figure 24 B shows a representative thickness map, in which the brightest pixels correspond to a distance of approximately 11 nm from the border of the phase to its core. A threshold was set to 7.5 nm and the resulting binary image (Figure 24 C) shows that the scaffold of the thresholded electron-dense phase matches the appearance of the original structure (Figure 24 A). 3D-reconstruction of the original (Figure 24 D) and thresholded data (Figure 24 E) confirm their similarity. These results suggest, that the thickness of the electron-dense phase is very consistent (at least  $\sim 15$  nm), whereas the spacing between the planar sheets varies. As of yet, the byssus cuticle posed numerous unresolved research questions regarding its ultrastructure and composition. These

new results allow for the first time a detailed depiction of byssus cuticle granules, which broaden our understanding of this complex coating.

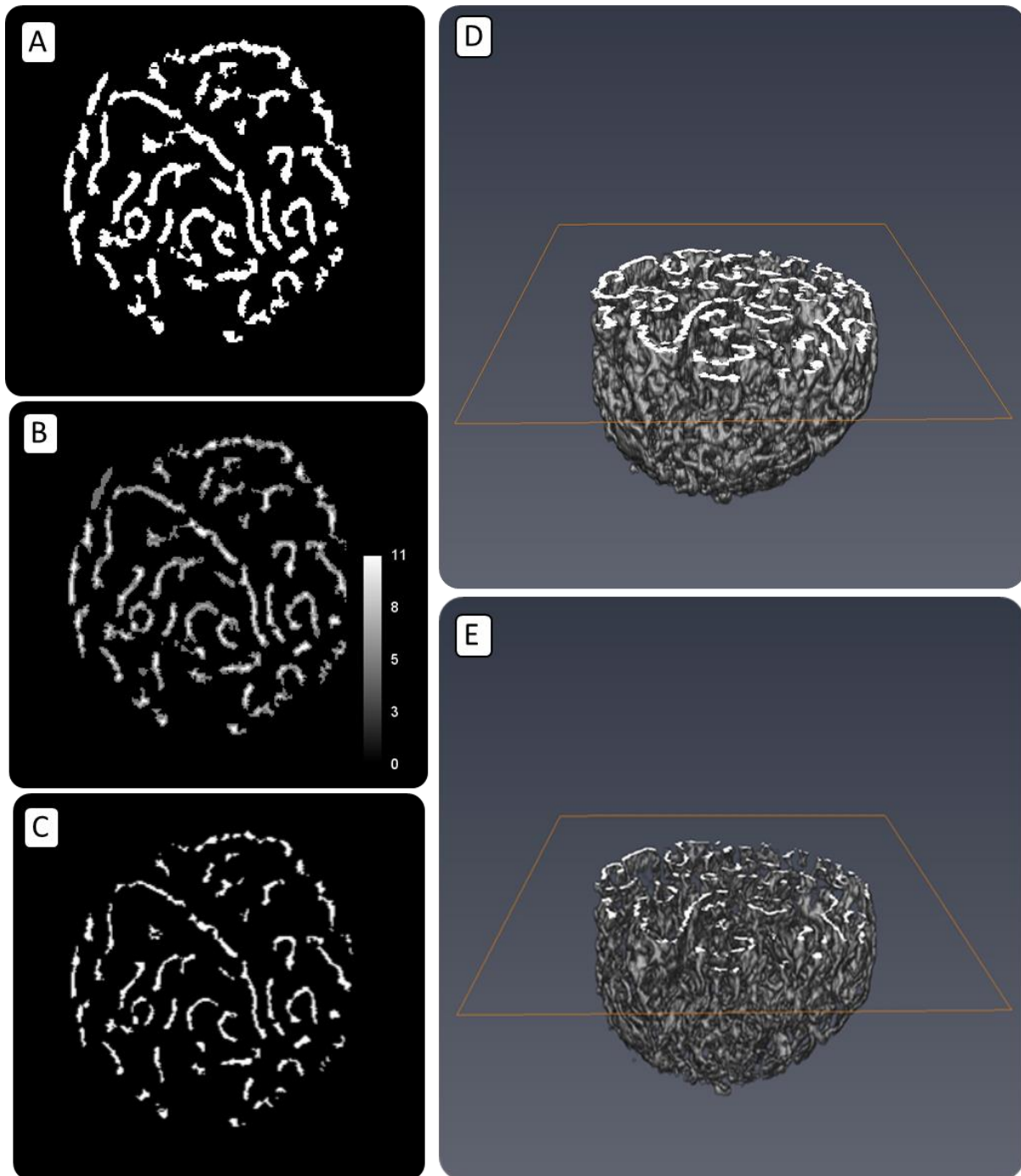


Figure 24. The electron-dense granule phase exhibits a very consistent thickness.

A) Representative binary image of the electron-dense granule phase. B) Exact Euclidean Distance Transform (3D) results in a thickness map with the brightest pixels corresponding to a distance of approximately 11 nm from the border of the phase to its core. C) The thresholded (7.5 nm) electron-dense phase matches the structure of the original data suggesting a thickness of at least  $\sim 15$  nm. D) 3D-reconstruction of original and thresholded (E) data confirms their similarity.



### 5.3 Discussion

The cuticle of byssal threads is a fascinating biological coating combining high hardness and high extensibility and has been subject of numerous studies during the past. However, the cuticle is also the part of byssal threads, which is the least understood. Although a basic concept of its structure-function relationship was established, an unambiguous identification of all components and their assembly remained elusive over decades. The previously presented results of cuticle ultrastructure and composition present a significant contribution to filling some of the gaps inherent to the knowledge about this natural coating.

The cuticle of *M. edulis* byssal threads contains a single layer of biphasic granules, which stands in stark contrast to the multilayered granule structure observed in the cuticles of its related species *M. galloprovincialis* and *M. californianus*. It is conceivable that the observed properties might affect *M. edulis* cuticle mechanics, since the presence of granules was previously correlated with high cuticle failure strain.<sup>42,66</sup> The cuticle of *M. californianus*, which is exposed to high forces due to large crashing waves, contains small granules which significantly increase the matrix-granule interfacial area.<sup>66</sup> In contrast, mussel species, which reside in subtidal, stiller waters - such as *Modiolus capax* and *Perna canaliculus* - show a homogeneous cuticle that lacks biphasic granules.<sup>42,70</sup> In the past, cuticle mechanical properties have been examined by tensile tests and nanoindentation of microtomed transverse thread sections.<sup>42,74</sup> While both experimental setups provided valuable insights into the biomaterials mechanical properties, they are not able to distinguish between matrix and granule mechanics. However, atomic force spectroscopy (AFM) force mapping measurements on the exposed thread cuticles of different mussel species suggested that granules are three-fold softer than the surrounding matrix under semi-hydrated conditions (although under fully hydrated and fully dehydrated conditions, the differences were minimal).<sup>70</sup> Nanoindenter-based nanoscale modulus mapping using nano-dynamic mechanical analysis (nano-DMA) emerged as powerful tool for studying the mechanical properties of complex materials such as the byssus cuticle, which resembles a particle reinforced composite.<sup>25,129</sup> Due to minimal tip penetration into the material, a resolution of 20 nm can be achieved, which would be highly suitable to map the local viscoelastic mechanical response of granules and matrix.<sup>129</sup> However, initial attempts to investigate the mechanical properties of *M. edulis* cuticle by performing nano-DMA were challenging due to difficulties in mapping the region of interest. The sample surface needs to be very smooth in order to perform nano-investigations. Therefore, threads were embedded and a transverse cross-section was fine-polished similar to previously described sample preparation.<sup>42,74</sup> A small gap was observed between the embedding resin and the thread cuticle, which resulted in an edge effect superimposing the signal stemming from the very thin cuticle during nanoscale modulus mapping. In order to

characterize the mechanical properties of *M. edulis* byssal cuticle, the development of a protocol yielding very smooth cross-sections without sample embedding might be a conceivable alternative. Nevertheless, a reasonable interpretation of the cuticle mechanical properties demands a thorough understanding of its ultrastructure and involved components.

Previous models of cuticle mechanics assumed that mfp-1 is the main component of matrix and granules. The presence of mfp-1 was demonstrated by using DOPA and dihydroxyproline as specific markers.<sup>25,69,74</sup> Immunohistochemical localization of mfp-1 in the cuticle was reported to be not of sufficient quality, most probably due to the cuticle's physical and chemical inertness.<sup>68,91</sup> This might also be the reason, why extraction and detection of other components has remained elusive. However, by using next generation sequencing, mRNA transcripts of the cuticle gland tissue identified four previously unknown proteins (mfp-16 - 19).<sup>53</sup> All of them are relatively small (5 - 20 KDa), contain moderate level of tyrosine (3 - 12 %) and are rich in cysteine (7 - 20 %). It was hypothesized that the newly discovered proteins might be located in the cuticle matrix with their cysteine residues serving as redox regulators for the highly abundant DOPA in mfp-1 – a role which is well known from mfp-6 in the plaque. Mfp-6 functions as heterobifunctional protein cross-linker, since it counteracts on the oxidation of DOPA to DOPA-quinone and serves as cross-linking partner for mfp-3.<sup>20,46</sup> *In situ* Raman spectroscopy demonstrated that DOPA-Fe and DOPA-V chelate complexes are present in matrix and granules of Fe-recovered and native threads, respectively and are crucial for stabilization of the load-bearing structure.<sup>25,74</sup> To maintain its cross-linking function, DOPA needs to be available in its reduced form, which could be ensured by concurrent oxidation of thiolates to disulfide bonds of cysteine-rich proteins. However, there existed no experimental indication of their presence in the cuticle. With cysteine residues serving as sulfur source, the present results on elemental analysis provide the first evidence of other proteins than mfp-1 being present in the thread cuticle and substantiate the hypothesis of mfp-16 - 19 as matrix components. However, regions of enriched sulfur were also detected in the granules suggesting that the cysteine-rich proteins are likely also involved in the formation of the biphasic structure. Furthermore, the observed high nitrogen content in granules and matrix and a concurrent constant carbon signal strongly contradict previous hypotheses of fatty acids acting as anionic counterparts to the positively charged mfp-1.<sup>68</sup>

Moderate levels of metal ions, such as Al, Fe and V (~ 1 % of dry weight) in the byssus cuticle have been reported by several studies.<sup>42,72,74</sup> Resonance Raman spectra provided the first evidence for the presence of DOPA-metal cross-links in the cuticle and indicated a higher density of cross-links in the granules than in the matrix.<sup>25</sup> One hypothesis for the different cross-linking density was the presence of a second versions of mfp-1 in the matrix, which contains less posttranslational modified



tyrosine.<sup>25</sup> In light of the elemental analysis, the moderate levels (3 – 12 %) of tyrosine in the sequence of the four newly discovered proteins might account for less DOPA-metal cross-links when compared to the tyrosine level (19 %) of mfp-1.<sup>53</sup> Furthermore, it is also conceivable that the highly abundant sulfur residues coordinate Fe, since cysteine was shown to chelate Fe *in vitro* and to function as ligand in numerous heme thiolate proteins, such as cytochrome P450.<sup>130-132</sup> In order to obtain a more detailed picture about metal coordination in the cuticle and its potential ligands, electron energy loss spectroscopy (EELS) or extended x-ray absorption fine spectroscopy (EXAFS) analysis could provide valuable information, but exceeded the scope of this thesis.

It was shown that mussels are opportunistic in their use of metal ions, since the mechanical properties of metal depleted threads are indistinguishable with either Fe or V.<sup>74</sup> In light of these results, which suggested a similar distribution of different metal ions in the byssus cuticle, the observed partitioning of Fe and V is striking. DOPA-metal coordination resonance bands were shown to be absent in cuticle vesicles and in the cuticle of induced threads, which suggests that metal ions infiltrate byssal threads after their formation.<sup>40</sup> Therefore, the sharp transition of Fe from granule to matrix provokes the hypothesis that V might outcompete Fe via selective accumulation in the granules. Furthermore, V is more concentrated in the granule core and is less concentrated towards the granule-matrix interface. Since metal depleted cuticles, that were subsequently enriched with either Fe or V did not exhibit differences in mechanical properties, a segregation of metal ions for mechanical reasons seems unlikely.<sup>74</sup> However, it is conceivable, that different coordination geometries of ligands in granules and matrix might favor the complexation of V and Fe, respectively. Whereas Fe<sup>3+</sup> was shown to prefer tetrahedral or trigonal prismatic geometries, V<sup>4+</sup> can be found in octahedral coordination.<sup>133</sup> Al seems to be uniformly distributed in granules and matrix and was previously proposed to bind DOPA in a tris-complex.<sup>74</sup> However, up to now, applied spectroscopic analyses were not suitable to detect DOPA-Al cross-links. Therefore, further work is required to elucidate the origin of metal distribution in the byssal thread cuticle. For example, metal depleted threads could be separately and successively treated with Fe and V and analyzed with TEM-EDS in order to shed light on the accumulation hypothesis. However, the observed results suggest that the density and organization of metal complexation can be fine-tuned, which is an exciting new finding and might influence the design concepts of future mussel-inspired coatings.

In addition to Fe, iodine is co-localized in the cuticle matrix. It's origin and role in the byssus cuticle remain unknown, but natural organohalogenes, such as halogenated DOPA and tyrosine, have been reported to be widely distributed - especially in materials produced by marine organisms, but very likely also in the cuticles of arthropods.<sup>134-136</sup> For example, the jaws of the marine worm *Nereis* are known as non-mineralized, but very hard biological material, similar to the byssal thread

cuticle.<sup>137</sup> It was demonstrated that the jaws contain significant amounts of Cl, Br and I associated with a variety of post-translationally modified amino acids.<sup>138</sup> Notably, iodine was found to be concentrated in proximity to the external jaw surfaces, but seemed not to influence the mechanical properties of the biomaterial.<sup>138</sup> Instead, due to the specific localization of iodine, the presence of halogenated di- and tri-tyrosines was proposed to mediate protein cross-linking resulting in a casing within the outer jaw regions.<sup>138</sup> Conceivably, iodinated tyrosine or DOPA could serve a similar function in the byssus cuticle by cross-linking the different matrix proteins. Along these lines, iodine was demonstrated to oxidize DOPA residues of mfp-1 *in vitro* and thus, enabled protein cross-linking.<sup>139</sup> Conceivably, the observed iodine in the cuticle matrix could serve a similar role and crosslink DOPA containing matrix proteins. However, further work is required to identify potential tyrosine or DOPA derivatives and to elucidate their role in the cuticle matrix. Given the fact that all proposed cuticle proteins contain serine residues, the observed phosphorus signal might stem from posttranslational modifications of serine to phosphoserine groups.<sup>53,68</sup> Taken together, the results of byssus cuticle elemental analysis provide exciting new insights into this complex biological coating and pave the way for a more profound understanding of its composition.

With this knowledge, a three-dimensional understanding of granule and matrix might allow to elucidate the origin and role of these complex structures. The 3D-reconstruction of the electron-dense granule phase revealed that it forms a highly complex interconnected system with planar structures, which are connected via elongated tubes. Furthermore, the well-defined volume fractions of five different granules suggest a highly controlled and defined formation process. Based on the observed sulfur signal in matrix and granules, it is conceivable that the electron-dense phase consists of mfp-1, whereas the cysteine-rich proteins can be found in the matrix and most probably also account for the electron-light granule phase. Along these lines, the presence of metal ions could account for the observed contrast in electron-density. Mfp-1 is a large, highly repetitive (AKPSYPPTYK)<sub>n</sub> and mostly unstructured protein. It consists of 20 mol % lysine and 10 mol % of each of the following amino acids: alanine, proline, serine, threonine, tyrosine, trans-4 hydroxyproline (Hyp), trans 2, 3- cis 3, 4-dihydroxyproline (diHyp), and DOPA.<sup>68</sup> Its grand average of hydropathy (GRAVY) can be calculated on the Bioinformatics Resource Portal Expasy by using the ProtParam tool, where increasing positive scores indicate hydrophobicity. The GRAVY value of mfp-1 was calculated to be -1.357, indicating that mfp-1 is very hydrophilic. The calculated GRAVY values of mfp-16 – 19 ranged between -0.666 (mfp-16) and 0.616 (mfp-19) indicating that all potential matrix proteins are less hydrophilic than mfp-1. Conceivably, the opposite biochemical properties might cause a separation of the proteins, especially between mfp-1 and mfp-19. Along these lines, the hydrodynamic radius of mfp-1 was measured to be  $10.5 \pm 1.2$  nm.<sup>140</sup> The calculated thickness of at least  $\sim 15$  nm of the



electron-dense phase would correspond well to two facing molecules of mfp-1, which are arranged in sheet-like structures. The calculated excess of matrix volume might be sufficient to create the observed distances between mfp-1 phases. The formation of such complex structures is well known from self-assembling block copolymers.<sup>141</sup> Depending on a variety of parameters, amphiphilic block copolymers attain different morphologies, such as lamellae, spherical and cylindrical micelles and bicontinuous gyroids.<sup>141</sup> Therefore, it seems likely that the molecules involved in the complex granule structure exhibit an amphiphilic character; however the details remain elusive and the previously discussed model remains theoretical without definite evidence for the presence of matrix proteins in the cuticle of byssal threads. Further work is required to elucidate the complex interplay of matrix and granule components. Based on the presented hypotheses and calculations, the matrix proteins are likely highly cross-linked and hydrophobic. This might be the reason why matrix proteins were not detected with previous acetic extraction methods. Extraction protocols based on polar solvents and enzymatic treatment might result in protein fragments that can be assigned to mfp-16 – 19. Alternatively, correlative light and electron microscopy (CLEM) might offer a good investigation strategy, since it can combine nano-level resolution with protein-specific stains or other signals.<sup>142</sup>

## 5.4 Conclusion

The combined studies within this thesis demonstrate for the first time that the matrix of byssus cuticle does not consist of fatty acids as previously hypothesized, but that rather cysteine-rich proteins might contribute to the complex cuticle architecture. Moreover, the elemental analysis revealed a partitioning of metal ions, which was never observed before and might impact the design of future mussel-inspired coatings. Furthermore, the specific localization of iodine provokes the hypothesis that it might be involved in matrix protein cross-linking, a role which was observed in another marine species. 3D-reconstruction of cuticle granules presented a detailed depiction of their complex and highly regulated ultrastructure and paves the way for potential structural and functional models. Taken together, the results of combined high resolution electron microscopy, elemental mapping and 3D-reconstruction greatly broadened our understanding of *M. edulis* byssus cuticle and forms a substantial basis for the in-depth analysis of the cuticle assembly process, which will be presented in the next chapter.

## 6. DYNAMIC FORMATION PROCESS OF BYSSAL THREAD CUTICLE

Byssal thread assembly is based on highly localized and dynamic processes that occur hidden from our view in the mussel foot ventral groove. Thus, investigating this dynamic formation process *in situ* is accompanied by exceptional technical challenges. However, early electron microscopy investigations of the mussel foot gland tissue established a profound understanding of the thread protein synthesizing cells, the protein storage vesicles and their secretion.<sup>73,75</sup> The secretory vesicles containing the cuticle precursors have been shown to possess a complex ultrastructure consisting of an electron-dense core presenting biphasic structures and one or more outer layers.<sup>70,73</sup> It seems likely that the complex structure observed in the vesicle core can be related to the biphasic granules in the cuticle, but an explicit assignment of one of the outer layers to the cuticle matrix has remained elusive. The previously presented results (chapter 5) on cuticle ultrastructure and composition strongly suggest the presence of other proteinaceous cuticle components, which is supported by previous hypotheses for cysteine-rich proteins in the cuticle based on transcriptomic data.<sup>53</sup> However, as of yet, they could not be assigned to one of the observed phases in secretory vesicles. The indication of sulfur-containing macromolecules in secretory vesicles within cuticle gland tissue would be an important step towards unraveling the origin of cuticle granules and matrix.

Although the winding structure observed in the cuticle vesicle cores was previously hypothesized to be the result of a maturation process, the physicochemical triggers initiating this process remain unknown.<sup>73</sup> The results on combined cuticle investigations within this thesis (chapter 5) suggest that the electron-dense phase of cuticle granules might consist of mfp-1, whereas cysteine-rich proteins potentially create the spacing between these structures and can also be found in the matrix. The observed phase separation might be triggered due to the opposing biochemical properties of the proteins, with mfp-1 being hydrophilic and mfp-16 – 19 being more hydrophobic. The investigation of a similar elemental distribution among cuticle precursors in the gland tissue would allow the development of a coherent model of phase-separation and granule formation.

A thorough understanding of the composition and ultrastructure of byssal thread cuticle and its precursors in the tissue is crucial to extract information about the structure-function relationship. However, in order to improve upon current generation of bio-inspired materials it is also essential to understand the physical and chemical driving forces guiding the rapid self-assembly of this fascinating material in detail. A recent study based on the synergistic combination of histological staining and confocal Raman microspectroscopy provided valuable insights into this rapidly occurring process.<sup>40</sup> This approach enabled the localization of cuticle precursors in the cuticle gland tissue and



showed that spatially organized vesicles containing pre-packed thread building blocks coalesce and self-assemble into locally organized architectures.<sup>40</sup> Furthermore, the results indicated that DOPA-metal interactions are not necessary for cuticle assembly. However, tracking changes in the precursors' ultrastructure and composition from their production and storage in the tissue to their secretion and self-assembly, requires a resolution that is beyond the limit of light microscopy techniques.

Therefore, I undertake a detailed *in situ* investigation of *M. edulis* cuticle gland tissue and its vesicles as well as of the induced secretion of precursors and their assembly. By combining high-resolution electron microscopy with elemental analysis, I demonstrate that the elemental distribution within tissue vesicles resembles the one of the byssus cuticle. This result allows for the first time to assign specific vesicle phases to the respective phases in the mature cuticle. Moreover, I show that metal ions are absent within the storage vesicles of cuticle precursors, which is highly consistent with previous observations.<sup>40</sup> The 3D-reconstruction of vesicles phases and following calculation of vesicle phase volume fractions suggest a highly regulated system, which is consistent with the results presented in chapter 5. Finally, artificial induction of vesicle secretion and thread formation revealed critical high-resolution insights into the formation of the byssal thread cuticle.

## 6.1 Material & Methods

### 6.1.1 Chemical fixation and embedding

Blue mussels (*M. edulis*) from the North Sea were purchased from the Alfred-Wegener-Institut and maintained at ~ 14 °C in an aquarium with artificial salt water. In order to investigate the ultrastructure and composition of thread cuticle precursors, adult mussels (5 - 8 cm in length) were cut open at the posterior retractor muscle and the mussel foot was removed with a scalpel. The foot was carefully rinsed with cold water and blotted with a paper towel to remove the mucus. For easier preparation of thin transverse sections, the foot was pre-fixed (3 % glutaraldehyde, 1.5 % paraformaldehyde, 650 mM sucrose in 0.1 M cacodylate buffer pH 7.2) for 30 min at 4 °C. The firm tissue could then be cut into very thin transverse sections comprising the groove and part of the gland tissue. Fixation was carried out for 2 h at 4 °C in the same buffer as previously described. Samples were rinsed 5 x with 0.1 M cacodylate buffer pH 7.2 at 4 °C and post-fixed with 1 % osmium tetroxide for 1 h at 4 °C. Tissue samples that were prepared for elemental analysis with TEM EDS were not treated with osmium tetroxide. Rinsing of the samples in 0.1 M cacodylate buffer pH 7.2 (3 x 5 min at 4 °C) was followed by dehydration in ethanol (50 %, 70 %, 90 %, 3 x 100 %) for 10 min each

step at RT. Samples were embedded either in low viscosity Spurr's resin (Electron Microscopy Sciences, # 14300) for TEM or in Hard Plus resin 812 (Electron Microscopy Sciences, # 14115) for FIB-SEM and polymerized at 70 °C for at least 48 h.

### **6.1.2 Induced secretion and thread formation**

To obtain a more dynamic view on cuticle assembly, protein secretion was induced by injecting 0.56 M KCl solution in the base of two mussel feet as previously described.<sup>40,60,85</sup> A mussel foot was dissected after ~ 5 min following induction to investigate protein secretion and another one after ~ 20 min to investigate the induced thread and its cuticle. The whole foot was subsequently transferred to a fixative solution (3 % glutaraldehyde, 1.5 % paraformaldehyde, 650 mM sucrose in 0.1 M cacodylate buffer pH 7.2) in order to preserve the secretion and formation process. After pre-fixation, the samples were further cut, chemically fixed and embedded as described in the previous chapter. During fixation, the induced thread detached from the surrounding tissue and was embedded separately.

### **6.1.3 Sample preparation for TEM**

Resin blocks were trimmed to expose the tissue sample and thick sections (500 nm) were cut and stained afterwards for 10 min with toluidine blue in order to identify the region of interest. Samples were then trimmed further to obtain a small sample size suitable for preparing ultrathin sections and the exposed tissue was stabilized at the edges by applying a thin layer of glue. Ultrathin sections of 100 nm were prepared using a PowerTome Model XL ultramicrotome (Boeckeler Instruments, Inc.) and mounted on carbon coated Cu grids (200 mesh) for imaging and on Lacey carbon coated Cu grids (200 mesh) for EDS measurements. Grids were post-stained with uranyl acetate for 10 min in order to reveal the biphasic structure.

### **6.1.4 TEM-EDS**

Dark-field electron imaging and EDS were performed on a Jeol JEM ARM200F equipped with a cold field-emission electron source (operated at 200 kV) and an emission current of 15  $\mu$ A. Overview elemental maps were acquired at a magnification of 50 000 x with a pixel size of 17 nm x 17 nm and an exposure of 1 sec per pixel. Elemental maps at higher magnification (100 000 x) were acquired with a pixel size of 30 nm x 30 nm using a Silicon Drift Detector (SDD).



### 6.1.5 FIB-SEM

Resin blocks containing the samples were polished in order to expose the tissue on the block surface. Sample was sputter coated with three Carbon layers (~ 5 nm each) and one platinum layer (~ 5-10 nm) and transferred to the Zeiss Crossbeam 540 (Carl Zeiss Microscopy GmbH, Germany). At the region of interest, a trench for SEM imaging was milled into the sample surface using the 65 nA FIB current at 30 kV acceleration voltage. The resulting cross-section was fine polished using the 1.5 nA FIB probe at 30 kV. Thin slices of material were removed in a serial manner by FIB milling (300 pA, 30 kV) and after each milling step (slice thickness 17.5 nm), the specimen was imaged by SEM at 2 kV acceleration voltage using the in-lens secondary and backscattered electron detector. The image resolution was 2048 x 1536 pixels, lateral image pixel size was 12.4 nm. Images were recorded using line averaging (N = 4) and a dwell time of 200 ns.

### 6.1.6 Image processing

The resulting back-scattered electron images were processed using the SPYDER<sup>3</sup> (Scientific Python Development Environment) (Python 3.6) software. Custom-written python scripts were developed and provided by Luca Bertinetti (Max Planck Institute of Colloids and Interfaces, Golm, Germany). Images were automatically aligned using enhanced correlation coefficient alignment. Total variation denoising was performed by applying the Chambolle's projection algorithm (100000 iterations, weight 0.07, 0.001 eps) in 3D mode.

### 6.1.7 Segmentation

Segmentation of cuticle vesicles was performed using the ZIB version of Amira 3D (Thermo Fisher Scientific, USA). Vesicle shapes of 28 individual granules were segmented manually from 392 processed back-scattered electron images using the brush tool. The inner phase, which corresponds to the biphasic structure as well as the surrounding phase were automatically segmented using the Magic Wand tool. 3D visualization of both phases was realized by volume rendering of segmented structures. Volumes of all phases were calculated using the Measure and Analyze tool in Amira. The volume fractions for inner phase (ip) and surrounding outer phase (op) of each individual vesicle were calculated as follows:

$$V_{\text{total}} = V_{\text{ip}} + V_{\text{op}} \quad \phi_{\text{ip}} = V_{\text{ip}} / V_{\text{total}} \quad \text{and} \quad \phi_{\text{op}} = 1 - V_{\text{ip}}$$

The mean values and standard deviation were calculated with OriginPro 2015.

## 6.2 Results

### 6.2.1 Development of a fixation protocol suitable for mussel foot tissue

The mussel foot is comprised of secretory glands, in which the thread proteins are produced and stored. A key first step in understanding byssus cuticle assembly is the ultrastructural characterization of secretory vesicles in the cuticle gland tissue via high-resolution imaging techniques. However, an optimal sample preparation for nanoscale investigations in high vacuum faces several challenges when it comes to soft tissues, such as the mussel foot. Tissue cells consist to a high percentage of water, which has to be entirely replaced before imaging in high vacuum environments.<sup>143</sup> Furthermore, the soft tissue needs to be infiltrated and embedded in resin in order to prepare thin sections suitable for TEM and to increase its stability under the focused ion or electron beam. Due to mainly light elements, such as nitrogen, carbon, hydrogen and oxygen, tissues usually present a low contrast when studied with electron microscopy and need to be stained (e.g. with osmium tetroxide or uranyl acetate).<sup>143</sup> The ultrastructural investigation of the mussel foot gland tissue and the cuticle assembly with FIB-SEM and TEM required the development of a fixation and embedding protocol suitable for the large and soft mussel foot tissue, which was accompanied with exceptional technical challenges.

In order to preserve the ultrastructural details, biological samples are usually either chemically or cryo-fixed. It is assumed that low temperature fixation, such as high-pressure freezing (HPF), is less distorting than conventional chemical fixation and therefore better suited for optimal preservation of ultrastructure in larger samples.<sup>144</sup> The fixation via HPF happens within milliseconds, while chemical fixation protocols can take up to one hour.<sup>145</sup> For this reason, HPF was chosen as fixation method. However, preparing the sample for HPF faced several challenges. Firstly, the mussel foot is very soft and covered in a layer of mucus, which hampered the preparation of very thin transverse sections due to slipping. Secondly, although the location of the cuticle gland within mussel foot tissue is roughly known, its definite position within transverse sections cannot be determined without differentiating methods, such as histological stains.<sup>40</sup> Therefore the cuticle gland location was estimated and a small tissue piece was excised from the region closely to the surface of the mussel foot on both sides of the ventral groove where the cuticle gland is supposed to be located. However, the sample thickness for HPF is limited by the space available within sample carriers, which is  $\sim 200 \mu\text{m}$ .<sup>145</sup> In order to investigate the storage site of vesicles in the gland and their secretion site close to the groove, it is essential to maintain a good understanding of the tissue orientation during sample preparation. However, tracking the orientation was impeded due to the small sample size and osmium-staining, which resulted in an entirely black stained sample. Investigation of the sample



surface with SEM revealed the presence of tissue vesicles but was not adequate to differentiate between core and cuticle vesicles, since only their surface was imaged (Figure 25 A).

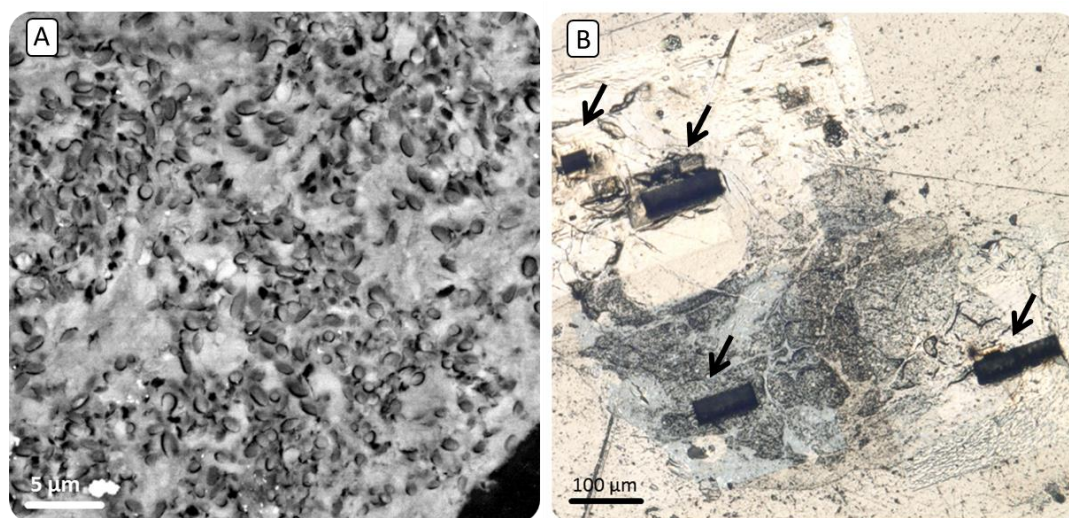


Figure 25. Identification of cuticle vesicles within the gland tissue.

A) SEM image of embedded mussel foot tissue. Numerous vesicles can be seen at the sample surface but a clear distinction between core and cuticle vesicles remains impossible. B) Several trenches were milled into the sample surface with the FIB in order to identify the region of interest.

Therefore, it was necessary to find the region of interest by milling several trenches into the sample and subsequently imaging the resulting surfaces (Figure 25 B). However, since the available time for sample analysis with FIB-SEM is very limited, a modification of the sample preparation protocol aiming for a better orientation within the sample was required. Although chemical fixation was reported to be inferior to HPF protocols, it offered several advantages for mussel foot tissue sample preparation.<sup>144</sup> Firstly, it enabled the pre-fixation of the whole mussel foot, which resulted in firm tissue and as a consequence in easier preparation of very thin transverse sections. Furthermore, slightly larger tissue pieces were excised, comprising the cuticle glands on both sides of the groove and the groove itself as point of orientation. This approach allowed the easy orientation within the sample after embedding and osmium-staining for both investigation techniques – FIB-SEM and TEM. A detailed description of the final chemical fixation and embedding protocol can be found in the material & methods section (chapter 6.1.1).

## 6.2.2 Ultrastructure of cuticle vesicles in gland tissue

In order to investigate byssus cuticle assembly, the production and storage site of cuticle vesicles within the mussel foot tissue of *M. edulis* was examined using electron microscopy. Resulting FIB-SEM back-scattered electron (BSE) images show a good preservation of the cellular ultrastructure (Figure 26 A). Consistent with previous histological studies, core and cuticle gland are interdigitated

with no absolute boundaries between cells.<sup>40</sup> Cuticle gland cells contain vesicles with a characteristic internal structure comprising two or three phases with heterogeneous electron-density (Figure 26 A). Notably, the biphasic structure was not visible without post-staining, which was also described in early electron microscopy studies.<sup>73</sup>

To identify the location of the cuticle gland in resin embedded samples prepared for TEM investigation, the sample had to be trimmed several times in order to yield a very small region of interest that could be cut with the ultramicrotome. Thick sections (500 nm) were stained with toluidine blue for better contrast in order to identify the gland tissue and ultrathin slices (100 nm) of the adjacent region were prepared for TEM investigations. High-resolution TEM of post-stained tissue revealed biphasic structures in the vesicle cores similar to those observed in the thread cuticle (Figure 26 B). It should be noted that the biphasic structure and surrounding phase in the TEM image correspond to the dark core and bright phase in the FIB-SEM BSE image, respectively. Whereas one of the phases seems to match the surrounding electron-density, the second phase appears to be brighter. The biphasic structure and surrounding phase are partially enclosed on one side of the vesicle by a crescent shaped third phase (Figure 26 B).

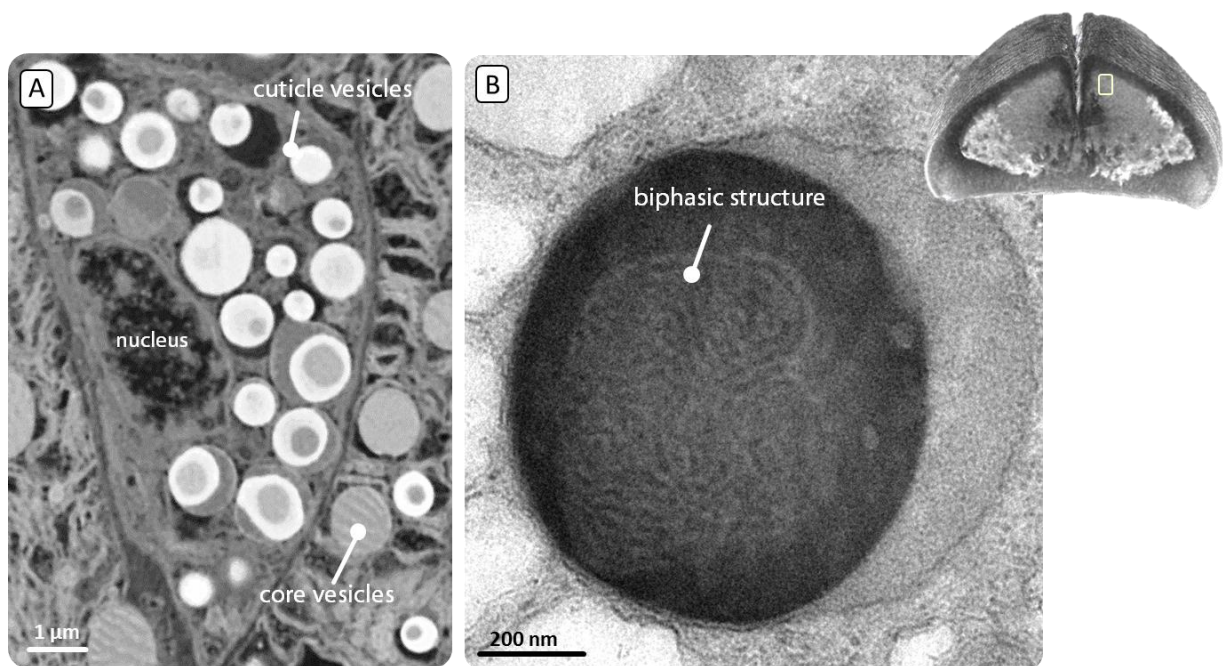


Figure 26. Cuticle gland cells contain vesicles with different phases.

A) FIB-SEM BSE image of mussel foot tissue showing interdigitated core gland and cuticle gland cells containing thread precursors. B) High-resolution TEM image of a cuticle vesicle exhibiting different electron-dense phases and a biphasic structure in the core. The transverse mussel foot section illustrates the region of investigation.

The above presented results underpin the long-running discussion about other components contributing to the observed phase-separation and difference in electron-density. The previously presented results (chapter 5) on cuticle elemental analysis strongly suggest the presence of an



additional proteinaceous component. To specifically locate the newly identified component in the secretory vesicles, EDS measurements were performed on cuticle gland tissue samples.

### 6.2.3 Elemental composition of cuticle vesicles

Early electron microscopy studies of cuticle vesicles within gland tissue of *M. galloprovincialis* revealed different electron-dense phases that were also reported to have a different liability to protease treatment.<sup>73</sup> This observation suggested the presence of different macromolecular precursors and stands in stark contrast to the previous detection of only one protein (mfp-1) in the thread cuticle. Along these lines, the previously presented results on the elemental analysis of thread cuticle suggest the presence of other proteinaceous components. In order to investigate, if a similar distribution of elements can be found at the production and storage side of thread cuticle precursors, the cuticle gland was analyzed. The combination of high resolution imaging with EDS measurements on thin sections of resin-embedded gland tissue allowed the characterization of each vesicle phase. However, similar to the elemental investigations of the thread cuticle, a very high spatial resolution was required to resolve all details. Imaging was performed in STEM mode using a HAADF detector and the corresponding elemental maps were acquired with an EDS detector.

Comparison of STEM images and resulting elemental maps revealed a high nitrogen signal that overlaps with the position of cuticle vesicles (Figure 27 A, B), suggesting that all vesicles phases contain highly concentrated proteins. This result is consistent with the observed nitrogen signal in cuticle matrix and granules (chapter 5.2.2, Figure 17). The nitrogen signal of the crescent phase, which is not present in all vesicles, indicates protein content; however most likely at lower concentrations (Figure 27 C). Similar to the observed distribution in the cuticle, sulfur is not homogeneously present within cuticle vesicles in the gland (Figure 27 D). Consistent with the observed sulfur distribution within the native thread cuticle (chapter 5.2.2, Figure 17 D), a higher sulfur-content was detected in the outer phase than within the biphasic structure. Plotting the percent composition of sulfur in the region of interest (Figure 27 D) reveals that sulfur is approximately twice as concentrated in the outer vesicle phase, than in the core phase (Figure 27 D). It should be noted that the elemental analysis likely includes carbon and oxygen from the embedding resin, which results in an underestimation of other elements. The resulting percent composition maps are therefore considered as comparative without exact quantitative determination of elements.

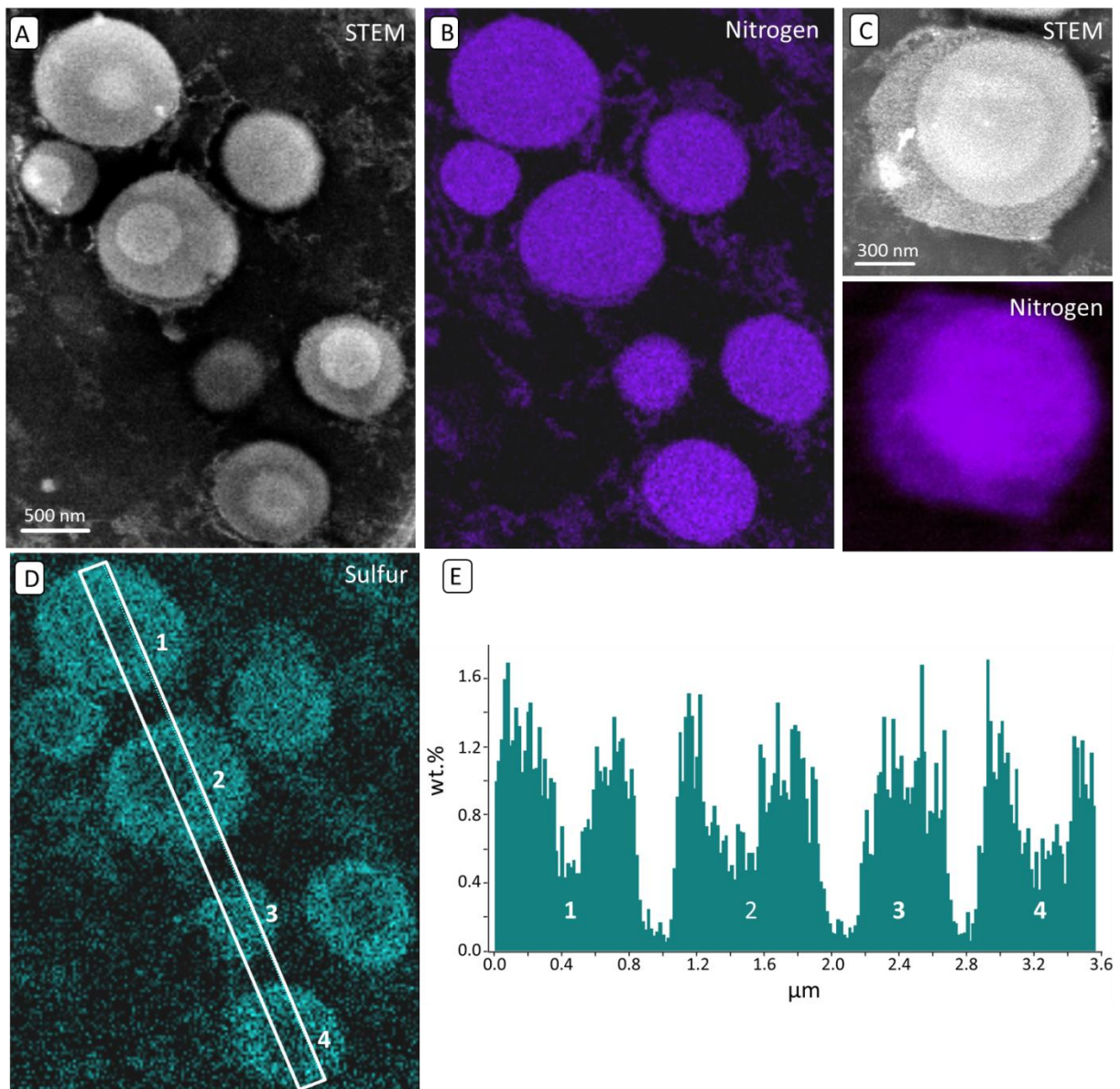


Figure 27. Nitrogen and sulfur composition of cuticle gland vesicles.

A) STEM HAADF image of cuticle vesicles exhibiting different electron-dense phases. The phases located in the center contain the biphasic structures. B) Percent composition map of nitrogen reveals that all phases contain proteins. C) Nitrogen is less concentrated in the outer crescent granule phase. D) Sulfur is not homogeneously distributed throughout the vesicle phases. E) Plotted percent composition in the region of interest (D) shows that sulfur is approximately two-fold less concentrated within biphasic structures in the vesicle cores.

In order to investigate, if the lower sulfur content can be assigned to the location of the biphasic structure within cuticle vesicles, elemental analysis was performed at higher magnification. Due to staining of the sample with uranyl acetate, the biphasic structure of all three vesicles can be observed in STEM HAADF mode (Figure 28 A). Resulting elemental maps based on the percent composition reveal that the lower sulfur signal clearly overlaps with the location of the biphasic structure (Figure 28 B). The distribution of nitrogen, carbon and uranium seems to be homogeneous in all vesicle phases (Figure 28 C, D, E). Consistent with the elemental analysis of the cuticle, P and Al



can be detected within secretory vesicles, but seem not to be concentrated at the vesicle surface (Figure 28 F, H). Furthermore, Cl can be detected in all vesicle phases (Figure 28 G). Similar to its location at the thread cuticle surface, Si seems also to be concentrated at the vesicle surface (Figure 28 I). Notably, neither Fe nor V can be found in any of the vesicle phases, which supports previous findings that suggest the infiltration of metal ions following structural assembly of the cuticle.<sup>40</sup> However, Al does appear to be co-localized in vesicles, although at very low levels (Figure 28 H). Finally, it is worth noting that iodine is not present in detectable quantities within the secretory vesicles, although it was localized in the matrix phase of native thread cuticles.

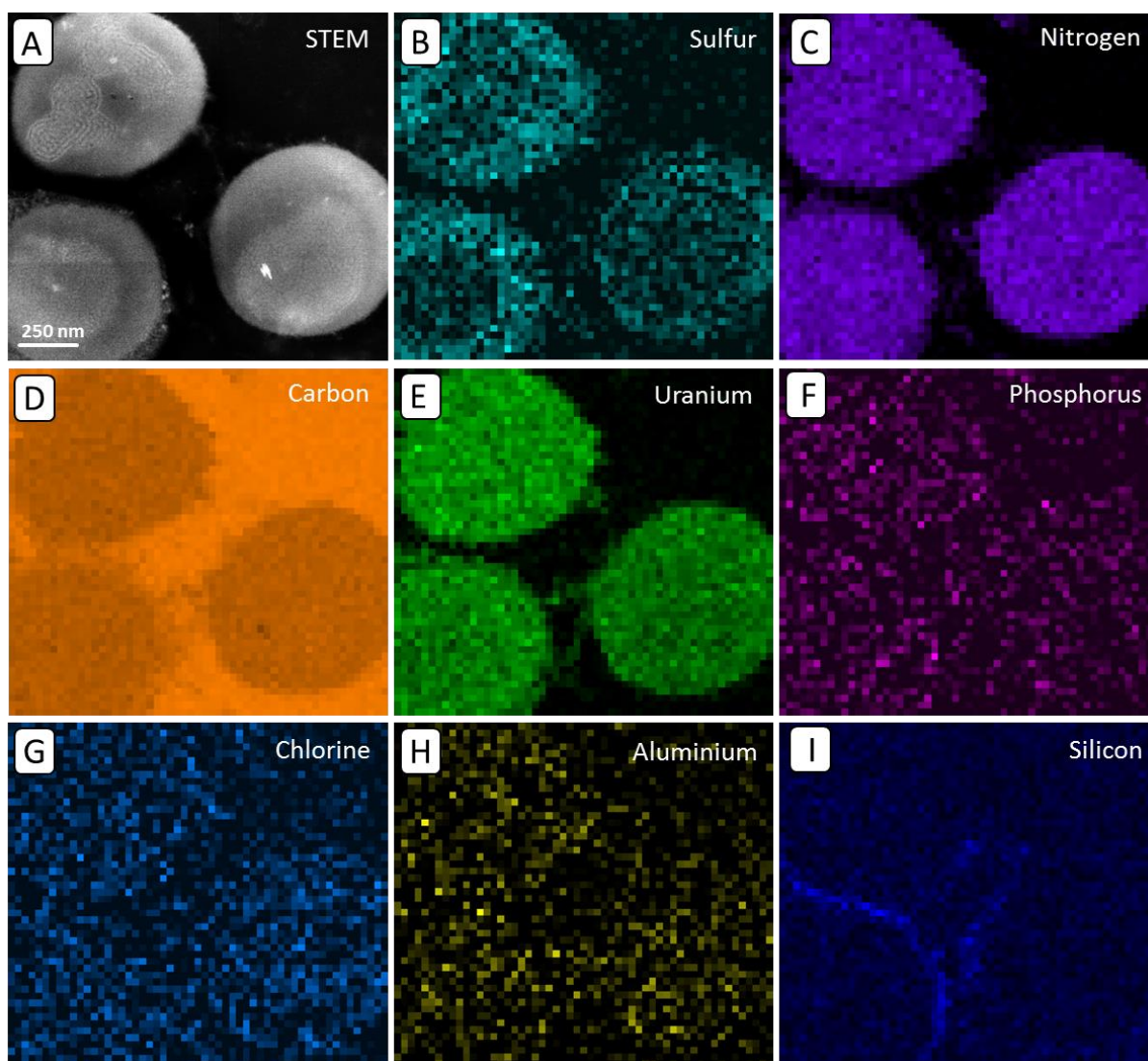


Figure 28. Elemental composition of cuticle gland vesicles.

A) STEM HAADF image of post-stained cuticle vesicles show the biphasic structures and surrounding phase. B) Lower sulfur content is observed where the biphasic structure is located. C), D) and E) N, C and U are evenly distributed within all phases. F), G) and H) P, Cl and Al can be detected within cuticle vesicles, whereas Si seems to be accumulated at the vesicle surface (I).

The results presented here regarding elemental analysis strengthen the previously observed results on the elemental composition of byssus cuticle. Especially the constant nitrogen signal and distinct distribution of sulfur are highly consistent and suggest that the biphasic structure forms the cuticle granules, whereas the surrounding phase can be related to the matrix. Furthermore, the data strengthen the hypothesis of at least one additional cysteine-rich proteinaceous cuticle component. The absence of metal ions prior to thread assembly provides crucial information for the production of mussel-inspired coatings.

### 6.2.4 3D-reconstruction of vesicle phases

To acquire a better understanding of the 3D-structure of different vesicle phases, FIB-SEM was performed on cuticle gland tissue. Due to the improved sample preparation protocol described in chapter 6.2.1, the position of the cuticle gland was easily identified and a trench was milled with the FIB in the region of interest (Figure 29). The resulting surface was scanned with a pixel size of 12.4 nm and an image was taken every 17.5 nm resulting in an image stack (392 images) suitable for a detailed reconstruction of cuticle vesicles in three dimensions (Figure 29).

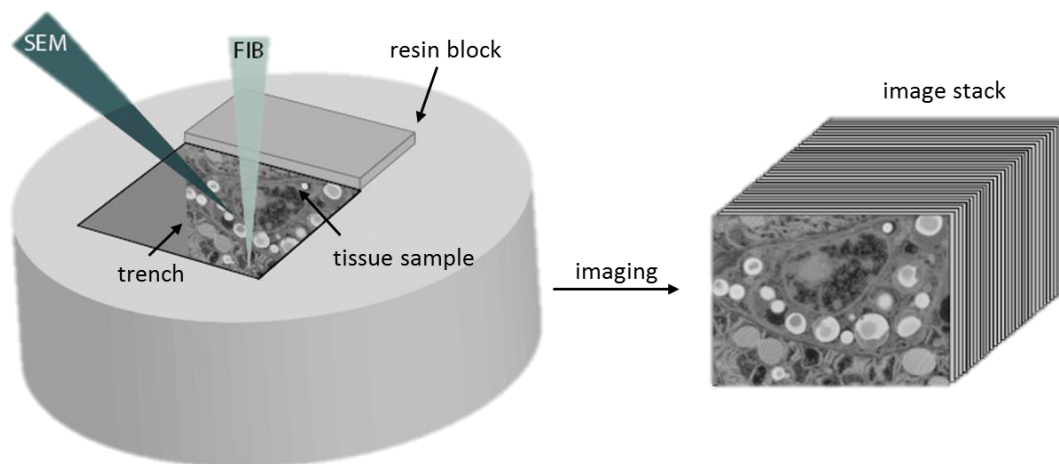


Figure 29. FIB-SEM setup for imaging the gland tissue vesicles in three dimensions.

FIB-SEM of cuticle gland tissue resulted in a stack of 392 back-scattered electron images suitable for the detailed reconstruction of cuticle vesicle phases.

Processing of the resulting back-scattered electron images is a crucial step before the nanoscale structures can be reconstructed, since the images need to be aligned and contain statistical noise. Custom-written python scripts provided by Luca Bertinetti (Max Planck Institute of Colloids and Interfaces, Golm) were used to align and denoise the original images by carefully selecting appropriate parameters. The vesicle shape as well as the biphasic and surrounding structure of twenty-eight individual cuticle vesicles were segmented using the Amira 3D software,



which assigns each pixel of an image to a created label. Similar to the images of cuticle matrix and granules, these images contained many pixels with similar grey values and thus segmentation of twenty-eight vesicle shapes had to be performed manually by going through 392 single images. Within the created vesicle labels, the other two phases could be automatically segmented due to their different grey values. Volume rendering of the segmented data presents a detailed depiction of their complex ultrastructure (Figure 30).

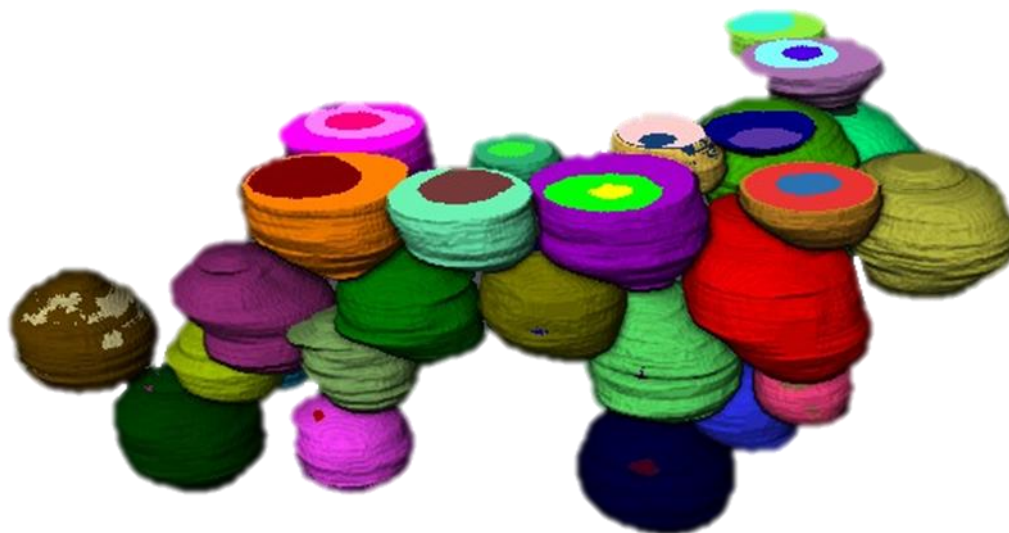


Figure 30. 3D-reconstruction of secretory cuticle vesicles reveals the different phases.

3D-reconstruction not only provides a better understanding of the cuticle vesicle ultrastructure, but also enables accurate calculation of the volume fractions of the different phases. Figure 31 shows the average volume fraction of the biphasic and surrounding phase of twenty-eight reconstructed cuticle vesicles, since the crescent third phase was not present in all vesicles. The volume fractions of both phases appear to be very similar in all analyzed vesicles suggesting a highly controlled formation process and relation of precursors, which is very consistent with the results of cuticle structures (chapter 5.2.3, Figure 23 A). The average volume fraction of the surrounding phase is  $\sim 0.84$  whereas the one of the biphasic structure was calculated to be  $\sim 0.16$  (Figure 31).

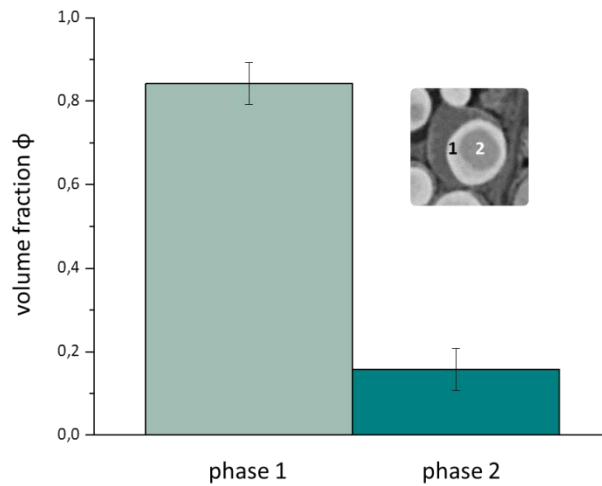


Figure 31. Mean volume fraction  $\phi$  of cuticle gland vesicles. Calculated volume fractions  $\phi$  are approximately five times higher for the surrounding phase ( $\sim 0.84$ ) when compared to the volume fractions of biphasic structures ( $\sim 0.16$ ).

### 6.2.5 Induced thread formation

Understanding the physicochemical driving forces of cuticle assembly is an important factor for the improvement upon current generation of mussel-inspired coatings. Induced thread formation proved to be a helpful tool for studying the self-assembly of thread precursors.<sup>40,146</sup> Injecting KCl into the pedal nerve at the base of the foot leads to muscle contraction and vesicle secretion into the foot groove.<sup>40</sup> Whereas the mussel foot is extended and constantly in motion once the mussel is cut open (Figure 32 A), it is assumed that the mussel foot is essentially paralyzed during induced thread formation (Figure 32 B), which allows one to study spontaneous rather than biologically controlled aspects of cuticle assembly process.<sup>40</sup> As a result, the morphology of the thread is impaired (Figure 32 C); however, previous findings indicated that the basic structure of the different thread parts including the cuticle, are well-preserved.<sup>40</sup>

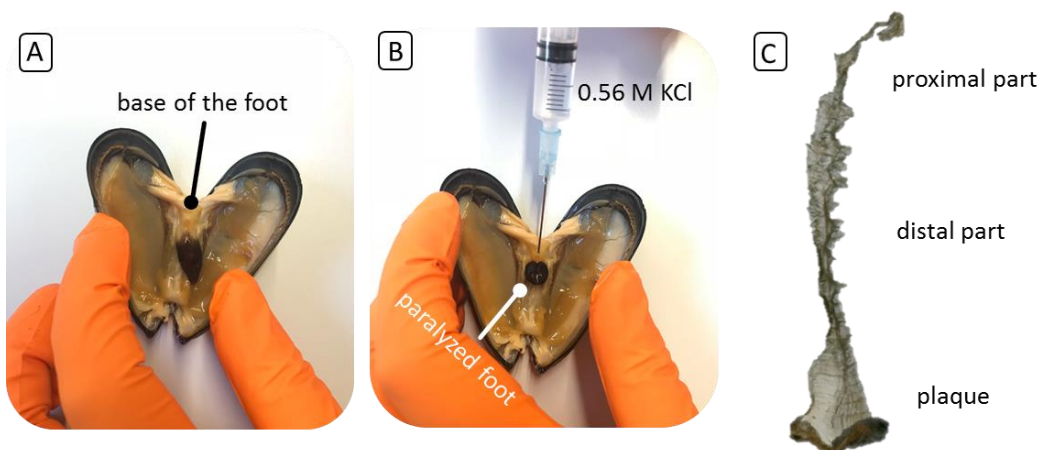


Figure 32. Induced thread formation.



A) *M. edulis* exhibiting its extended foot. B) Secretion of thread precursors into the groove and thread production is induced by injecting 0.56 M KCl into the base of the foot. The mussel foot is paralyzed, which prevents biologically controlled thread formation. C) The morphology of induced threads differs from native threads.

The process of vesicle secretion was conserved by instant chemical fixation of mussel foot tissue following induction with KCl, which required careful timing in order to observe the secretion as it occurred.<sup>46,60,85</sup> With the ventral groove serving as point of orientation, the region of interest (marked with a yellow rectangle in the representative mussel foot transverse section, Figure 33) could be identified. Electron microscopy images show that cuticle vesicles are arranged in rows within ciliated epithelial cells and are released into the ventral pedal groove (Figure 33 A). Their heterogeneous appearance seems to be unaltered. However, when the vesicles come in contact with the ventral groove area and its physicochemical conditions, some of them seem to coalesce right before secretion (Figure 33 B) showing a liquid-like behavior. The coalescence of vesicles inside the groove has been previously observed and these results are consistent with early TEM studies on secretory vesicles that report an elongated shape and the disorganization of outer layers during secretion.<sup>40,73</sup> Based on the observations presented here, the outer layer described in early TEM studies is most likely the crescent phase. As indicated in Figure 33 B, most of the vesicles exhibit a crescent outer phase; however it is not observed any more around coalescing vesicles, suggesting that this phase opens up and releases the other two phases. Consequently, cuticle matrix and granules are most likely composed of the biphasic and surrounding phase of cuticle vesicles.

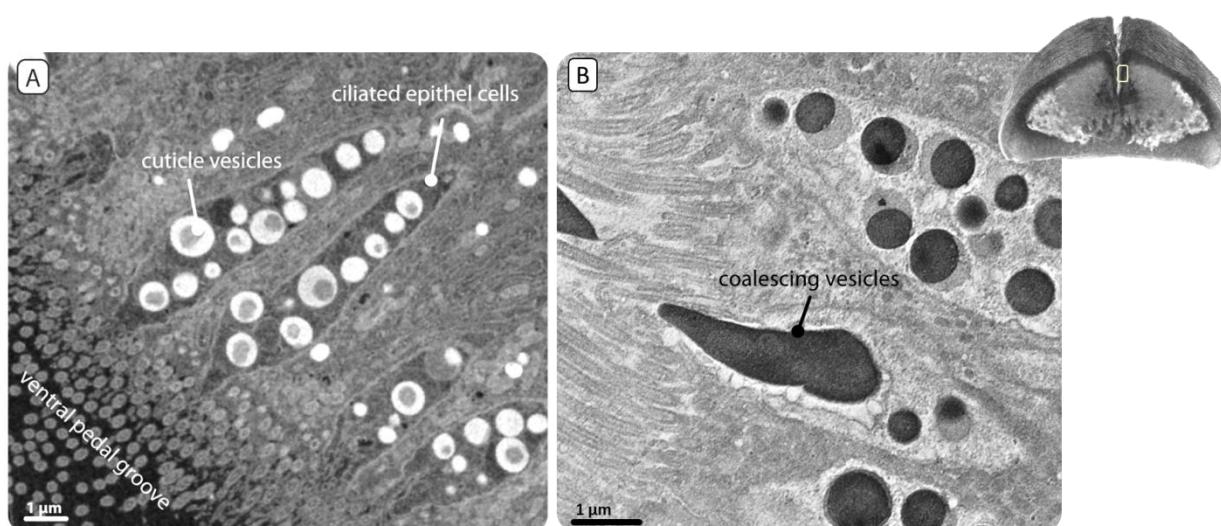


Figure 33. Secretion of cuticle vesicles.

Cuticle vesicles are secreted via ciliated epithelial cells and seem to coalesce right before secretion. A) FIB-SEM BSE image of cuticle vesicle secretion process. Cuticle vesicles are arranged in rows and released into the ventral pedal groove. B) High-resolution TEM image of cuticle vesicles. Some vesicles seem to coalesce right before secretion.

Investigating the cuticle of an induced thread (Figure 32 C) with high-resolution TEM revealed a thin cuticle layer that surrounds the core. In contrast to the highly aligned fibrous core of native threads, the spontaneous assembly of core building blocks results in a disordered morphology (Figure 34 A). At higher magnification, biphasic granules can be observed, which are embedded in a continuous matrix highly reminiscent of the native cuticle structure (Figure 34 B). Based on the observed coalescing of cuticle vesicles during secretion (Figure 33 B), the matrix enclosing the core likely coalesces to form a continuous layer. Figure 34 B shows that the morphology of matrix and granule in the induced cuticle even resembles the secretory vesicle shape in this case (right image half).

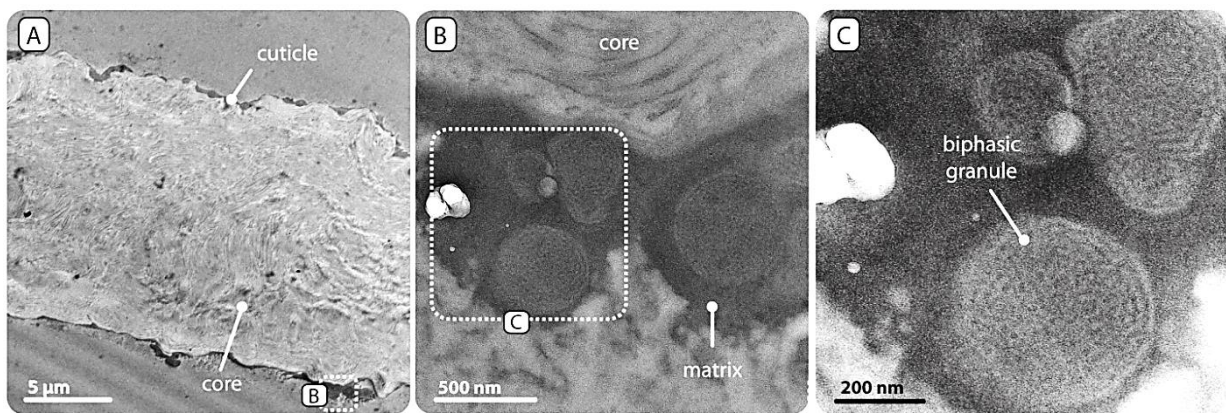


Figure 34. Induced thread shows the ultrastructure of cuticle assembly.

A) TEM image of cross-sectioned induced thread shows the cuticle as thin layer on the fibrous core. B) The biphasic granules and surrounding matrix seem to partially resemble the secretory vesicle shape. C) In contrast to granules observed in native threads, biphasic granules of induced threads are tightly packed.

In contrast to the biphasic granules in mature threads, granules of induced cuticle exhibit a tightly packed structure (Figure 34 C) suggesting either a time-dependent maturation of granule structure or the dependence on biologically regulated mechanical drawing by muscle contraction in the foot. Furthermore, Raman spectroscopy investigations on the induced cuticle demonstrated the absence of metal coordination bonds, which might also impact the structure of induced cuticle granules.<sup>40</sup>

Taken together, the results of the combined investigation of cuticle assembly provide the clear evidence that the two condensed phases observed within the cuticle vesicles - namely the sulfur-rich and sulfur-depleted phase - correspond to the matrix and granules within the mature cuticle, respectively. Furthermore, the results of the elemental analysis indicate that Fe and V are added after cuticle formation, since metals are not observed within the vesicles. Presumably, different metal ions diffuse into the cuticle and partition in different parts, with V concentrating in the granules and Fe concentrating in the matrix.



### 6.3 Discussion

The combined investigations of the synthesis and storage site of cuticle precursors, as well as their secretion and assembly provide an excellent complementation of the previously presented results on cuticle ultrastructure and composition (chapter 5). More than 35 years ago, cuticle tissue vesicles were described as specific membrane-bound subcompartments responsible for the storage of thread cuticle precursors.<sup>73</sup> Within this work, the 3D-structure of cuticle vesicle phases has been shown to be spherical, which is highly reminiscent of multiphase droplet architectures.<sup>147</sup> The spherical shape of condensates in cells has been reported to be dictated by the relative surface tensions among the different possible interfaces.<sup>147</sup> However, why the cuticle vesicles exhibit the observed distinct phases remained elusive. Due to extensive research during the past decades, it is well known that phase separation of macromolecules is largely responsible for cell component organization.<sup>147,148</sup> Although entropy usually keeps a system well mixed, nanoscale interactions between large molecules, such as proteins, can cause demixing. For example, in a system with hydrophilic and hydrophobic molecules, their separation is driven by physical interactions that favor association with like neighbors and disfavor unlike neighbors, resulting in an energy reduction of the system, which opposes mixing of both molecules due to entropy.<sup>148</sup> Mfp-1 was for a long time the only protein that was demonstrated to be present in the byssus cuticle, but enzyme digestion tests in early studies indicated that the vesicle core contains different proteinaceous moieties than the outer layers.<sup>73</sup> While the core was reported to be sensitive to pepsin, the outer layers could be digested with  $\alpha$ -chymotrypsin. Notably, additional cytochemical tests revealed that vesicles consist mainly of strongly reducing groups, such as -SH and phenols.<sup>73</sup> These early studies are highly consistent with recent transcriptomic data and the here presented results on elemental analysis, that suggest the presence of cysteine and DOPA containing proteins in the outer vesicle layers and most probably mfp-1 in the biphasic core structure.<sup>53</sup> Given the fact that mfp-1 and potential cysteine-rich matrix proteins exhibit different biochemical properties regarding their hydrophathy (chapter 5.3), the resulting interaction could drive separation into different phases. Notably, both phases were visible in unstained native threads, whereas the biphasic structure in cuticle vesicles was revealed after post-staining. This suggests that the presence and absence of metal ions, respectively, might contribute to the observed contrast in electron-density.

Along these lines, proteins involved in phase separation of well-studied systems have been reported to often consist of several repeats of specific domains or different types of interaction domains.<sup>147,149</sup> Mfp-1 consists of more than 80 decapeptide repeats (AKPSYPPTYK)<sub>n</sub>, which have not yet been assigned to a specific function.<sup>67</sup> Conceivably, the repetitive domains might be involved in phase separation, but as of yet there exists no experimental evidence for this hypothesis. Along

these lines, aromatic residues have been shown to mediate phase separation via  $\pi$ - $\pi$  stacking interactions and a recombinant version of mfp-1 was demonstrated to undergo coacervation due to cation- $\pi$  interactions *in vitro*.<sup>80,102,147</sup> Cations such as  $\text{Ca}^{2+}$  have been shown to be present in the cuticle by SIMS, but were not observed in cuticle vesicles or the thread cuticle within this study.<sup>72</sup> However, based on the well understood self-assembly of block copolymers into complex architectures, an amphiphilic character of involved components seems likely.<sup>141</sup> Phase-separation in cells mostly results in spherical shapes, which makes the biphasic structure observed in cuticle vesicles particularly interesting.<sup>147</sup> Based on the presented findings, phase separation in cuticle vesicles might involve multiple components and it will require extensive investigation to elucidate the contribution of each component.

Phase-separation requires a critical concentration of involved molecules and it is conceivable that membrane-bound cuticle vesicles could serve as a biological “reaction vessel” for the nucleation of phase separation.<sup>148</sup> Notably, the crescent vesicle phase, which was described as a translucent halo in previous studies, was shown to contain a much lower concentration of nitrogen and presumably protein concentration than the other phases (chapter 6.2.3; Figure 27 C) and is a typical feature of intracellular coacervates.<sup>147</sup> Liquid-liquid phase separation, termed coacervation, usually results in a very dense and in a diluted phase.<sup>80</sup> Conceivably, the observed crescent phase of cuticle vesicles might resemble a diluted phase due to coacervation of matrix proteins. This would fit well to the fact that the two condensed inner phases were shown to assemble into granules and matrix (chapter 6.2.5; Figure 34 B), whereas the third phase presumably is not involved in cuticle formation (chapter 6.2.5; Figure 33 B). Furthermore, the combination of high protein concentration and fluidity observed during the induced thread formation suggests that the vesicle phase containing matrix proteins might be a coacervate.

The ultrastructural observation of the secretion of cuticle vesicles within this thesis showed, that they coalesce prior to secretion, most likely due to contact with the physicochemical properties of the ventral groove, such as higher pH and salt concentration. This result is very consistent with previous observations and suggests a fluid-like behavior which fits well with the hypothesis of tissue vesicles being a liquid-liquid phase-separated architecture.<sup>40</sup> The inner, biphasic structure of cuticle vesicles and induced cuticle are very similar, whereas the spacing between electron-dense phases in mature granules of the native thread was observed to be wider. It is conceivable that mechanical drawing by muscle contraction in the foot might impact the structure of induced cuticle granules, as they have also been shown to be aligned within this work (chapter 5.2.3; Fig. 21 B, C). Furthermore, it was previously demonstrated that DOPA-metal coordination is absent in the induced cuticle, which might affect granule structure and the results of the elemental analysis of cuticle vesicles underpin



the hypothesis that metal ions infiltrate the assembled structures at a later time-point.<sup>40</sup> However, it remains unknown, if specific ion-transporters might be involved in providing the required metal concentrations. Along these lines, it was demonstrated that metal-depleted threads could be reinforced by incubating them in metal solutions demonstrating a passive uptake.<sup>74</sup> However, when native threads were introduced to FeCl<sub>3</sub> enriched seawater, the passive uptake was not measurable, whereas the cuticle of newly produced byssal threads was strongly enriched in Fe, when live mussels were introduced to enriched FeCl<sub>3</sub> water.<sup>69</sup> Furthermore, the absence of iodine in cuticle vesicles is striking, since the matrix of native threads was shown to be specifically enriched in iodine, co-localized with Fe. This result might also suggest that specific transporters might be involved in the enrichment of the byssus cuticle with specific elements. However, further investigations are required to elucidate the role and introduction of different elements detected within cuticle vesicles and mature threads.

The maturation and curing of threads was shown to require biologically regulated steps that are not at play during induced thread formation.<sup>40</sup> The presented ultrastructural details of cuticle self-assembly show the fluid-like coalescing of vesicles and subsequent formation of a solid layer by matrix proteins that enclose the core. This curing process of matrix proteins most likely does not involve metal coordination cross-links, since metal ions were demonstrated to be absent in cuticle vesicles and proposed to infiltrate the cuticle at a later time-point based on a previous study.<sup>40</sup> However, it is conceivable that the formation of disulfide bonds between cysteine-residues or the formation of 5-S-cysteinyl-dopa cross-links of matrix proteins might provide an initial curing of the matrix with a later reinforcement of the cuticle by metal coordination cross-links.

## 6.4 Conclusion

Investigating the ultrastructural details of the rapid cuticle assembly, which occurs hidden from our view, is accompanied by exceptional technical challenges. However, a combination of high-resolution electron microscopy techniques, elemental analysis and 3D-reconstruction provided crucial insights into the production and storage site of cuticle precursors and their secretion. The obtained results allow for the first time to specifically assign the different phases observed in cuticle vesicles to granules and matrix of the thread cuticle, respectively. Moreover, the results of this work strengthen the hypothesis of phase separation contributing to the observed complex ultrastructure of cuticle vesicles and the addition of metal ions at a later time-point. The ultrastructural details of cuticle vesicles during induced thread formation demonstrate that prior coalesced vesicles showing a liquid-like behavior enclose the thread core with a thin layer. Taken together, the combined studies

of the byssus cuticle, its precursors and assembly greatly broadens our understanding of this natural coating and have a high impact on the design of future mussel-inspired coatings.



## 7. REFERENCES

- 1 Fratzl, P. & Weinkamer, R. Nature's Hierarchical Materials. *Prog Mater Sci* 52, 1263-1334, (2007).
- 2 Dunlop, J. W. C. & Fratzl, P. Multilevel Architectures in Natural Materials. *Scr Mater* 68, 8-12, (2013).
- 3 Dunlop, J. W. C. & Fratzl, P. Biological Composites. *Annu Rev Mater Res* 40, 1-24, (2010).
- 4 Fratzl, P. Biomimetic Materials Research: What Can We Really Learn from Nature's Structural Materials? *J R Soc, Interface* 4, 637-642, (2007).
- 5 Fratzl, P. Collagen, Structure and Mechanics. *Springer Science + Business Media, LLC*, (2008).
- 6 Hu, X., Cebe, P., Weiss, A. S., Omenetto, F. & Kaplan, D. L. Protein-Based Composite Materials. *Mater Today* 15, 208-215, (2012).
- 7 Mc Grath, K. & Kaplan, D. Protein-Based Materials. *Birkhäuser Boston*, (1997).
- 8 Gosline, J. M., Guerette, P. A., Ortlepp, C. S. & Savage, K. N. The Mechanical Design of Spider Silks: From Fibroin Sequence to Mechanical Function. *Br J Exp Biol* 202, 3295–3303, (1999).
- 9 Ebrahimi, D., Tokareva, O., Rim, N. G., Wong, J. Y., Kaplan, D. L. & Buehler, M. J. Silk-Its Mysteries, How It Is Made, and How It Is Used. *ACS Biomater Sci Eng* 1, 864-876, (2015).
- 10 Thompson, R. C., Moore, C. J., vom Saal, F. S. & Swan, S. H. Plastics, the Environment and Human Health: Current Consensus and Future Trends. *Philos Trans R Soc Lond B Biol Sci* 364, 2153-2166, (2009).
- 11 Jambeck, J. R., Geyer, R., Wilcox, C., Siegler, T. R., Perryman, M., Andrady, A., Narayan, R. & Law, K. L. Plastic Waste Inputs from Land into the Ocean. *Science* 347, 768-771, (2015).
- 12 Eisoldt, L., Smith, A. & Scheibel, T. Decoding the Secrets of Spider Silk. *Mater Today* 14, 80-86, (2011).
- 13 Rising, A. & Johansson, J. Toward Spinning Artificial Spider Silk. *Nat Chem Biol* 11, 309-315, (2015).
- 14 Rammensee, S., Slotta, U., Scheibel, T. & Bausch, A. R. Assembly Mechanism of Recombinant Spider Silk Proteins. *PNAS* 105, 6590–6595, (2008).
- 15 Krogsgaard, M., Nue, V. & Birkedal, H. Mussel-Inspired Materials: Self-Healing through Coordination Chemistry. *Chemistry* 22, 844-857, (2016).
- 16 Lee, B. P., Messersmith, P. B., Israelachvili, J. N. & Waite, J. H. Mussel-Inspired Adhesives and Coatings. *Annu Rev Mater Res* 41, 99-132, (2011).
- 17 Harrington, M. J. & Waite, J. H. Holdfast Heroics: Comparing the Molecular and Mechanical Properties of *Mytilus californianus* Byssal Threads. *J Exp Biol* 210, 4307-4318, (2007).
- 18 Carrington, E., Waite, J. H., Sara, G. & Sebens, K. P. Mussels as a Model System for Integrative Ecomechanics. *Ann Rev Mar Sci* 7, 443-469, (2015).
- 19 Harrington, M. J., Jehle, F. & Priemel, T. Mussel Byssus Structure-Function and Fabrication as Inspiration for Biotechnological Production of Advanced Materials. *Biotechnol J*, e1800133, (2018).
- 20 Waite, J. H. Mussel Adhesion - Essential Footwork. *J Exp Biol* 220, 517-530, (2017).
- 21 Waite, J. H., Qin, X. & Coyne, K. The Peculiar Collagens of Mussel Byssus. *Matrix Biol* 17, 93-106, (1998).
- 22 Krauss, S., Metzger, T. H., Fratzl, P. & Harrington, M. J. Self-Repair of a Biological Fiber Guided by an Ordered Elastic Framework. *Biomacromolecules* 14, 1520-1528, (2013).
- 23 Schmitt, C. N., Politi, Y., Reinecke, A. & Harrington, M. J. Role of Sacrificial Protein-Metal Bond Exchange in Mussel Byssal Thread Self-Healing. *Biomacromolecules* 16, 2852-2861, (2015).

- 24 Reinecke, A., Bertinetti, L., Fratzl, P. & Harrington, M. J. Cooperative Behavior of a Sacrificial Bond Network and Elastic Framework in Providing Self-Healing Capacity in Mussel Byssal Threads. *J Struct Biol* 196, 329-339, (2016).
- 25 Harrington, M. J., Masic, A., Holten-Andersen, N., Waite, J. H. & Fratzl, P. Iron-Clad Fibers: A Metal-Based Biological Strategy for Hard Flexible Coatings. *Science* 328, 216-220, (2010).
- 26 Li, L., Smitthipong, W. & Zeng, H. Mussel-Inspired Hydrogels for Biomedical and Environmental Applications. *Polym Chem* 6, 353-358, (2015).
- 27 Fullenkamp, D. E., He, L., Barrett, D. G., Burghardt, W. R. & Messersmith, P. B. Mussel-Inspired Histidine-Based Transient Network Metal Coordination Hydrogels. *Macromolecules* 46, 1167-1174, (2013).
- 28 Holten-Andersen, N., Harrington, M. J., Birkedal, H., Lee, B. P., Messersmith, P. B., Lee, K. Y. & Waite, J. H. PH-Induced Metal-Ligand Cross-Links Inspired by Mussel Yield Self-Healing Polymer Networks with near-Covalent Elastic Moduli. *PNAS* 108, 2651-2655, (2011).
- 29 Grindy, S. C. & Holten-Andersen, N. Bio-Inspired Metal-Coordinate Hydrogels with Programmable Viscoelastic Material Functions Controlled by Longwave Uv Light. *Soft Matter* 13, 4057-4065, (2017).
- 30 Enke, M., Jehle, F., Bode, S., Vitz, J., Harrington, M. J., Hager, M. D. & Schubert, U. S. Histidine-Zinc Interactions Investigated by Isothermal Titration Calorimetry (ITC) and Their Application in Self-Healing Polymers. *Macromol Chem Phys* 218, (2017).
- 31 Degtyar, E., Harrington, M. J., Politi, Y. & Fratzl, P. Die Bedeutung Von Metallionen Für Die Mechanischen Eigenschaften Von Biomaterialien Auf Proteinbasis. *Angew Chem* 126, 12220-12240, (2014).
- 32 Grindy, S. C., Learsch, R., Mozhdehi, D., Cheng, J., Barrett, D. G., Guan, Z., Messersmith, P. B. & Holten-Andersen, N. Control of Hierarchical Polymer Mechanics with Bioinspired Metal-Coordination Dynamics. *Nat Mater* 14, 1210-1216, (2015).
- 33 Kim, B. J., Oh, D. X., Kim, S., Seo, J. H., Hwang, D. S., Masic, A., Han, D. K. & Cha, H. J. Mussel-Mimetic Protein-Based Adhesive Hydrogel. *Biomacromolecules* 15, 1579-1585, (2014).
- 34 Golser, Adrian V. & Scheibel, T. Biotechnological Production of the Mussel Byssus Derived Collagen preCol-D. *RSC Advances* 7, 38273-38278, (2017).
- 35 Wang, J. & Scheibel, T. Recombinant Production of Mussel Byssus Inspired Proteins. *Biotechnol J*, e1800146, (2018).
- 36 Harrington, M. J. & Waite, J. H. How Nature Modulates a Fiber's Mechanical Properties: Mechanically Distinct Fibers Drawn from Natural Mesogenic Block Copolymer Variants. *Adv Mater* 21, 440-444, (2009).
- 37 Harrington, M. J. & Waite, J. H. Ph-Dependent Locking of Giant Mesogens in Fibers Drawn from Mussel Byssal Collagens. *Biomacromolecules* 9, 1480-1486, (2008).
- 38 Kim, B. J., Choi, Y. S. & Cha, H. J. Reinforced Multifunctionalized Nanofibrous Scaffolds Using Mussel Adhesive Proteins. *Angew Chem Int Ed Engl* 51, 675-678, (2012).
- 39 Lu, Q., Danner, E., Waite, J. H., Israelachvili, J. N., Zeng, H. & Hwang, D. S. Adhesion of Mussel Foot Proteins to Different Substrate Surfaces. *J R Soc Interface* 10, 20120759, (2013).
- 40 Priemel, T., Degtyar, E., Dean, M. N. & Harrington, M. J. Rapid Self-Assembly of Complex Biomolecular Architectures During Mussel Byssus Biofabrication. *Nat Commun* 8, 14539, (2017).
- 41 Waite, J. H. The Formation of Mussel Byssus: Anatomy of a Natural Manufacturing Process. *Results Probl. Cell Differ.* 19, 27-54, (1992).
- 42 Holten-Andersen, N., Fantner, G. E., Hohlbauch, S., Waite, J. H. & Zok, F. W. Protective Coatings on Extensible Biofibres. *Nat Mater* 6, 669-672, (2007).
- 43 Stewart, R. J., Weaver, J. C., Morse, D. E. & Waite, J. H. The Tube Cement of Phragmatopoma Californica: A Solid Foam. *J Exp Biol* 207, 4727-4734, (2004).



## REFERENCES

- 44 Hennebert, E., Wattiez, R., Demeuldre, M., Ladurner, P., Hwang, D. S., Waite, J. H. & Flammang, P. Sea Star Tenacity Mediated by a Protein That Fragments, Then Aggregates. *PNAS* 111, 6317-6322, (2014).
- 45 Petrone, L., Kumar, A., Sutanto, C. N., Patil, N. J., Kannan, S., Palaniappan, A., Amini, S., Zappone, B., Verma, C. & Miserez, A. Mussel Adhesion Is Dictated by Time-Regulated Secretion and Molecular Conformation of Mussel Adhesive Proteins. *Nat Commun* 6, 8737, (2015).
- 46 Yu, J., Wei, W., Danner, E., Ashley, R. K., Israelachvili, J. N. & Waite, J. H. Mussel Protein Adhesion Depends on Interprotein Thiol-Mediated Redox Modulation. *Nat Chem Biol* 7, 588-590, (2011).
- 47 Lim, S., Choi, Y. S., Kang, D. G., Song, Y. H. & Cha, H. J. The Adhesive Properties of Coacervated Recombinant Hybrid Mussel Adhesive Proteins. *Biomaterials* 31, 3715-3722, (2010).
- 48 Wei, W., Petrone, L., Tan, Y., Cai, H., Israelachvili, J. N., Miserez, A. & Waite, J. H. An Underwater Surface-Drying Peptide Inspired by a Mussel Adhesive Protein. *Adv Funct Mater* 26, 3496-3507, (2016).
- 49 Maier, G. P., Rapp, M. V., Waite, J. H., Israelachvili, J. N. & Butler, A. Adaptive Synergy between Catechol and Lysine Promotes Wet Adhesion by Surface Salt Displacement. *Science* 349, 628-632, (2015).
- 50 Gebbie, M. A., Wei, W., Schrader, A. M., Cristiani, T. R., Dobbs, H. A., Idso, M., Chmelka, B. F., Waite, J. H. & Israelachvili, J. N. Tuning Underwater Adhesion with Cation- $\pi$  Interactions. *Nat Chem* 9, 473-479, (2017).
- 51 Hwang, D. S., Zeng, H., Masic, A., Harrington, M. J., Israelachvili, J. N. & Waite, J. H. Protein- and Metal-Dependent Interactions of a Prominent Protein in Mussel Adhesive Plaques. *J Biol Chem* 285, 25850-25858, (2010).
- 52 Zhao, H. & Waite, J. H. Proteins in Load-Bearing Junctions: The Histidine-Rich Metal-Binding Protein of Mussel Byssus. *Biochemistry* 45, 14223-14231, (2006).
- 53 DeMartini, D. G., Errico, J. M., Sjoestroem, S., Fenster, A. & Waite, J. H. A Cohort of New Adhesive Proteins Identified from Transcriptomic Analysis of Mussel Foot Glands. *J R Soc Interface* 14, (2017).
- 54 Waite J. H. , V. E., Sun C. and Lucas J. M. Elastomeric Gradients: A Hedge against Stress Concentration in Marine Holdfasts? *Phil. Trans. R. Soc. Lond. B* 357, 143–153, (2002).
- 55 Mercer, E. H. Observations on the Molecular Structure of Byssus Fibres. *Aust. J. Mar. Freshw. Res.* 3, 199-205, (1952).
- 56 Qin, X. & Waite, J. H. Exotic Collagen Gradients in the Byssus of the Mussel *Mytilus edulis*. *Br J Exp Biol* 198, 633–644, (1995).
- 57 Carrington, E. & Gosline, J. M. Mechanical Design of Mussel Byssus: Load Cycle and Strain Rate Dependence. *American Malacological Bulletin* 18, 135-142, (2004).
- 58 Waite, J. H., Lichtenegger, H. C., Stucky, D. G. & Hansma, P. Exploring Molecular and Mechanical Gradients in Structural Bioscaffolds. *Biochemistry* 43, 7653–7662, (2004).
- 59 Vaccaro, E. & Waite, J. H. Yield and Post-Yield Behavior of Mussel Byssal Thread: A Self-Healing Biomolecular Material. *Biomacromolecules* 2, 906-911, (2001).
- 60 Sagert, J. & Waite, J. H. Hyperunstable Matrix Proteins in the Byssus of *Mytilus galloprovincialis*. *J Exp Biol* 212, 2224-2236, (2009).
- 61 Suhre, M. H., Gertz, M., Steegborn, C. & Scheibel, T. Structural and Functional Features of a Collagen-Binding Matrix Protein from the Mussel Byssus. *Nat Commun* 5, 3392, (2014).
- 62 Sun, C., Lucas, J. M. & Waite, J. H. Collagen-Binding Matrix Proteins from Elastomeric Extraorganismic Byssal Fibers. *Biomacromolecules* 3, 1240-1248, (2002).
- 63 Harrington, M. J., Gupta, H. S., Fratzl, P. & Waite, J. H. Collagen Insulated from Tensile Damage by Domains That Unfold Reversibly: In Situ X-Ray Investigation of Mechanical Yield and Damage Repair in the Mussel Byssus. *J Struct Biol* 167, 47-54, (2009).

- 64 Hagenau, A., Papadopoulos, P., Kremer, F. & Scheibel, T. Mussel Collagen Molecules with Silk-Like Domains as Load-Bearing Elements in Distal Byssal Threads. *J Struct Biol* 175, 339-347, (2011).
- 65 Arnold, A. A., Byette, F., Seguin-Heine, M. O., Leblanc, A., Sleno, L., Tremblay, R., Pellerin, C. & Marcotte, I. Solid-State NMR Structure Determination of Whole Anchoring Threads from the Blue Mussel *Mytilus edulis*. *Biomacromolecules* 14, 132-141, (2013).
- 66 Holten-Andersen, N., Zhao, H. & Waite, J. H. Stiff Coatings on Compliant Biofibers: The Cuticle of *Mytilus californianus* Byssal Threads. *Biochemistry* 48, 2752–2759, (2009).
- 67 Hwang, D. S. & Waite, J. H. Three Intrinsically Unstructured Mussel Adhesive Proteins, Mfp-1, Mfp-2, and Mfp-3: Analysis by Circular Dichroism. *Protein Sci* 21, 1689-1695, (2012).
- 68 Holten-Andersen, N. & Waite, J. H. Mussel-Designed Protective Coatings for Compliant Substrates. *J Dent Res* 87, 701-709, (2008).
- 69 Sun, C. & Waite, J. H. Mapping Chemical Gradients within and Along a Fibrous Structural Tissue, Mussel Byssal Threads. *J Biol Chem* 280, 39332-39336, (2005).
- 70 Monnier, C. A., DeMartini, D. G. & Waite, J. H. Intertidal Exposure Favors the Soft-Studded Armor of Adaptive Mussel Coatings. *Nat Commun* 9, 3424, (2018).
- 71 He, Y., Sun, C., Jiang, F., Yang, B., Li, J., Zhong, C., Zheng, L. & Ding, H. Lipids as Integral Components in Mussel Adhesion. *Soft Matter* 14, 7145-7154, (2018).
- 72 Holten-Andersen, N., Mates, T. E., Toprak, M. S., Stucky, G. D., Zok, F. W. & Waite, J. H. Metals and the Integrity of a Biological Coating: The Cuticle of Mussel Byssus. *Langmuir* 25, 3323-3326, (2009).
- 73 Vitellaro Zuccarello, L. Ultrastructural and Cytochemical Study on the Enzyme Gland of the Foot of a Mollusc. *Tissue & Cell* 13, 701-713, (1981).
- 74 Schmitt, C. N., Winter, A., Bertinetti, L., Masic, A., Strauch, P. & Harrington, M. J. Mechanical Homeostasis of a Dopa-Enriched Biological Coating from Mussels in Response to Metal Variation. *J R Soc Interface* 12, 0466, (2015).
- 75 Tamarin, A. & Keller, P. J. An Ultrastructural Study of the Byssal Thread Forming System in *Mytilus*. *J Ultrastruct Res* 40, 401-416, (1972).
- 76 Inoue, K., Takeuchi, Y., Miki, D., Odo, S., Harayama, S. & Waite, J. H. Cloning, Sequencing and Sites of Expression of Genes for the Hydroxy Arginine-Containing Adhesive-Plaques Protein of the Mussel *Mytilus galloprovincialis*. *Eur J Biochem* 239, (1996).
- 77 Miki, D., Takeuchi, Y., Inoue, K. & Odo, S. Expression Sites of Two Byssal Protein Genes of *Mytilus galloprovincialis*. *Biol Bull* 190, 213-217, (1996).
- 78 Hwang, D. S., Zeng, H., Srivastava, A., Krogstad, D. V., Tirrell, M., Israelachvili, J. N. & Waite, J. H. Viscosity and Interfacial Properties in a Mussel-Inspired Adhesive Coacervate. *Soft Matter* 6, 3232-3236, (2010).
- 79 Wei, W., Tan, Y., Martinez Rodriguez, N. R., Yu, J., Israelachvili, J. N. & Waite, J. H. A Mussel-Derived One Component Adhesive Coacervate. *Acta Biomater* 10, 1663-1670, (2014).
- 80 Kim, S., Yoo, H. Y., Huang, J., Lee, Y., Park, S., Park, Y., Jin, S., Jung, Y. M., Zeng, H., Hwang, D. S. & Jho, Y. Salt Triggers the Simple Coacervation of an Underwater Adhesive When Cations Meet Aromatic Pi Electrons in Seawater. *ACS Nano* 11, 6764-6772, (2017).
- 81 Vitellaro Zuccarello, L. The Collagen Gland of *Mytilus galloprovincialis*: An Ultrastructural and Cytochemical Study on Secretory Granules. *J Ultrastruct Res* 73, 135-147, (1980).
- 82 Hassenkam, T., Gutschmann, T., Hansma, P., Sagert, J. & Waite, J. H. Giant Bent-Core Mesogens in the Thread Forming Process of Marine Mussels. *Biomacromolecules* 5, 1351-1355, (2004).
- 83 Reinecke, A., Brezesinski, G. & Harrington, M. J. Ph-Responsive Self-Organization of Metal-Binding Protein Motifs from Biomolecular Junctions in Mussel Byssus. *Adv Mater Interfaces* 4, (2017).
- 84 Pujol, J. P. Formation of the Byssus in the Common Mussel (*Mytilus edulis* L.). *Nature* 214, 204-205, (1967).



## REFERENCES

- 85 Tamarin, A., Lewis, P. & Askey, J. The Structure and Formation of the Byssus Attachment Plaque in *Mytilus*. *J Morphol* 149, 199-222, (1976).
- 86 Inoue, K., Takeuchi, Y., Miki, D. & Odo, S. Mussel Adhesive Plaque Protein Gene Is a Novel Member of Epidermal Growth Factor-Like Gene Family. *J Biol Chem* 270, 6698-6701, (1995).
- 87 Papov, V. V., Diamond, T. V., Biemann, K. & Waite, J. H. Hydroxyarginine-Containing Polyphenolic Proteins in the Adhesive Plaque of the Marine Mussel *Mytilus edulis*. *J Biol Chem* 270, 20183-20192, (1995).
- 88 Waite, J. H. & Qin, X. Polyphosphoprotein from the Adhesive Pads of *Mytilus edulis*. *Biochemistry* 40, 2887-2893, (2001).
- 89 Zhao, H. & Waite, J. H. Linking Adhesive and Structural Proteins in the Attachment Plaque of *Mytilus californianus*. *J Biol Chem* 281, 26150-26158, (2006).
- 90 Qin, X., Coyne, K. J. & H., W. J. Tough Tendons: Mussel Byssus Has Collagen with Silk-Like Domains. *J Biol Chem* 272, 32623-32627, (1997).
- 91 Benedict, C. V. & Waite, J. H. Location and Analysis of Byssal Structural Proteins of *Mytilus edulis*. *J Morphol* 189, 171-181, (1986).
- 92 Narayan, K. & Subramaniam, S. Focused Ion Beams in Biology. *Nat Methods* 12, 1021-1031, (2015).
- 93 Burette, F., Pellerin, C. & Marcotte, I. Self-Assembled Ph-Responsive Films Prepared from Mussel Anchoring Threads. *J Mater Chem* 2, (2014).
- 94 Montroni, D., Piccinetti, C., Fermani, S., Calvaresi, M., Harrington, M. J. & Falini, G. Exploitation of Mussel Byssus Mariculture Waste as a Water Remediation Material. *RSC Advances* 7, 36605-36611, (2017).
- 95 Montroni, D., Valle, F., Rapino, S., Fermani, S., Calvaresi, M., Harrington, M. J. & Falini, G. Functional Biocompatible Matrices from Mussel Byssus Waste. *ACS Biomater Sci Eng* 4, 57-65, (2017).
- 96 Burette, F., Laventure, A., Marcotte, I. & Pellerin, C. Metal-Ligand Interactions and Salt Bridges as Sacrificial Bonds in Mussel Byssus-Derived Materials. *Biomacromolecules* 17, 3277-3286, (2016).
- 97 Strausberg, R. L., Anderson, D. M., Filpula, D., Finkelman, M., Link, R., McCandliss, R., Orndorff, S. A., Strausberg, S. L. & Wei, T. in *Adhesives from Renewable Resources Acs Symposium Series* 453-464 (1989).
- 98 Yoo, H. Y., Song, Y. H., Foo, M., Seo, E., Hwang, D. S. & Seo, J. H. Recombinant Mussel Proximal Thread Matrix Protein Promotes Osteoblast Cell Adhesion and Proliferation. *BMC Biotechnol* 16, 16, (2016).
- 99 Lee, H., Scherer, N. F. & Messersmith, P. B. Single-Molecule Mechanics of Mussel Adhesion. *PNAS* 103, 12999-13003, (2006).
- 100 Kim, B. J., Cheong, H., Hwang, B. H. & Cha, H. J. Mussel-Inspired Protein Nanoparticles Containing Iron(III)-Dopa Complexes for Ph-Responsive Drug Delivery. *Angew Chem Int Ed Engl* 54, 7318-7322, (2015).
- 101 Zeng, H., Hwang, D. S., Israelachvili, J. N. & Waite, J. H. Strong Reversible Fe<sup>3+</sup>-Mediated Bridging between Dopa-Containing Protein Films in Water. *PNAS* 107, 12850-12853, (2010).
- 102 Kim, S., Huang, J., Lee, Y., Dutta, S., Yoo, H. Y., Jung, Y. M., Jho, Y., Zeng, H. & Hwang, D. S. Complexation and Coacervation of Like-Charged Polyelectrolytes Inspired by Mussels. *PNAS* 113, E847-853, (2016).
- 103 Hwang, D. S., Gim, Y., Kang, D. G., Kim, Y. K. & Cha, H. J. Recombinant Mussel Adhesive Protein Mgfp-5 as Cell Adhesion Biomaterial. *J Biotechnol* 127, 727-735, (2007).
- 104 Kim, C. S., Choi, Y. S., Ko, W., Seo, J. H., Lee, J. & Cha, H. J. A Mussel Adhesive Protein Fused with the Bc Domain of Protein A Is a Functional Linker Material That Efficiently Immobilizes Antibodies onto Diverse Surfaces. *Adv Funct Mater* 21, 4101-4108, (2011).

- 105 Choi, B.-H., Cheong, H., Jo, Y. K., Bahn, S. Y., Seo, J. H. & Cha, H. J. Highly Purified Mussel Adhesive Protein to Secure Biosafety for in Vivo Applications. *Microb Cell Fact* 13, 1-12, (2014).
- 106 Hwang, D. S., Gim, Y., Yoo, H. J. & Cha, H. J. Practical Recombinant Hybrid Mussel Bioadhesive Fp-151. *Biomaterials* 28, 3560-3568, (2007).
- 107 Hwang, D. S., Sim, S. B. & Cha, H. J. Cell Adhesion Biomaterial Based on Mussel Adhesive Protein Fused with Rgd Peptide. *Biomaterials* 28, 4039-4046, (2007).
- 108 Choi, B. H., Choi, Y. S., Kang, D. G., Kim, B. J., Song, Y. H. & Cha, H. J. Cell Behavior on Extracellular Matrix Mimic Materials Based on Mussel Adhesive Protein Fused with Functional Peptides. *Biomaterials* 31, 8980-8988, (2010).
- 109 Yang, B., Ayyadurai, N., Yun, H., Choi, Y. S., Hwang, B. H., Huang, J., Lu, Q., Zeng, H. & Cha, H. J. In Vivo Residue-Specific Dopa-Incorporated Engineered Mussel Bioglue with Enhanced Adhesion and Water Resistance. *Angew Chem Int Ed Engl* 53, 13360-13364, (2014).
- 110 Wei, W., Yu, J., Gebbie, M. A., Tan, Y., Martinez Rodriguez, N. R., Israelachvili, J. N. & Waite, J. H. Bridging Adhesion of Mussel-Inspired Peptides: Role of Charge, Chain Length, and Surface Type. *Langmuir* 31, 1105-1112, (2015).
- 111 Schmidt, S., Reinecke, A., Wojcik, F., Pussak, D., Hartmann, L. & Harrington, M. J. Metal-Mediated Molecular Self-Healing in Histidine-Rich Mussel Peptides. *Biomacromolecules* 15, 1644-1652, (2014).
- 112 Trapaidze, A., D'Antuono, M., Fratzi, P. & Harrington, M. J. Exploring Mussel Byssus Fabrication with Peptide-Polymer Hybrids: Role of Ph and Metal Coordination in Self-Assembly and Mechanics of Histidine-Rich Domains. *Eur Polym J* 109, 229-236, (2018).
- 113 Jehle, F., Fratzi, P. & Harrington, M. J. Metal-Tunable Self-Assembly of Hierarchical Structure in Mussel-Inspired Peptide Films. *ACS Nano* 12, 2160-2168, (2018).
- 114 Hammersley, A. P. Fit2d: A Multi-Purpose Data Reduction, Analysis and Visualization Program. *J Appl Cryst* 49, 646-652, (2016).
- 115 Barth, A. Infrared Spectroscopy of Proteins. *Biochim Biophys Acta* 1767, 1073-1101, (2007).
- 116 Shivu, B., Seshadri, S., Li, J., Oberg, K. A., Uversky, V. N. & Fink, A. L. Distinct Beta-Sheet Structure in Protein Aggregates Determined by Atr-Ftir Spectroscopy. *Biochemistry* 52, 5176-5183, (2013).
- 117 Rousseau, M.-E., Lefèvre, T., Beaulieu, L., Asakura, T. & Pérolet, M. Study of Protein Conformation and Orientation in Silkworm and Spider Silk Fibers Using Raman Microspectroscopy. *Biomacromolecules* 5, 2247-2257, (2004).
- 118 Takeuchi, H. Raman Structural Markers of Tryptophan and Histidine Side Chains in Proteins. *Biopolymers* 72, 305-317, (2003).
- 119 Frankaer, C. G., Knudsen, M. V., Noren, K., Nazarenko, E., Stahl, K. & Harris, P. The Structures of T6, T3r3 and R6 Bovine Insulin: Combining X-Ray Diffraction and Absorption Spectroscopy. *Acta Cryst* 68, 1259-1271, (2012).
- 120 Jahn, T. R., Makin, O. S., Morris, K. L., Marshall, K. E., Tian, P., Sikorski, P. & Serpell, L. C. The Common Architecture of Cross-Beta Amyloid. *J Mol Biol* 395, 717-727, (2010).
- 121 Weisman, S., Okada, S., Mudie, S. T., Huson, M. G., Trueman, H. E., Sriskantha, A., Haritos, V. S. & Sutherland, T. D. Fifty Years Later: The Sequence, Structure and Function of Lacewing Cross-Beta Silk. *J Struct Biol* 168, 467-475, (2009).
- 122 Sampath, S., Isdebski, T., Jenkins, J. E., Ayon, J. V., Henning, R. W., Orgel, J. P., Antipoa, O. & Yarger, J. L. X-Ray Diffraction Study of Nanocrystalline and Amorphous Structure within Major and Minor Ampullate Dragline Spider Silks. *Soft Matter* 8, 6713-6722, (2012).
- 123 Fu, J., Guerette, P. A., Pavesi, A., Horbelt, N., Lim, C. T., Harrington, M. J. & Miserez, A. Artificial Hagfish Protein Fibers with Ultra-High and Tunable Stiffness. *Nanoscale* 9, 12908-12915, (2017).
- 124 Inouye, H., Sharma, D., Goux, W. J. & Kirschner, D. A. Structure of Core Domain of Fibril-Forming Phf/Tau Fragments. *Biophys J* 90, 1774-1789, (2006).



## REFERENCES

- 125 Ling, S., Li, C., Adamcik, J., Shao, Z., Chen, X. & Mezzenga, R. Modulating Materials by Orthogonally Oriented Beta-Strands: Composites of Amyloid and Silk Fibroin Fibrils. *Adv Mater* 26, 4569-4574, (2014).
- 126 Knowles, T. P., Oppenheim, T. W., Buell, A. K., Chirgadze, D. Y. & Welland, M. E. Nanostructured Films from Hierarchical Self-Assembly of Amyloidogenic Proteins. *Nat Nanotechnol* 5, 204-207, (2010).
- 127 Alies, B., Pradines, V., Llorens-Alliot, I., Sayen, S., Guillon, E., Hureau, C. & Faller, P. Zinc(II) Modulates Specifically Amyloid Formation and Structure in Model Peptides. *J Biol Inorg Chem* 16, 333-340, (2011).
- 128 Sviben, S., Gal, A., Hood, M. A., Bertinetti, L., Politi, Y., Bennet, M., Krishnamoorthy, P., Schertel, A., Wirth, R., Sorrentino, A., Pereiro, E., Faivre, D. & Scheffel, A. A Vacuole-Like Compartment Concentrates a Disordered Calcium Phase in a Key Coccolithophorid Alga. *Nat Commun* 7, 11228, (2016).
- 129 Zlotnikov, I., Zolotoyabko, E. & Fratzl, P. Nano-Scale Modulus Mapping of Biological Composite Materials: Theory and Practice. *Prog Mater Sci* 87, 292-320, (2017).
- 130 Panossian, R., Terzian, G. & Guiliano, M. Coordination Iron-Cysteine and Methylcysteine Complexes. *Spectrosc Lett* 12, 715-723, (2006).
- 131 Girvan, H. M., Bradley, J. M., Cheesman, M. R., Kincaid, J. R., Liu, Y., Czarnecki, K., Fisher, K., Leys, D., Rigby, S. E. & Munro, A. W. Analysis of Heme Iron Coordination in Dgcr8: The Heme-Binding Component of the Microprocessor Complex. *Biochemistry* 55, 5073-5083, (2016).
- 132 Smith, A. T., Pazicni, S., Marvin, K. A., Stevens, D. J., Paulsen, K. M. & Burstyn, J. N. Functional Divergence of Heme-Thiolate Proteins: A Classification Based on Spectroscopic Attributes. *Chem Rev* 115, 2532-2558, (2015).
- 133 Venkataraman, D., Du, Y., Wilson, S. R., Hirsch, K. A., Zhang, P. & Moore, J. S. A Coordination Geometry Table of the D-Block Elements and Their Ions. *J Chem Educ* 74, 915-918, (1997).
- 134 Politi, Y., Priewasser, M., Pippel, E., Zaslansky, P., Hartmann, J., Siegel, S., Li, C., Barth, F. G. & Fratzl, P. A Spider's Fang: How to Design an Injection Needle Using Chitin-Based Composite Material. *Adv Funct Mater* 22, 2519-2528, (2012).
- 135 Gribble, G. W. Naturally Occurring Organohalogen Compounds - a Survey. *J Nat Prod* 55, 1353-1395, (1992).
- 136 Sun, C. J., Srivastava, A., Reifert, J. R. & Waite, J. H. Halogenated Dopa in a Marine Adhesive Protein. *J Adhes* 85, 126, (2009).
- 137 Lichtenegger, H. C., Schöberl, T., Ruokolainen, J. T., Cross, J. O., Heald, S. M., Birkedal, H., Waite, J. H. & Stucky, G. D. Zinc and Mechanical Prowess in the Jaws of Nereis, a Marine Worm. *PNAS* 100, 9144-9149, (2003).
- 138 Birkedal, H., Khan, R. K., Slack, N., Broomell, C., Lichtenegger, H. C., Zok, F., Stucky, G. D. & Waite, J. H. Halogenated Veneers: Protein Cross-Linking and Halogenation in the Jaws of Nereis, a Marine Polychaete Worm. *ChemBiochem* 7, 1392-1399, (2006).
- 139 Haemers, S., Koper, G. J. M. & Frens, G. Effect of Oxidation Rate on Cross-Linking of Mussel Adhesive Proteins. *Biomacromolecules* 4, 632-640, (2003).
- 140 Haemers, S., van der Leeden, M. C. & Frens, G. Coil Dimensions of the Mussel Adhesive Protein Mefp-1. *Biomaterials* 26, 1231-1236, (2005).
- 141 Deng, Y., Wei, J., Sun, Z. & Zhao, D. Large-Pore Ordered Mesoporous Materials Templated from Non-Pluronic Amphiphilic Block Copolymers. *Chem Soc Rev* 42, 4054-4070, (2013).
- 142 Kopeck, B. G., Paez-Segala, M. G., Shtengel, G., Sochacki, K. A., Sun, M. G., Wang, Y., Xu, C. S., van Engelenburg, S. B., Taraska, J. W., Looger, L. L. & Hess, H. F. Diverse Protocols for Correlative Super-Resolution Fluorescence Imaging and Electron Microscopy of Chemically Fixed Samples. *Nat Protoc* 12, 916-946, (2017).
- 143 Hayat, M. A. Principles and Techniques of Electron Microscopy. *Cambridge University Press*, (2000).

- 144 McDonald, K. L. A Review of High-Pressure Freezing Preparation Techniques for Correlative Light and Electron Microscopy of the Same Cells and Tissues. *J Microsc* 235, 273-281, (2009).
- 145 Kaech, A. & Ziegler, U. High-Pressure Freezing: Current State and Future Prospects. *Springer*, (2014).
- 146 Filippidi, E., DeMartini, D. G., Malo de Molina, P., Danner, E. W., Kim, J., Helgeson, M. E., Waite, J. H. & Valentine, M. T. The Microscopic Network Structure of Mussel (*Mytilus*) Adhesive Plaques. *J R Soc Interface* 12, 20150827, (2015).
- 147 Shin, Y. & Brangwynne, C. P. Liquid Phase Condensation in Cell Physiology and Disease. *Science* 357, (2017).
- 148 Hyman, A. A., Weber, C. A. & Julicher, F. Liquid-Liquid Phase Separation in Biology. *Annu Rev Cell Dev Biol* 30, 39-58, (2014).
- 149 Pawson, T. & Nash, P. Assembly of Cell Regulatory Systems through Protein Interaction Domains. *Science* 300, 445-452, (2003).



## **8. DECLARATION OF ORIGINALITY / EIDESSTÄTTLICHE ERKLÄRUNG**

I hereby declare, that this thesis work “Tracking Self-assembly of Hierarchically Structured Soft Matter” is my own work and that only the denoted resources were used. In this or similar form this thesis work has not been submitted for the award of any other degree.

Hiermit erkläre ich, dass ich die vorliegende Arbeit zum Thema „Tracking Self-assembly of Hierarchically Structured Soft Matter“ selbständig und unter ausschließlicher Verwendung der angegebenen Literatur und Hilfsmittel erstellt habe. Die Arbeit ist bisher an keiner anderen Hochschule eingereicht worden.

Franziska Jehle

Potsdam-Golm, 28.01.2019

## 9. ACKNOWLEDGEMENTS

When thinking about the past 3.5 years, I feel above all very grateful to have had two fantastic supervisors – Matt Harrington and Luca Bertinetti. I could immediately sense Matt's enthusiasm and curiosity for science when we first met and although this research topic felt to be way out of my comfort zone at first, it fascinates me ever since. This work was possible not least because of the trust Matt put in me and my abilities and his help in any way possible. Although he left the institute 1.5 years ago to start a new position in Canada, he made time for regular skype calls and discussions whenever needed. When Matt left the institute, Luca adopted me as official member of his group and introduced me into the world of FIB-SEM. Besides being an excellent scientist, Luca is a very empathic and caring mentor, who gives great advice and feedback. Working with him is great fun and I appreciate the countless hours he spent with me in front of my samples and data. Thank you so much Matt and Luca for everything you taught me about science - and life!

I also want to thank Robert Seckler, who accepted me as his PhD student and who always was friendly and open for discussions about my research topic. My work at the institute clearly benefited from the great atmosphere in our department. Peter Fratzl makes the Biomaterials department a great place to work and to further develop knowledge and expertise. I enjoyed our numerous discussions about my project, which I never left without learning something new. During the past years, I met numerous wonderful colleagues and friends - I would especially like to thank Jeannette Steffen and Tobias Priemel for their constant support. Without the great expertise of Sanja Sviben and Elena Macías-Sánchez, the sample preparation for FIB-SEM and TEM would not have been possible. I would also like to thank Kerstin Blank for helpful discussions and Igor Zlotnikov for inviting me to Dresden to test my samples.

I wouldn't be here if it wasn't for my wonderful family and friends. I want to thank my parents and my sister, who always support me in any way possible and my friends, who celebrate the good times with me and share the bad ones. Marc, thank you for your support, your great company, your strength, your faith in me and your love – I couldn't have done this without you!